TABLE OF CONTENTS

LIST OF FIGURES

LIST OF TABLES

CHAPTER 1

DEFINITION OF THE PROBLEM

CHAPTER 1

DEFINITION OF THE PROBLEM

1.1 INTRODUCTION

In recent years, Al-B_4C composite materials have been increasingly used as neutron absorber components in the nuclear industry. This is due to their special capability of capturing neutrons, and then lightweight, superior thermal conductivity and mechanical properties [1-4]. Generally, processing techniques for Al MMCs can be classified into: 1) liquid mixing process, 2) semi-solid process and 3) powder metallurgy process [5,6]. The liquid mixing process is an effective method to economically produce large quantities of Al-based metal–matrix composites. This process has been employed to produce most of the commercial Al-based metal–matrix composites [7]. However, during this process, B_4C usually is unstable in liquid aluminum and reacts with the Al melt to form reaction products, Al_3BC, AlB_2 and Al_4C_3 [8,9]. In order to limit the decomposition of B_4C particles and improve their wettability in the liquid metal casting process, Ti is added to Al-B_4C composites forming a TiB_2 barrier layer around the B_4C particle surfaces [9].

The fluidity of Al-based alloys and composites has been studied by several researchers [10,11]. In an alloy with rich solute, the flow arrest is due to a choking of the flow at the leading tip of the stream. When a critical concentration of solid is reached at the leading tip, the viscosity then rises rapidly and the flow ceases abruptly [12,13]. The reinforcement characteristics such as size, shape and volume fraction of ceramic particles

have an effect on the fluidity of Al-based composites [14]. It is reported that the volume fraction of the reaction-induced particles increases and its fluidity deteriorates with the increase of melt holding time [9]. Moreover, the particle agglomerates, particle settling and pushing, presence of oxide films, and the appearance of reaction-induced particles influence the flow behavior of the composite melt [15]. Furthermore, during remelting, the fluidity of the composites can be influenced by different working processes due to their effect on the distribution of reinforcement particles [16]. However, the literature related to the recycling of metal matrix composites and the fluidity evolution of the scrap materials during remelting is very limited.

Quantitative characterization of the material microstructure is one of the means of investigating of the influence of the microstructure on the fluidity and mechanical properties. Image analysis techniques may be used to estimate the volume fraction evolution of solid particles [17, 18]. Besides, various methods have been developed for characterizing the spatial distribution of discrete secondary phase bodies on two-dimensional sections, including field methods, inter-particle spacing methods and tessellation methods [19].Moreover, numerous approaches for assessment of clustering have been proposed and applied in composite materials, such as the Euclidean distance; nearest neighbor distance; radial distribution function; and some others [20-21].

1.2 PROBLEMS

During manufacturing processes, the process scrap from the casting and transformation processes (extrusion and rolling) can reach 50 to 60% of the total materials produced. The need to recycle Al-B_4C composites thus becomes urgent to meet

environmental goals and to reduce production costs. Compared to standard aluminum alloys, the fluidity of metal matrix composites is already limited due to the presence of a large quantity of ceramic particles. For the liquid metal casting process, the fluidity of the composites can greatly influence the ability of the composites to be recycled for reuse. Remelting is a promising method to recycle process scrap materials because of its simplicity. Good fluidity is a basic requirement for the materials to be recycled with the remelting process. However, during the remelting process, since there are strong chemical reactions between B_4C and Al, the fluidity behavior of the scrap should be studied to better understand and optimize the recycling process, and microstructure of the remelted composite needs to be examined to understand the mechanism of the fluidity evolution.

1.3 OBJECTIVES

1. Investigate the fluidity evolution as a function of the holding time for two process scrap materials, namely AA6063-10 vol.% B_4C (cast billets and extruded plates) and AA1100-16 vol.% B_4C (cast ingots and rolled sheets).
2. Study the influence of casting, extrusion and rolling processes on microstructural features, such as particle distribution, particle agglomeration and interfacial reaction products.
3. Study the impact of particle amount, particle segregation and agglomeration, as well as particle distribution on the fluidity evolution.
4. Attempt to propose widely applied approaches for microstructure characterization of metal matrix composites.

1.4 METHODOLOGY

1. A vacuum fluidity test setup is used to investigate the evolution of the fluidity of cast billets, extruded plates and rolled sheets with prolonging of holding time.

2. The methods for characterization of the microstructure of Al-B_4C composites are developed in terms of particle volume fraction, distribution agglomeration and effective volume fraction using optical microscopy, scanning electron microscopy (SEM) and optical image analysis techniques.

3. The microstructures of original materials and remelted samples are examined and quantitatively analyzed to establish the relationship between microstructure and fluidity evolution.

CHAPTER 2

LITERATURE REVIEW

CHAPTER 2

LITERATURE REVIEW

2.1 INTERFACE OF AL-B_4C COMPOSITES

Interfaces in composites are regions of finite dimension at the boundary between the reinforcement and the matrix where compositional and structural discontinuities can occur over distances varying from an atomic monolayer to over five orders of magnitude in thickness [22]. The nature of interfaces that develop in composites during fabrication and subsequent service is critical to their response to mechanical stresses, and thermal and corrosive environments[23]. The development of a suitable interfacial bond between the reinforcements and matrix is, therefore, a primary requirement for optimum performance of a composite [24, 25].

Using the liquid metal process, Al-B_4C MMCs are manufactured at temperatures well above the liquidus of the aluminum matrix, and the processing time can amount to a few hours. In addition, B_4C is not stable in an aluminum melt, as the particles may react with aluminum to form reaction products, AlB_2, Al_4C_3, and Al_3BC, which deteriorate the fluidity of the melt and certain mechanical properties [2,25-27]. It is reported that titanium addition can improve the uniformity of the particulate distribution within aluminum matrix [27]. Through the formation of a layer rich in titanium on the surface of the particulates, this can limit decomposition of the B_4C particles [27]. In addition, it is also found that the amount of the reaction products in the composites increases with the

increase of holding time. However, the rate of the increase is reduced by the increase of the content of titanium in the composites.

2.1.1 Interfacial reactions of Al-B_4C composites

Since B_4C is not stable in an aluminum melt, the particles may react with the aluminum to form reaction products which deteriorate the fluidity of the melt and certain mechanical properties [2,8,27,28]. It was reported that when the Al–B_4C temperature is between660 °C and 868 °C, the reaction products are Al_3BC and AlB_2 [8]. To overcome the reactivity problem of B_4C particles, titanium is added into the composite melt to form a barrier layer on the surface of the B_4C particulate, thus limiting the interfacial reactions between the B_4C and liquid aluminum [2,27].

Z. Zhang et al. [9] have found that by adding higher levels of Ti (approximately 2%) in Al–10% B_4C composite, most B_4C particles become stable in the aluminum matrix. No significant degradation of B_4C is observed.

Figure 2.1 shows an optical metallograph of Al-B_4C composites. In this micrograph, secondary reaction-induced solid particles around the B_4C particles appear in the aluminum matrix. These particles are the interfacial reaction products. The color of one type of particle is yellow and that of another one is gray when seen under the optical microscope. Most of the gray particles are connected or close to the B_4C particles. The yellow particles are often not attached to the B_4C particles [9].

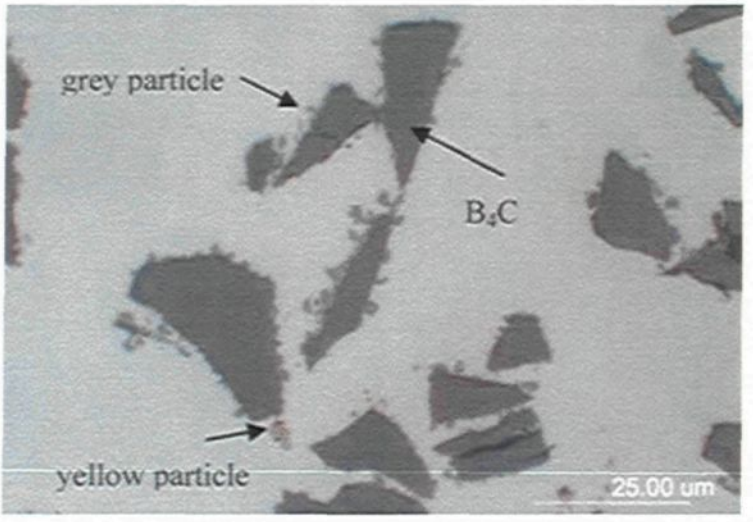

Figure2.1: Microstructures of the Al-B_4C composite sample [9].

Several of the yellow particles were examined using an electron probe microanalyzer (EPMA) [9]. They were to be AlB_2. The backscattered electron image of the Al-B_4C composite sample is shown in Figure 2.2. A Ti-rich layer enclosing B_4C particles and some reaction product particles distributed inside and outside of this layer were found. The reaction product particles consisted of Al, B, and C elements as detected by EDS analysis.

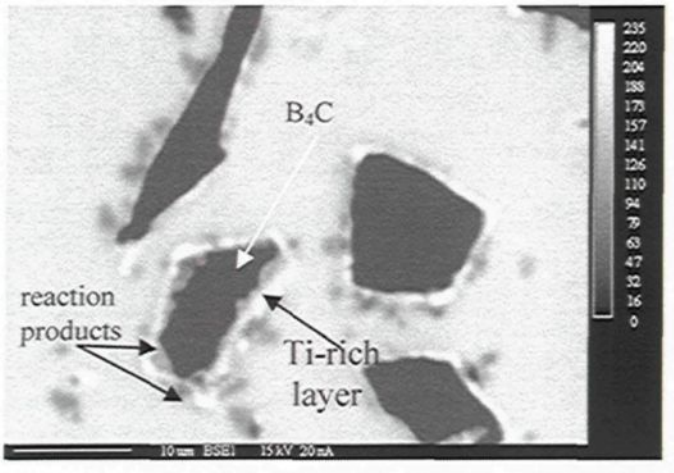

Figure2.2: Backscattered electron image of the Al-B_4C composite sample[9].

The Ti-rich layer was determined to be composed of fine TiB_2 crystals (crystal size: 0.1–0.5μm) and the reaction products were Al_3BC crystals (crystal size: 0.3–0.8μm) by means of transmission electron microscopy. Figure 2.3 is a TEM dark field image of the sample. In this image, there are two B_4C particles. The smaller one is located at the lower right corner. The B_4C particle surfaces are covered a layer of Al_3BC crystals and then a layer of fine TiB_2 crystals that encloses the Al_3BC layer and the B_4C particles. Outside the TiB_2 layer, there is another layer of Al_3BC crystals which continues to grow during the melting period. Therefore, the gray particles seen in the optical metallographs include two phases: TiB_2 and Al_3BC. Based on the above observation, the microstructure of the Al–10% B_4C composite consists of B_4C particles and Al_3BC, AlB_2, and TiB_2 phases. The addition of Ti during remelting reacts with B_4C to form a TiB_2 layer around the B_4C particles.

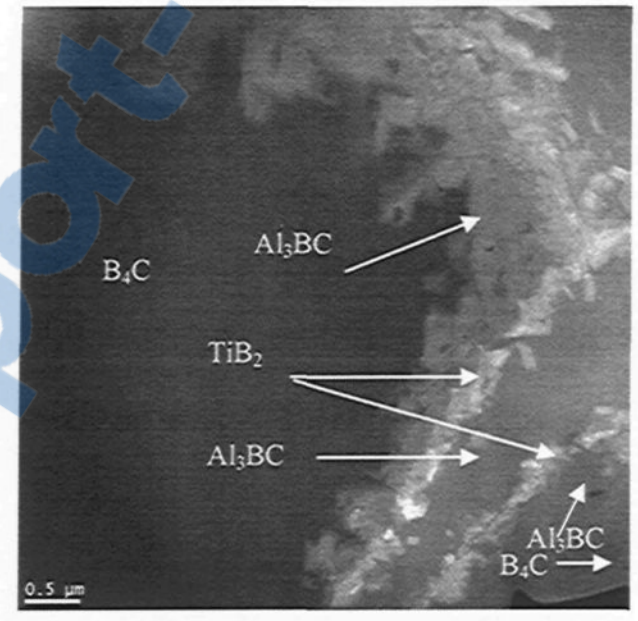

Figure 2.3: A dark field image (TEM) of the Al-B_4C composite sample[9].

In other B_4C systems such as Al–Si–B_4C composites and Al–B_4C composites, such

reactions and their reaction products (Al_3BC, TiB_2, and AlB_2) have also been demonstrated [8,29,30].

2.1.2 Interfacial reaction thermodynamics

It took several decades for material scientists to identify the reaction products of Al-B_4C composites. In 1989, based on the previous researches, Halverson[31] investigated the reaction thermodynamic of Al-B_4C in a larger temperature range from 800 °C to 1400 °C which is illustrated in Figure 2.4. The significant conclusion from this paper is that it reports the appearance of the X phase which formed around the B_4C evolves and consequently ties up most of the free carbon required to form Al_4C_3 and thus protects the B_4C particulates from being attached by Aluminum. This result was proved to be correct by later research studies [8,32]. This is a specific feature that differentiates the Al-B_4C couple from other reactive couples such as Al-TiC [33]or Al-SiC [32, 34-36] at the interface of which Al_4C_3 appears as a major reaction product. Due to its hygroscopic nature and poor mechanical properties, Al_4C_3 is always undesirable.

The X phase mentioned by Halverson was determined to be Al_3BC by Viala [37]. Based on Viala's detailed report [8], as long as the temperature is lower than 660 °C, i.e. in the solid state of aluminum, the reaction between B_4C and aluminum becomes very slow. Nevertheless, in the range from 660 °C to 827 °C, the reaction rate increases sharply, forming the ternary carbide (Al_3BC) and diboride (AlB_2). Above 868 °C, Al_3BC is still formed, while $Al_3B_{48}C_2$ (β -AlB_{12}) replaces AlB_2. The other phases ($AlB_{12}C_2$ and Al_4C_3) are formed only at the higher end of the investigated temperature interval of 985 °C ~ 1370 °C. With the onset of formation of the boron rich $AlB_{12}C_2$ phase, the depletion of B_4C increases significantly[38]. For long term heating beyond 868 °C, Al_3BC

phase plays an important role in preventing the B_4C particle from being attacked by aluminum. The equations corresponding to these chemical reactions are as follows:

$$4\ B_4C(S) + 13\ Al(L) \Leftrightarrow 4\ Al_3BC(S) + AlB_{12}(S)\ (T > 985°C)\ ^{[39]} \quad (2.1)$$

$$2B_4C(S) + 9Al\ (L) \Leftrightarrow 3AlB_2(S) + 2Al_3BC(S) \quad (T < 897\ °C)\ ^{[8, 40]} \quad (2.2)$$

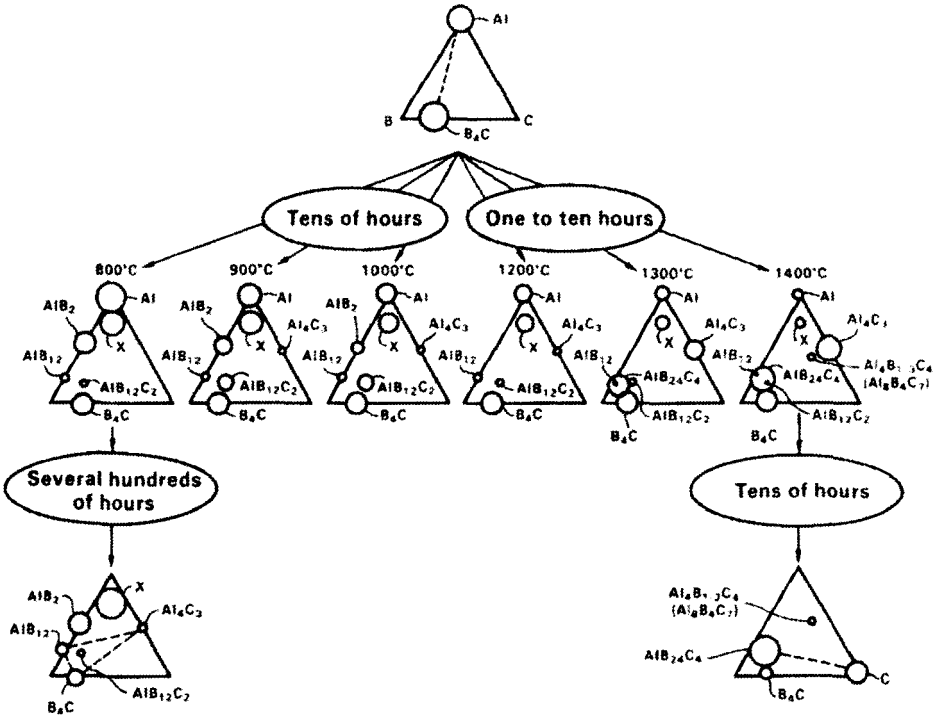

Figure2.4:Thermodynamic-reaction-series map for Al - B_4C composites at 1180°C and heat-treated under various isothermal conditions between 800 °C and 1400°C[31].

Taking into account the addition of titanium in the matrix, the reactions between Ti-B_4C are briefly summarized here. The Ti-B_4C phase diagram is illustrated in Figure 2.5 [41]. The changes in free energy and enthalpy of the possible reactions with titanium at 1023 °C are shown as below[34]:

$$B_4C + 3Ti \Leftrightarrow 2TiB_2 + TiC \quad (2.3)$$

$$\Delta G° = -624.6\ kJ/mol,\ \Delta H° = -700.5\ kJ/mol \quad (2.4)$$

which means this is an exothermic reaction. The $\Delta G°$ and $\Delta H°$ for this reaction are generally more negative than those for the reaction between aluminum and B_4C particles, with values of -335 KJ/mol and -556 KJ/mol, respectively [2]. After a period of holding above the melting point, all the titanium was consumed and converted into TiB_2 [1,34], and the size of the TiB_2 particles ranges from approximately 0.1 ~ 1 μm [2].

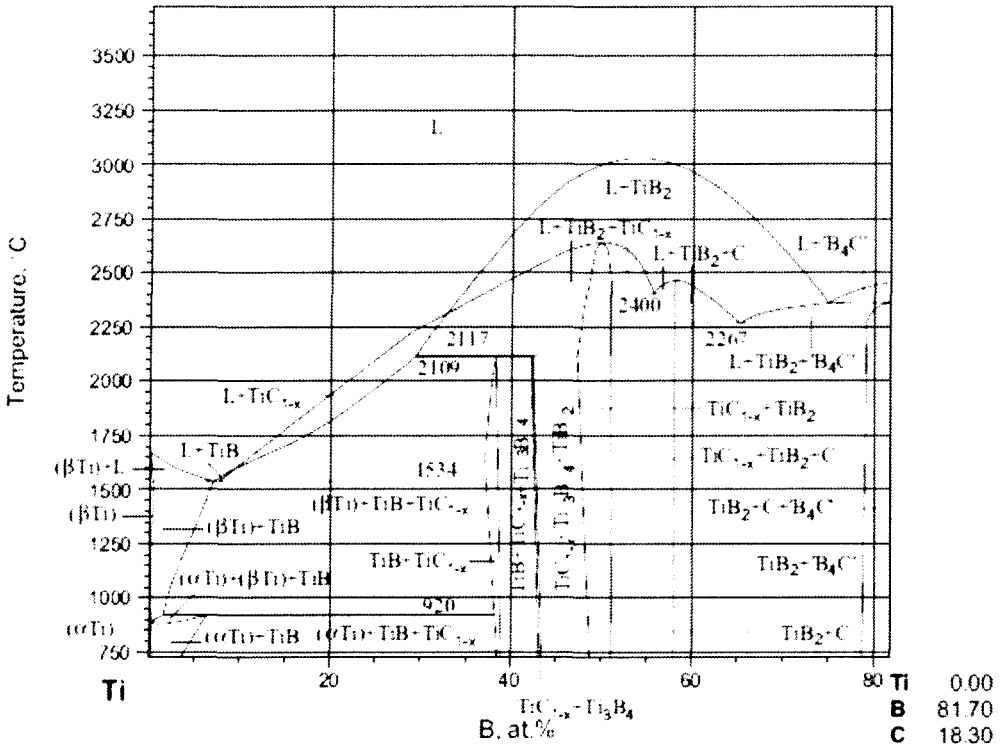

Figure 2.5:Calculated isopleths of the Ti- B_4C phase diagram [41].

2.2 FLUIDITY

The fluidity is the ability of molten metal to flow in a long channel of small cross sections [42]. The fluidity of an alloy is influenced by the temperature, the composition, the density and the viscosity of the alloy, thermal properties of the metal and the mold and test variables such as applied metal head and channel diameter [43]. For a composite, the addition of particles to the melt implies that additional parameters which influence the

fluidity above those presented for the pure alloy must also be considered, namely, volume fraction, size and shape of particles, reactions, segregation, clustering, gas and inclusions[15].

To evaluate the fluidity of metals, there are two common types of fluidity tests: the spiral fluidity test and the vacuum fluidity test [13,42]. The fluidity is measured in terms of the length along which the molten melt flows in the long channel before it is stopped by solidification [42]. Flemings developed the following equation to evaluate the fluidity of pure metal, assuming that friction, acceleration, and separation of the flow are negligible [42].

$$L_f = \frac{\rho_s a v}{2h(T_M - T_O)}(H + \Delta T) \tag{2.5}$$

where:

L_f: Fluidity length (fluidity),

ρ_s: Density of the solid metal,

a: Radius of cross-session of channel,

v: Velocity of the molten metal,

H: Latent heat of fusion,

C: Specific heat of molten metal,

$\triangle$T: Superheat,

h: Heat-transfer coefficient,

T_m: Melting point of metal,

T_o: Temperature of the mold.

The model indicates that the velocity of the molten metal is one of the key factors influencing the fluidity, as the temperature of melt and mold, as well as the interface heat-transfer coefficient are fixed for a metal. However, the melt viscosity has a strong influence on its velocity to fill the mold channel under pressure.

In the case of a pure metal, the solidification front is planar, as shown schematically in Figure2.6. For alloys that freeze over a range of temperature, however, solidification is not the same. The pattern of solidification in a fluidity test for a longer-freezing range alloy is well explained by Campbell [13]: Dendrites which grow at an early stage of freezing can be broken by the stream and the fragments of the dendrites then flow with the stream. The stream develops into a slurry of tumbling dendritic crystals. When these grow to the point at which they start to impinge on each other, the mixture stiffens, becoming suddenly more resistant to flow. This phenomenon is represented in Figure2.7.

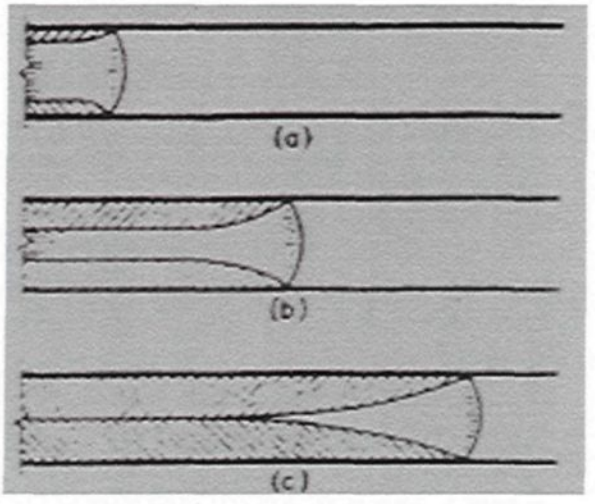

Figure 2.6: Flow and solidification front of a pure metal in channel [13].

(a) Liquid enters flow channel; columnar grain formation with jagged liquid-solid interface begins;

(b) Columnar grains grow as metal flows;

(c) Choking off occurs at flow channel entrance.

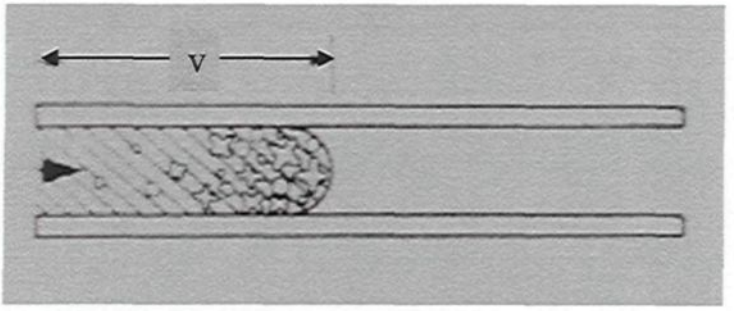

Figure 2.7: Flow arrest in long-freezing-range alloys in a channel [13].

- Liquid enters flow channel; fine grains nucleate at tip;
- Nucleation continues and fine grains grow rapidly as flow progresses;
- Flow cease when a critical concentration of solid is reached near the tip.

Furthermore, Flemings et al.[12] developed equations to estimate the fluidity evolution for the longer freezing range alloys(Equation 2.6, 2.7).When all resistance to heat flow is at the metal-mold interface(h type heat flow), the flow length is:

$$L_f = \frac{a\rho' V_0(\lambda H + c'\Delta T)}{2h(T - T_O)} \tag{2.6}$$

When all thermal resistance is in the mold (θ type heat flow),

$$L_f = \frac{a\rho'(\pi \times V_0)^{0.5}(\lambda H + c'\Delta T)}{4(K\rho c)^{0.5}(T - T_O)} \tag{2.7}$$

where,

L_f : Fluidity length (fluidity),

a : Radius of cross-section of channel,

ρ' : Density of the liquid metal,

c' : Specific heat of the molten metal,

V_0 : Initial velocity of the molten metal,

λ : Critical solid concentration,

H : Heat of fusion,

ΔT : Superheat,

h : Heat-transfer coefficient,

T : Metal solidification temperature,

T_0 : mold temperature,

K : Conductivity of mold,

ρ : Mold density,

C : Specific heat of mold.

Equations 2.6 and2.7 assume that solid particles form during flow in a fluidity channel and travel downstream with the liquid; flow stops when the mean solid concentration near the flow tip reaches a certain value, λ , (critical solid concentration), and flow velocity is constant until flow stops. Regardless of the heat flow being either h or θ type, or intermediate, it can be shown that λ can be calculated from the test variables as

$$\lambda = \frac{c'}{H}\left(\frac{L_f}{dL_f / dT}\right)_{T=T_M} \tag{2.8}$$

2.3 FLUIDITY OF COMPOSITE

Addition of solid particles into the melt affects the fluidity by the modification of solidification time and flow properties in which the ceramic particles added to the liquid phase do not have the same thermal properties as the liquid metal. Thus, the solidification time of a composite melt will be different from that of the pure alloy, due to change in the latent heat caused by the volume fraction of the solid phase, and a change in the superheat and effective thermal conductivity of the melt. For the description of composite fluidity, Equation2.9 was proposed by introducing the fraction of reinforcement particles and their properties into the equation [11].

$$L_f = \frac{(\rho_f \phi_m + \rho_d \phi_d) av}{2h(T_m - T_O)} [H_m(1-\phi_d) + (C_m W_m + C_d W_d)\Delta T] \tag{2.9}$$

where:

ρ: Density of the solid metal,

φ: Volume fraction,

C: Specific heat,

H: Latent heat,

W: Weight fraction of matrix (m) and reinforcement particles (d).

This equation indicates that the density, fraction and thermal properties of particles have an effect on the fluidity. It is reported that decrease in fluidity with increase in SiC volume fraction predicted by the equation is consistent with the experimental observations, provided v and h do not change significantly [15]. However, the factors important to composite fluidity but not considered in Equation 2.9 such as settling,

agglomeration, and pushing of particles, presence of gas and oxides and reaction-induced changes may result in deviations between theory and experiment [15]. Moreover, the effect of reinforcement particles on the mechanism of flow arrest in the channel in a fluidity test could also influence the composite fluidity as predicted by Equation2.9.

It was found that one of the major factors for the decrease of fluidity was the increase in the viscosity of the melt for an Al-Al_2O_3 composite [10]. However, the increase of the viscosity is more than that predicted by Equation2.10 [44]. The reasons resulting in the extra increase viscosity and involving the change of surface areas are the variation of shape and size of particles at a given volume percent. Moreover, the fluidity of the composites is related to the surface area of particles, and a linear relationship between the fluidity and the surface area is observed [9].

$$\eta_s = \eta_0(1 + 2.5\phi + 10.52\phi^2) \qquad \phi < 0.25 \tag{2.10}$$

where:

η_s: Viscosity of suspension,

η_o: Viscosity of suspending medium,

φ: Volume fraction of dispersed phase.

The predictive capability of the Flemings model is limited at present for metal matrix composites. This can be attributed to the noninclusion of factors such as particle size, shape, agglomeration, and the effect of interfacial reactions, which lead to an increase in the effective solid fraction in the slurry. K.R. Ravi et al. [45] modified the Flemings model by incorporating (i) the solidification behavior of alloys; (ii) the decrease in flow velocity due to surface tension and friction losses; and (iii) the increase in

viscosity of composite slurries due to reinforcement size, shape, and volume fraction, and proposed Equation2.11 to evaluate the spiral fluidity length of aluminum Al-SiCp composites without interfacial reaction and with interfacial reaction by using the volume-averaged properties of the particle-melt mixture such as density, specific heat, critical solid fraction, and latent heat.

$$L_f = \frac{\rho_c d\sqrt{\frac{2g(H - H_{surften})}{(1+f_d^L)}}}{2h(T - T_O)}(f_{sc}^{critical}\Delta H_c + C_c\Delta T)(1+\frac{K}{2}) \qquad (2.11)$$

where:

ρ_c: Volume-averaged density,

ΔH_c: Volume-averaged specific heat,

$f_{sc}^{critical}$: Volume-averaged critical solid fraction,

C_c: Volume-averaged latent heat.

2.4 INFLUENCING FACTORS OF REINFORCEMENT ON FLUIDITY

2.4.1 Particle volume fraction

In the case of particle-dispersed composites, the fluidity at any given temperature is diminished relative to the particle free base alloy [11,46,47]. Surappa and Rohatgi [10] observed a decrease in spiral fluidity with the addition of reinforcement like mica, graphite, silicon carbide and alumina particles in the size range 40–200 μm in various Al alloys. Carity [48] found that spiral fluidity decreases with volume fraction of SiC in A356

and A357 alloys cast in permanent mold (Figure2.8). Z. Zhang et al. [9] found that an increase in the volume fraction of solid particles in Al-10% B_4C composite results in the decline of the fluidity.

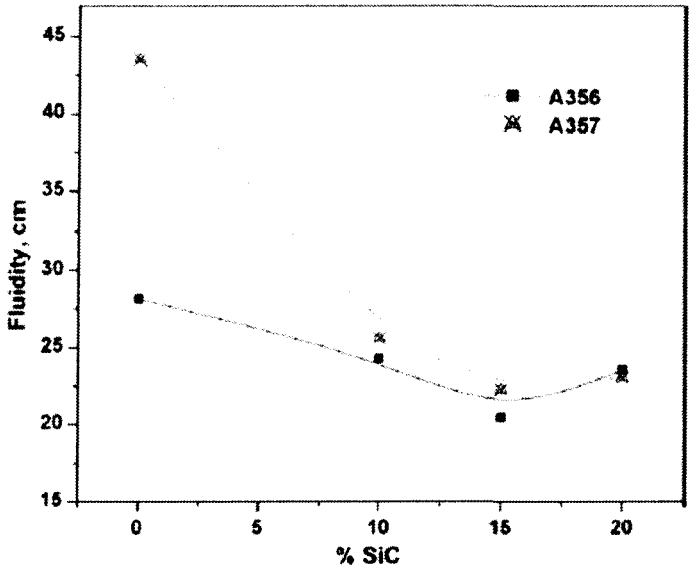

Figure 2.8: Fluidity vs. vol.% of SiC particles in A356 and A357 cast in permanent mold [48].

2.4.2 Particle surface area

It was also observed that the fluidity of the Al-based composites was related to the size and shape of reinforcing particles (Al_2O_3, SiC and B_4C) [9,10,49]. The composite fluidity decreased with a decrease in particle size and with an increase of angularity for a given percentage of the reinforcement. The relationship between the fluidity length (F, in cm) and the Al_2O_3 particle surface area (x, in $m^2/100$ g) could be expressed by Equation 2.12, where a and b are constants [10].

$$F = a - bx \tag{2.12}$$

It was suggested that the decrease in the Al–alumina composite fluidity with an increase in the surface area of alumina particles may be attributed to the viscosity

increase in the melt [10]. Surappa and Rohatgi [10] observed that spiral fluidity tested in a permanent mold casting decreased linearly with the total surface area per unit weight of the particles (Figure 2.9)

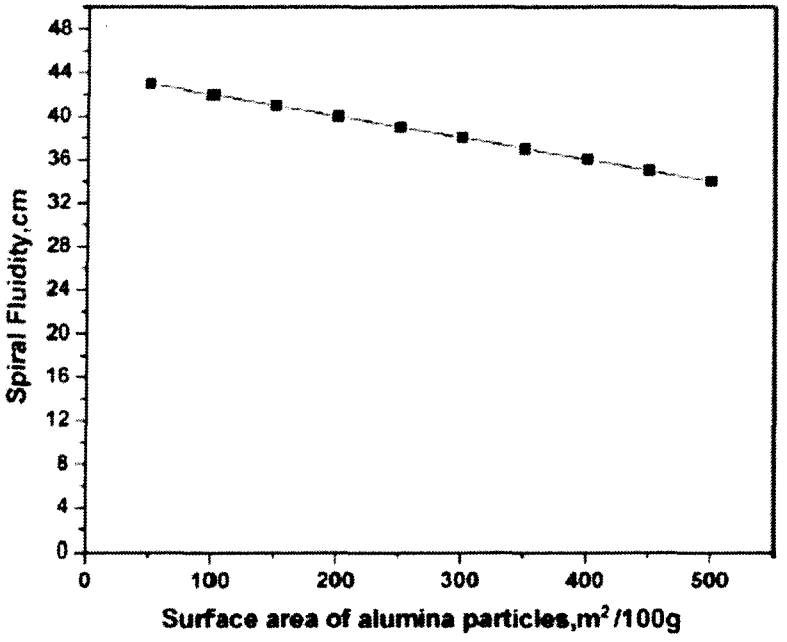

Figure2.9:Variation of spiral fluidity (cast in permanent mold) as a function of specific surface area of ceramic particles [10].

2.4.3 Particle size

The fluidity of Al–4.5Cu–mica composites [50] (cast in permanent mold) decreases with a decrease in the reinforcement particle size for a given volume fraction of particles (Figure2.10). Yarandi et al. [51] found that the A356 alloy–SiC_p composite (cast in a permanent mold) containing 15 vol.% SiC_p of 9 μm diameter had the lowest flow ability, lower than that of composite containing 20 vol.% SiC_p of 14 μm diameter, indicating that particle size has a strong influence on flow and spiral length. The decrease with size has been attributed to an increase in the total surface area of particulates causing more

resistance to fluid flow as a result of stagnant boundary layers around the particles.

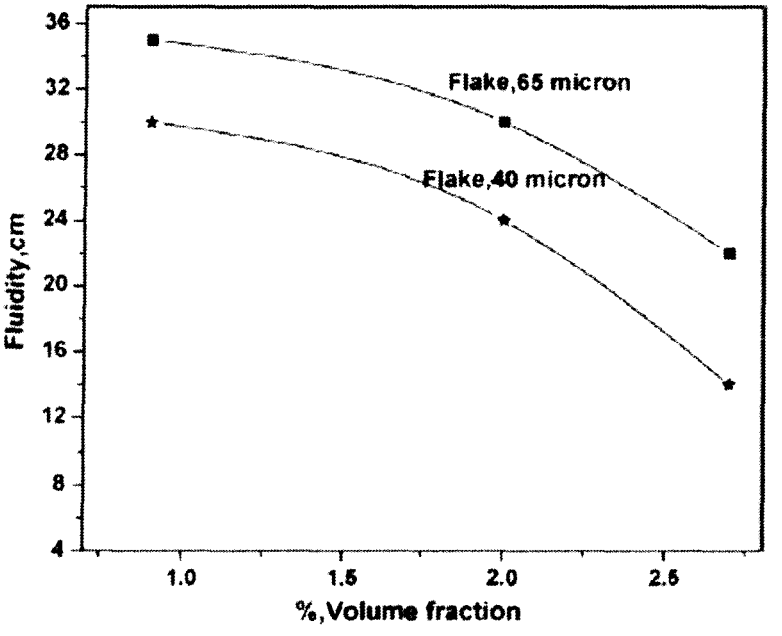

Figure 2.10:Fluidity vs. particle size of mica in Al–4.5% Cu alloys cast in permanent mold [50]

2.4.4 Particle shape

The morphology of the reinforcement influences the fluidity of composite melts because of its effect on the surface area-to-volume ratio of the dispersed phase. Increasing angularity (deviation from perfect sphericity) of the reinforcing particles leads to a progressively greater decrease in the fluidity at a given temperature and volume fraction of particles (Figure2.11) [50].

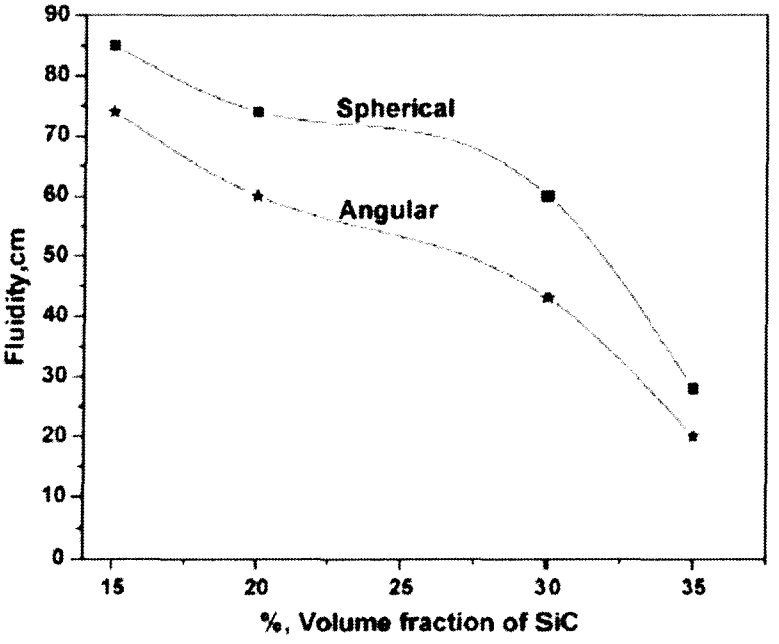

Figure 2.11:Fluidity vs. particle shape of SiC in A356 alloys cast in permanent mold [50].

2.4.5 Particle agglomeration

The distribution of SiC particles in the Al melt is not perfectly uniform and the presence of particles increases the viscosity of the melt [14]. Besides, the particle clusters and networks have an important contribution to the deterioration of the composite fluidity[9].

2.4.6 Interfacial reaction

A study on the relations between fluidity and reaction products has been done, and analysis of the fraction of the reaction products of Al-10%B_4C metal matrix composite and the surface area has been performed by means of an image analyzer [9]. Two main interface reaction phases, AlB_2 and Al_3BC, exist in the composite. The fluidity of Al-10%B_4C decreases with the increase of holding time. During the first period up to 400

minutes of holding time, the deterioration of fluidity is much faster than at all other holding times. Exactly during this period (400 min), the surface area increases more quickly, about 60% of the total increase in amount. The increase of surface area directly results in the decrease of fluidity. Therefore, the increase of reaction products during the holding time would greatly impact the fluidity of Al-B_4C composites [9].

2.5 INFLUENCE OF MECHANICAL DEFORMATION ON FLUIDITY

During remelting, the fluidity of the composites through casting and transformation processes can be influenced due to the distribution of reinforcement particles during these processes [14,16]. In composites processed by molten metal mixing methods, the particle distribution is influenced by the mixing and the solidification rate[16]. The reinforcement particles are rejected at the solid/liquid interface and segregate to interdendritic regions after solidification. As well, a slow solidification rate would lead to very inhomogeneous particle distribution. Secondary fabrication processing such as extrusion or rolling, can homogenize the structure to some extent during the severe work deformation [16].

2.6 CHARACTERIZATION OF COMPOSITE

2.6.1 Particle volume fraction

Addition of solid particles into the melt affects the fluidity by the modification of solidification time and flow properties [28]. For the composite fluidity, Equation2.8 indicates that the fluidity will decrease with an increase in volume fraction of solid particles.

For quantitative evaluation of the volume fraction of particles in the composites, the image analysis technique can be used to relate the measurements performed on two-dimensional images to the three-dimensional structures that are represented and sampled by those images. If a structure or phase can be identified in an image, and that image is representative of the whole specimen, then the area fraction that the phase occupies in the image is a measure of the volume fraction that it occupies in the whole specimen [52]. Actually, this relationship is one of the oldest known relationships in quantitative stereology, used in mineral analysis 150 years ago [52]. This requires some clarification in which the image must be representative in the sense that each phase has an equal chance of being examined; thus, the sections must be uniformly and randomly placed in the specimen. In most real structures, this is ensured by collecting many images from multiple fields of view spread throughout the specimen in an unbiased way. Then the measured area fractions of the phases may be equal to the volume fraction of these phases[52].

Therefore, using image analysis method, estimation of the volume fraction of phases is to count (in a binary image) all the pixels that represent the analyzed phase and use this number in the image as a reference value [17,53]:

$$V_V = A_A = \frac{N_P}{N_O} \tag{2.13}$$

where, V_V denotes volume fraction, A_A denotes area fraction, N_P denotes the number of pixels that corresponding to the phase being analyzed, and N_O is the total number of pixels in the image.

2.6.2 Particle distribution

Reinforcement distributions play an important role in various aspects of the processing and final mechanical behavior of particulate metal matrix composites (PMMCs). In general, a non-uniform distribution of particles in the aluminum matrix and the presence of these particles increase the viscosity of melt, resulting in decrease of fluidity [29]. Moreover, controlled particle distribution in the matrix is very important for composite material applications since it greatly impacts the mechanical properties such as tensile strength and elongation of the materials [19].

Various methods have been developed for characterizing the spatial distribution of discrete secondary phase bodies on two-dimensional sections, such as field methods, inter-particle spacing methods and tessellation methods [19].

The simplest field methods involve comparing numbers of particles in defined areas[54]. Others focus on the variance of the number of particles in a box of specified area, moved randomly around the field of study, or from the rate of decrease of this variance with increasing box size [55,56]. Inter-particle spacing methods, most of which are based on the measurement of nearest neighbor distances between particle centroids, offer improvements over field methods by their ability to differentiate different types of distribution and quantify local clustering characteristics [57-60].

Tessellation methods represent a further improvement over inter-particle spacing methods in that the more general surroundings of individual secondary phase particles may be uniquely characterized [61-63]. Established Dirichlet tessellation methods utilize the centroids of particles to construct a network of polygon cells such that any point within a cell is closer to the centre of the cell (i.e. the centroid of the particle) than to any

other centroids, as shown in Figure 2.12 [64]. It is given by the inner envelope of the perpendicular bisectors of the lines joining the given point to the other points. Based on the tessellated cell structure, a variety of parameters relating to spatial distribution may be derived, including "neighboring particle" parameters (defined as cells sharing cell boundaries) and near-neighbor distance (defined as the shortest distance between corresponding particle centroids) [19]. For example, Lloyd [65] studied the particle distribution in two particle reinforce MMCs. A more clustered composite could be distinguished from a more homogeneous one by a large tail at the long separation end of a near neighbor histogram.

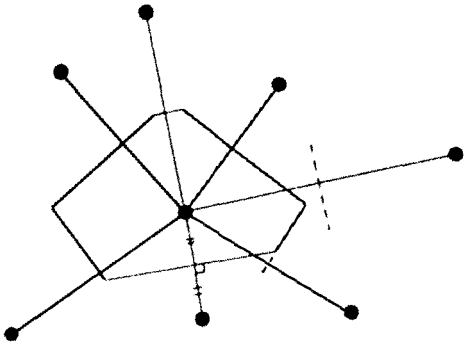

Figure 2.12: Construction of a Dirichlet cell for a given point [64].

In addition to identifying the near neighbors of each particle, the cells themselves can provide useful information about the distribution. Several studies [66,67] has shown that a clustered distribution would be expected to generate a wide range of cell sizes, ranging from small cells in heavily clustered regions to large cells in particle denuded zones. A more homogeneous distribution would have a narrower range of cell sizes. Furthermore, a most appropriate parameter for characterizing the homogeneity of particle distribution was found to be the ratio of the variance of the distribution of cell areas to the

variance of random distribution with the same average areal density of particles by Dirichlet tessellations [68].

Alternatively, the tessellation can be carried out using a "growth process" [69]. Growth occurs from the particle periphery in all directions at the same rate and continues until each cell comes into contact with all of its neighboring cells. Growth tessellations can have non-linear cell boundaries, in contrast to Dirichlet cells. However, compared with the Dirichlet method, a large particle is always contained within a large cell when the growth method is used, and even a long, thin particle is always contained within a long, thin cell, whereas this is not always the case using the Dirichlet method.

2.6.3 Particle agglomeration

Clustering of second-phase has been recognized as a factor influencing materials properties and behavior, such as ductility and formability, toughness and fatigue life [70]. Furthermore, the presence of particle agglomerates results in an increase of the flow resistance to the composite melt and deteriorates the fluidity of the composite [9]. Particle cluster is one type of particle agglomerates, forming a dense solid particle complex. Particle network is a less dense agglomerate induced by oxide films or reaction products. These agglomerates are formed during the composite preparation and melt holding. They likely move as a whole mass during the fluid flow and occupy a much greater space than the sum of individual solid particles. Consequently, the effective volume of solid particles in the melt is remarkably increased due to these agglomerates. Li et al. have noted that particle cracking is more likely to occur in larger particles that are located in clusters [71].

A variety of approaches to assess clustering have been proposed and applied in

composite materials. These methods include the Euclidean distance; nearest neighbor distance; radial distribution function; and some others [20,21,72]. All of these consider the distance between the particles from an absolute measure: i.e. if two particles are within 5 μm of each other, they form a cluster. G. Langelaan et al. [73] have described another method to characterize the clustering of intermetallic particles in an aluminum alloy by considering the size of each particle and estimating the size of its strain field based on Eshelby's work. Accordingly, any particle with overlapping strain fields would be defined as belonging to a cluster.

CHAPTER 3

EXPERIMENTAL PROCEDURES

CHAPTER 3

EXPERIMENTAL PROCEDURES

A vacuum fluidity test setup was used to investigate the evolution of the fluidity of cast billets, extruded plates and rolled sheets as a function of the melt holding time. Subsequently, the microstructural features and interfacial-reaction-induced particles observed in the remelted aluminum composites were identified using optical microscopy. Furthermore, the characteristics of B_4C particles and interfacial reaction-induced particles, such as particle volume fraction, distribution and particle agglomerates, and effective volume fraction were examined and quantitatively analyzed to establish the relationship between microstructure and fluidity evolution by using optical microscopy, scanning electron microscopy (SEM) and image analysis.

3.1 FLUIDITY TEST

3.3.1 Material preparation

The process scrap of AA6063-10 vol.% B_4C Direct Chill (DC) cast billets and their extruded plates, as well as AA1100-16 vol.% B_4C DC cast ingots and their rolled sheets fabricated by Rio Tinto Alcan, were used in this investigation. The average B_4C particle size in both materials was approximately 17 μm. The AA6063-10 vol.% B_4C cast billets had a diameter of 7 inches. The extrusion plates were rectangular with a section dimension of 8 × 144 mm, and the extrusion ratio was about 22:1. Besides, the AA1100-

16 vol.% B_4C cast ingots had a rectangular section of 6 × 6 inches, while the thickness of the rolled sheets was approximately 4.5 mm and the hot rolling reduction ratio was 97%. All these scrap materials are shown in Figure3.1. The chemical compositions of both matrix alloys are Aluminum Association Standard Compositions, except for the Ti content (Table 3.1). In Al-B_4C composites, the Ti addition is necessary to prevent the decomposition of B_4C particles.

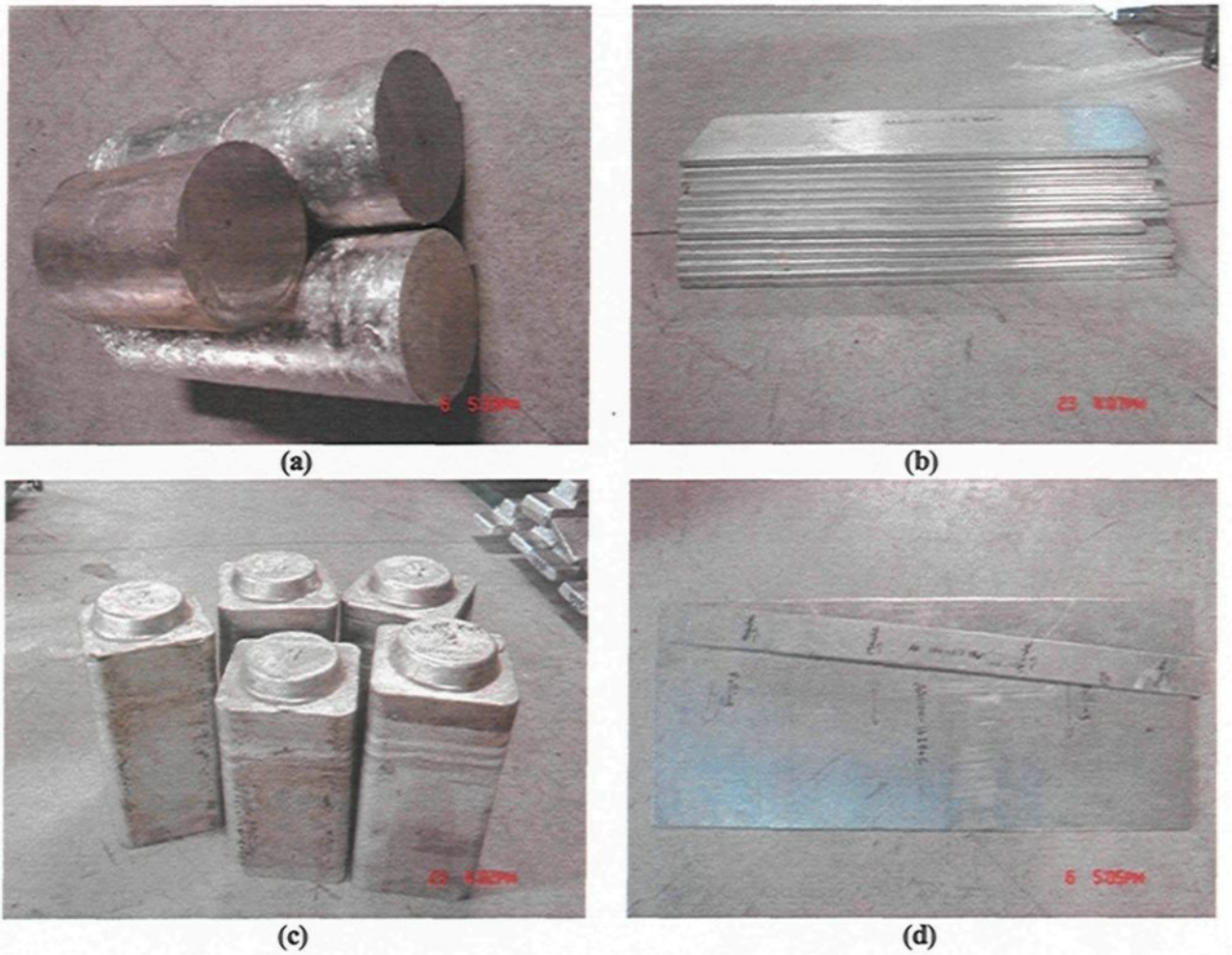

Figure 3.1: The scrap materials used in Fluidity tests: (a) AA6063-10 vol.% B_4C cast billets; (b) AA6063-10 vol.% B_4C extruded plates; (c) AA1100-16 vol.% B_4C cast ingots; (d) AA1100-16 vol.% B_4C rolled sheets.

Table 3.1: The chemical compositions of matrix alloys AA6063 and AA1100.

Alloy	Composition (wt%)					
	Si	Fe	Cu	Mn	Mg	Ti
AA6063 (Matrix alloy)	0.2-0.6	0.35	0.10	0.10	0.45-0.9	1.0
AA1100 (Matrix alloy)	0.95 Si+Fe		0.05-0.20	0.05		1.5

3.3.2 Vacuum fluidity test procedures

The experimental system for fluidity test is illustrated in Figure 3.2, as well as the schematic diagram (Figure3.3). The Al-B_4C MMCs were sectioned and remelted in the electrical resistance furnace and held under mechanical stirring at a speed of 200 rpm using an impeller to ensure a uniform distribution of B_4C particles in the liquid. The melt temperature was maintained at 730 °C ± 2 °C for approximately 510 min (for Al-10 vol.% B_4C composites) or 150 min (for Al-16 vol.% B_4C composites). The holding time was counted when the composite began to be remelted (around 660 °C). The consuming time was about 30 min from remelting to the target temperature of 730 °C. In the fluidity tests, the composite melt was drawn into a 6 mm internal diameter glass tube under the predetermined 215 mmHg pressure. It should be noted that the curved part of the glass tube was heated on the flat surface of a heater to a temperature of about 100 °C to prevent breakage by thermal shock. While taking the fluidity samples, the tubes were immersed into the melt, approximately 12.25 mm deep from the melt surface. A crucible lifter was used to maintain a constant immersion depth of the glass tube in the melt. Fluidity samples were regularly taken at intervals of 30–60 min. After solidification of the

composite in the glass tube, the length of the composite in the tube (length of flow) was measured for the fluidity valuation. A fluidity sample is shown in Figure 3.4 as an example. In the meantime, samples were taken from the crucible by a small ladle for subsequent analysis.

Figure 3.2: A vacuum fluidity test setup.

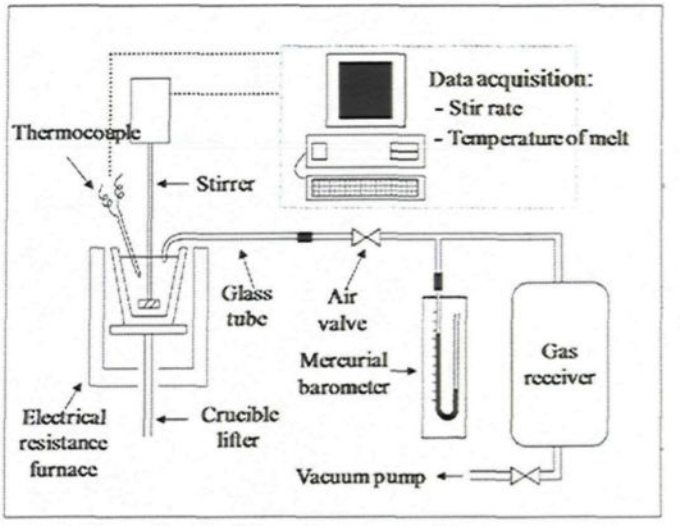

Figure 3.3: Sketch of vacuum fluidity test setup.

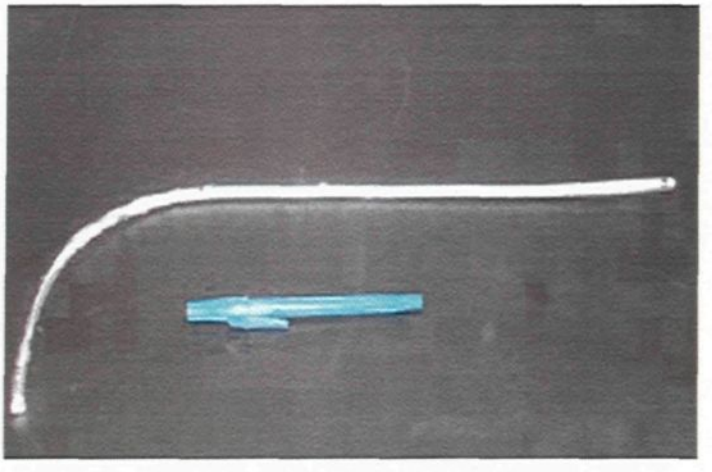

Figure 3.4: A fluidity sample.

3.2 MICROSTRUCTURE ANALYSIS

3.2.1 Sample preparation

Sections from the scrap materials of cast billets, extruded plates and rolled sheets before remelting were used for preparing metallography samples. In addition, the fluidity samples of cast billets, extruded plates and rolled sheets, with holding times of 30, 60, 90, 120, 150, 330, 510 minutes respectively, were transversely sectioned at different positions along the flow path, from flow entrance to flow end. Metallography samples were also obtained from the crucible (called "crucible sample") at holding times of 30, 90, 150, 510 minutes. All these samples were subsequently embedded in a phenolic hot mounting resin with carbon filler for grinding and polishing. The steps for preparation of metallographic samples of Al-B_4C composite are summarized in Appendix A. The finished samples were taken for microstructure examination using an optical microscope and image analyzer system. Fluidity samples of each material with holding times of 60 and 510 minutes, as well as their original materials were mildly etched with 2.5 vol.% NaOH base solution at 50-60 °C for 60 seconds to reveal the microstructure of the thin oxide film, as well as deeply etched using 10 vol.% NaOH base solution at 50-60 °C for approximately 70 seconds for the investigation of the spatial microstructure of particle agglomerates and the change of TiB_2 layer due to severe extrusion and rolling deformation processes.

3.2.2 Quantitative analysis of microstructure

The optical microscope equipped with a digital camera (Nikon ME 600) and an image analysis system (CLEMEX JS-2000, PE4.0) allows the examination and quantitative analysis of the microstructure, as illustrated in Figure 3.5.To investigate the impact of particles on the fluidity of Al-B_4C metal matrix composites, the methods for

characterization of Al-B_4C composite microstructures were developed in this research. These methods were applied to describe and quantitatively analyze the microstructures, such as particle volume fraction, distribution, agglomeration and particle effective volume fraction to establish the relationship between the microstructure of the composite and fluidity evolution.

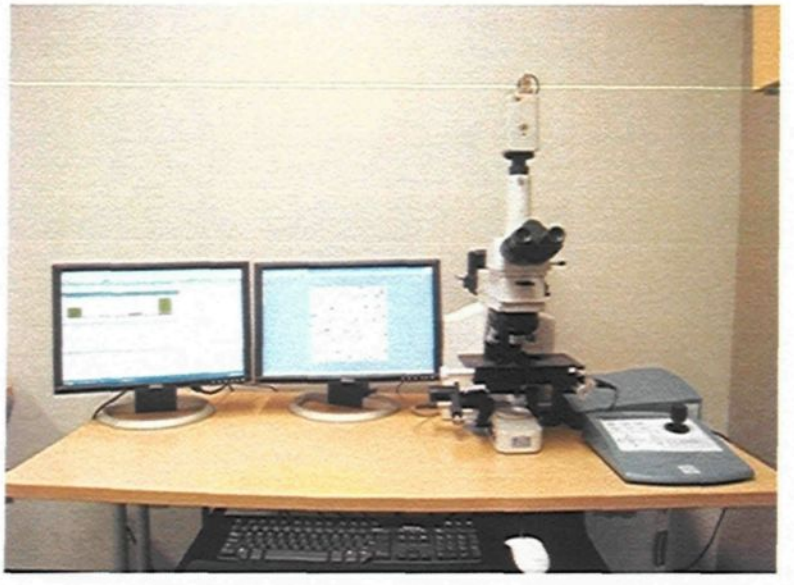

Figure 3.5: Optical microscope and image analysis system (Clemex).

3.2.2.1 Particle volume fraction

To investigate the influence of particle volume fraction evolution on the fluidity of Al-B_4C metal matrix composites during remelting and holding, the volume fraction measurements of B_4C particles and the reaction-induced particles with holding time was performed by analyzing the images obtained under optical microscopy. Images were taken from the crucible samples of cast billets, ingots, extruded plates and rolled sheets with holding times of 30, 90, 150, 510 minutes separately. For precise identification and quantitative measurement of the particles in the samples, the image analysis was carried out at 500× magnification and over 900 continuous fields (approximately 25 mm^2) on the

surface of a crucible sample, which typically represented the entire microstructure.

The image analysis ran with a routine that the user must program in advance. The routine developed for the measurement of particle volume fraction in Al-B_4C composite is shown in Appendix B, which could distinguish and characterize particles present in the samples. Firstly, the distinction of different particles needed to be done by image analysis as shown in Figures 3.6(a) and (b). In Figure3.6(a), which shows the microstructure of an Al-B_4C composite, the reaction-induced particles were fine TiB_2 particles, gray Al_3BC particles around the dark gray particles of B_4C and yellow AlB_2 particles. The Figure3.6(b) is the thresholded image, in which each of the different particles as shown in Figure3.6(a) was identified by the intensity of light, hue and saturation of color (IHS) associated with a given binary plane (bitplane), represented by a single color. Thus, the optical image was covered with green areas corresponding to the bitplane (Intensity: 110-200, Hue: 61°-250° and Saturation: 0%-100%) associated with the Al_3BC particle, the red bitplane (I: 121-200, H: 1°-60° and S: 0%-100%) for the AlB_2particle, the blue bitplane (I: 50-110, H: 0°-360° and S: 0%-99%) for B_4C and the pink bitplane (I: 120-200, H: 250°-359° and S: 0%-100%) corresponding to TiB_2. Each of the bitplanes correlated with one type of particles. Finally, the area fractions (i.e. volume fraction) of the solid particles represented by identified bitplanes were quantitatively and statistically measured throughout the selected 900 image fields using image analysis technique.

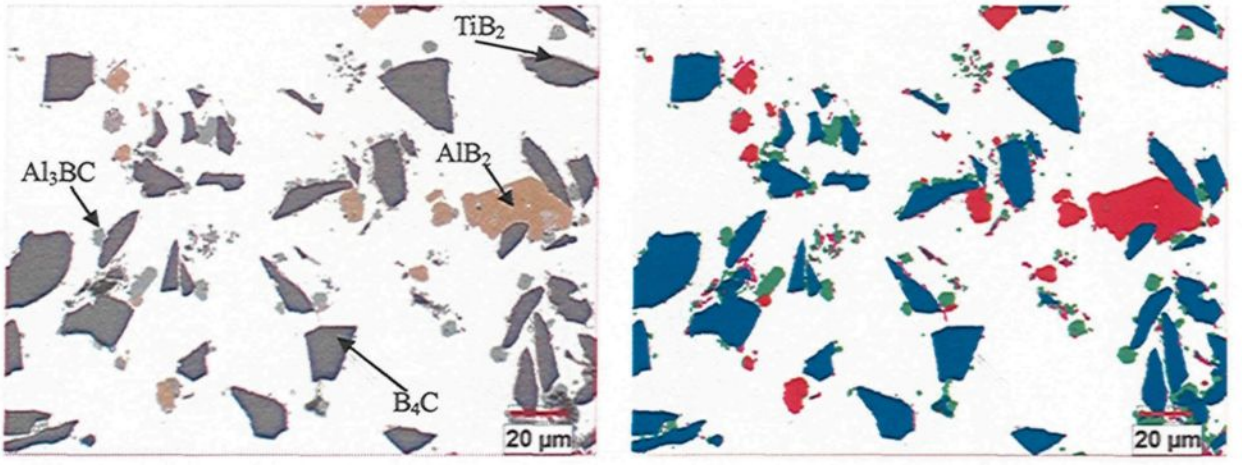

(a) (b)

Figure 3.6:(a) Optical image of Al-B_4C composite; (b) thresholding image.

3.2.2.2 Particle distribution

In this project, a homogeneity parameter was proposed for characterizing the variance of the particle distribution of cast, extruded and rolled Al-B_4C metal matrix composites to understand the influence of particle distribution on the fluidity evolution of these materials after remelting and holding. To investigate particle distribution, the crucible samples of cast billet and extruded plate with 10 vol.% B_4C at 150 and 510 min holding time were prepared, while such samples of cast ingot and rolled sheet with 16 vol.% B_4C were taken at 30 and 150 min separately. These samples were then mounted and metallographically polished for examination.

One mosaic image (942.5um×837um) was selected for the particle distribution analysis, which could be considered to typically represent the particle distribution of the whole mass. This image was captured at 500× magnification under the optical microscope, consisting of 5×6 field images (Figure 3.7(a)). After that, according to particle intensity, hue and saturation optical parameters, thresholding was performed to identify the different solid particles, such as B_4C, Al_3BC and AlB_2 (Figure3.7(b)). Then,

for each category of particles, the distribution was analyzed. Take B_4C particles for example, the centroid of each B_4C particle was recorded (Figure3.8(a)). In order to generate data for comparison with the actual distributions, an image of random distributions were created using a random number generator proposed by Park and Miller[74] (Figure3.9(a)), with the same image size and identical particles quantity as those on the mosaic image. Subsequently, Dirichlet tessellation was carried out on the sets of centroids on the sample image, as well as the random dots generated as shown in Figure3.8(b) and 3.9(b), in which the centroids are ultimately dilated by the same rate in all directions within their respective zones of influence until impingement occurs. A zone of influence is a boundary that is situated at an equal distance between a centroid and its neighbors. It should be noted that, for both tessellation images, edge cells are removed as microstructurally unrepresentative. Finally, the tessellation cell areas for both images were recorded by the image analyzer. The routine for characterization of particle distribution homogeneity is listed in Appendix C.

In order to quantitatively identify the distribution homogeneity, one promising parameter P has been extracted, which is based on the variance of the cell area distribution. The larger the value of P, the more non-homogeneous the particle distribution (random distribution P=1).

Variance of measured areas (μm^4):

$$V = \frac{1}{n}\sum_{i-1}^{n}(A_i - \overline{A})^2 \tag{3.1}$$

Variance of random distribution (μm^4):

$$V_{rand} = \frac{1}{n}\sum_{i-1}^{n}(A_{i-rand} - \overline{A}_{rand})^2 \tag{3.2}$$

Homogeneity parameter:

$$P = \frac{V}{V_{rand}} \tag{3.3}$$

where, $\overline{A}$ is the average of the measured cell area, $\overline{A}_{rand}$ is the average area of random distribution.

According to Equation (3.3), the homogeneity parameter P of B_4C particles (Figure 3.8(a)) is P_{B4C} =2.41, and P_{random}=1, which consistent with the corresponding microstructure of distribution.

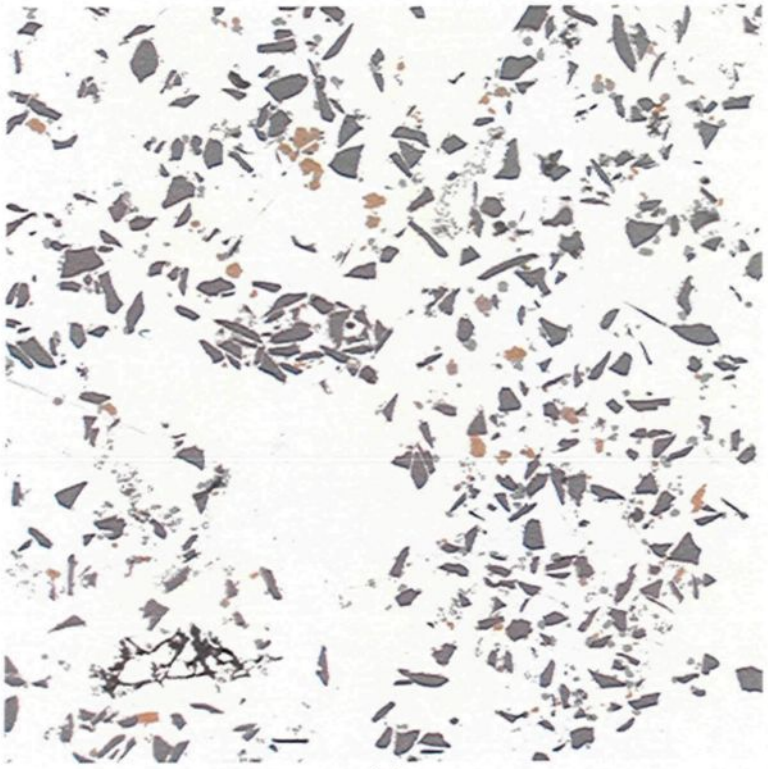

(a)

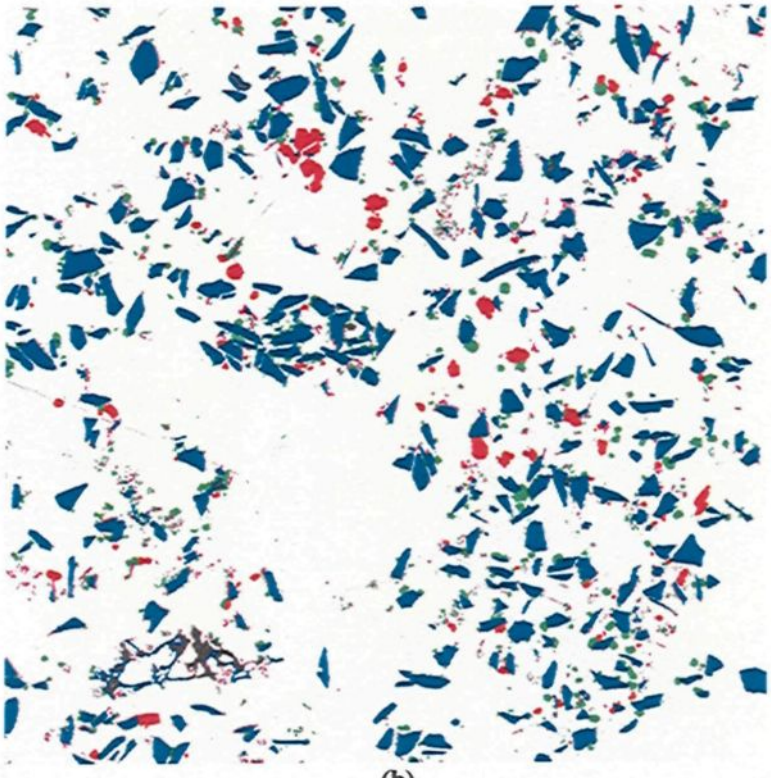

(b)

Figure 3.7: Sample image: (a) original image; (b) thresholding image.

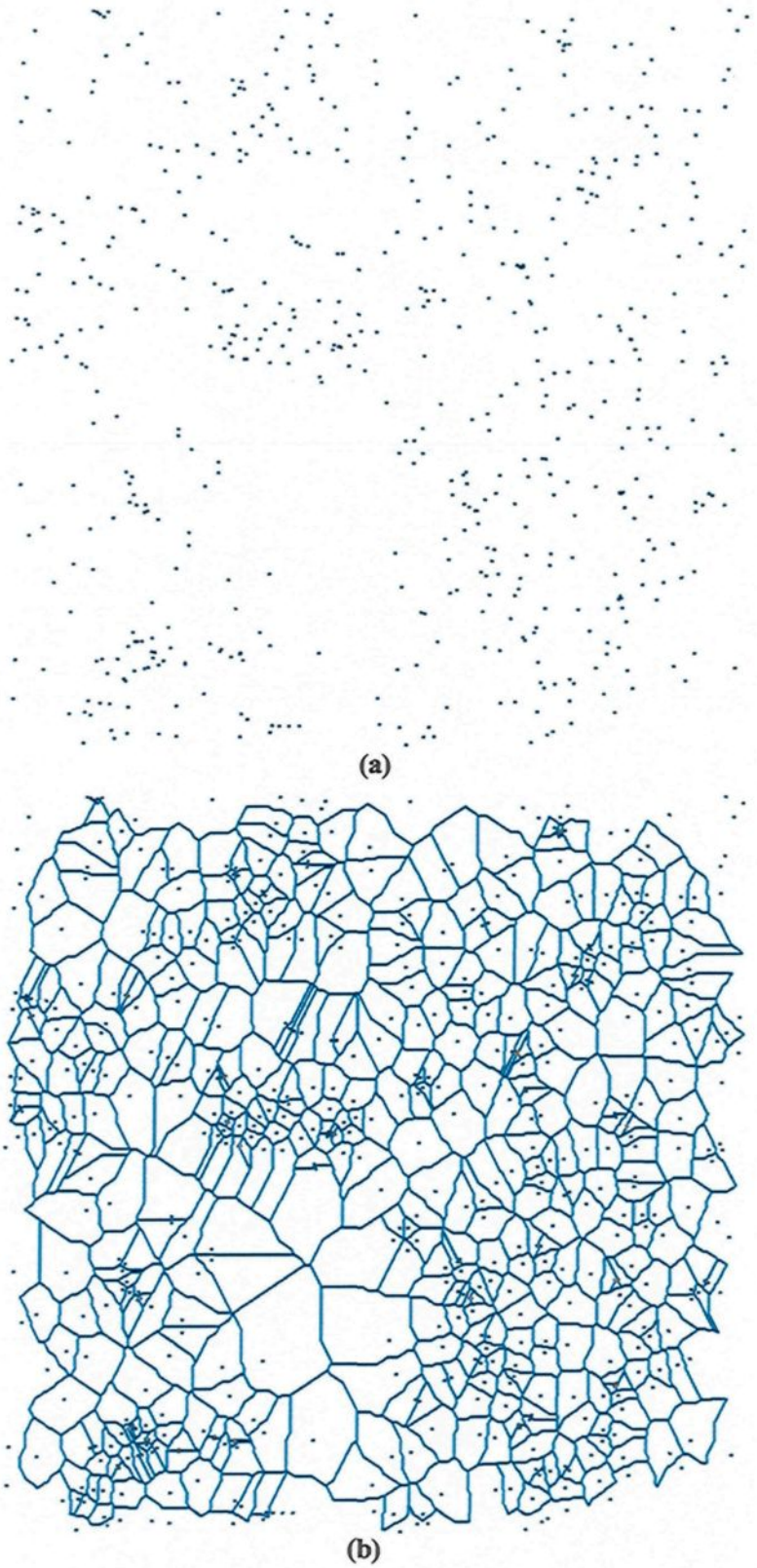

Figure3.8: Centroid of B_4C particles: (a) centroids image; (b) tessellated image.

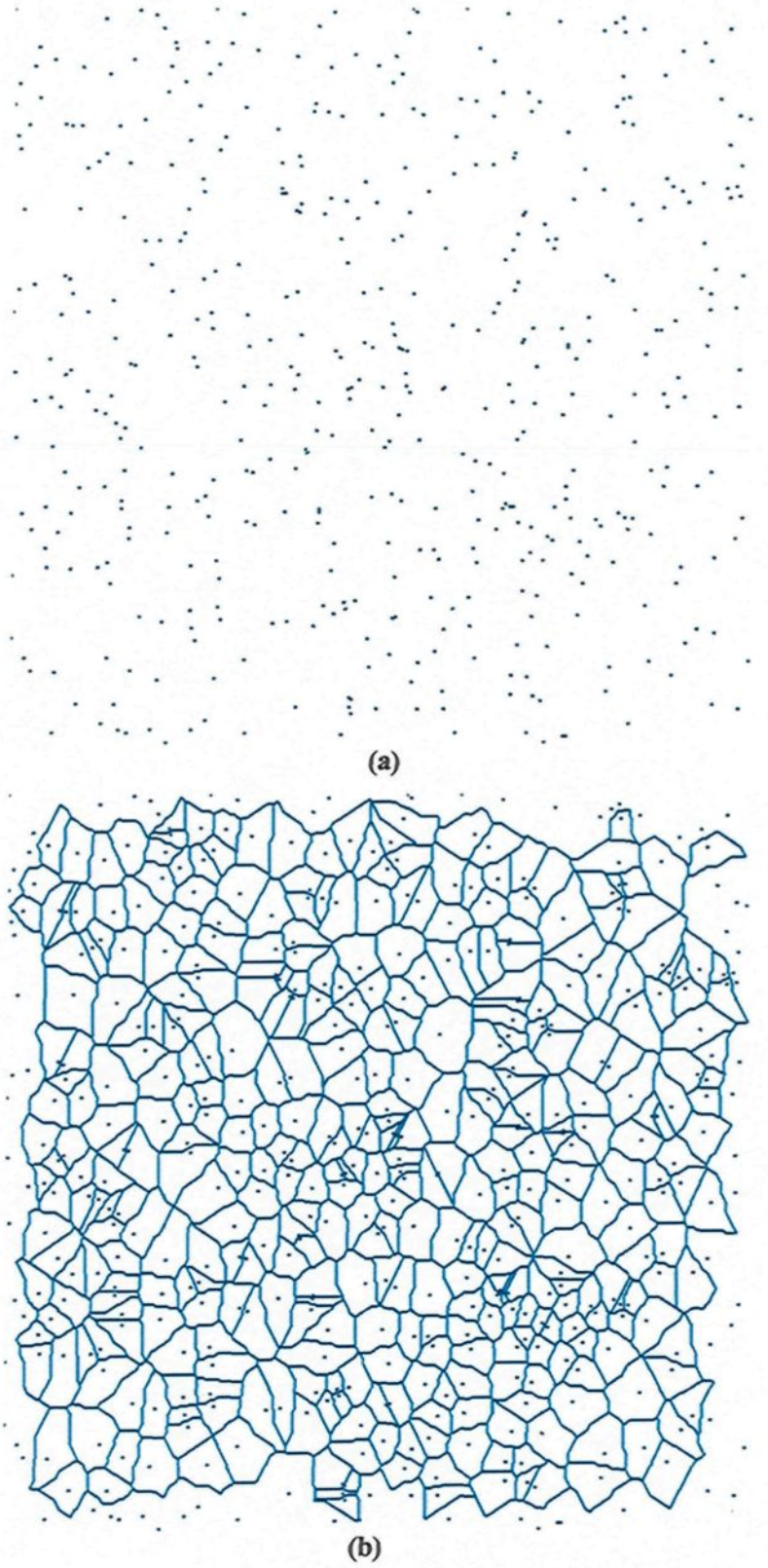

Figure 3.9: Random dots image: (a) original image; (b) tessellated image[75].

3.2.2.3 Particle agglomeration

An image analysis approach was proposed to identify two types of particle agglomerates in Al-B_4C metal matrix composites, particle clusters and particle networks induced by oxide films, in order to study the impact of the volume fraction of these particle agglomerates on the fluidity. The particle agglomeration phenomenon is more visible in fluidity samples during the fluid flow. Hence, the fluidity samples of Al-10 vol.% B_4C cast billets and extruded plates, in addition to Al-16 vol.% B_4C cast ingots and rolled sheets with holding times of 30, 60, 120, 330, 510 minutes were respectively transversely sectioned at different positions along the flow path respectively. The quantification of particle agglomerates was carried out at 200× magnification covering the entire 6 mm diameter round area of each fluidity sample.

Particle cluster

Since there was strong interfacial reaction between B_4C particles and the Al melt, the reaction-induced particles, Al_3BC and AlB_2, were produced during remelting. Of particular interest was that the neighboring particles might be joined together by the reaction-induced particles to form a dense cluster in the spatial structure, as illustrated in Figure3.10.

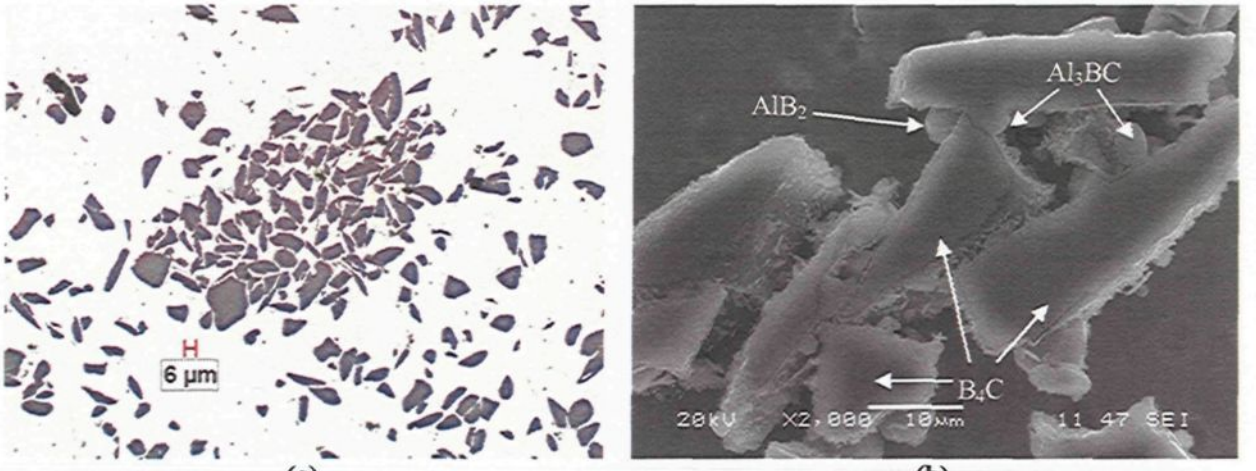

(a) (b)

Figure3.10: (a) An optical image of a cluster; (b) A secondary electron image (SEI) of a cluster in an etched fluidity sample with 510 min holding.

Our definition of a cluster of particles was one in which the "range of influence" of one particle overlapped with that of another. In an image analysis routine defining the range of influence might be achieved by dilating the identified particles by a certain amount. The required amount of dilation was somewhat arbitrary; hence caution must be exercised in selecting a suitable value. My approach to define this value was based on an actual examination of large numbers of clusters using optical microscopy and scanning electronic microscopy. From such 2D and 3D microstructural investigations of Al-B_4C composite samples, it was observed that particles were likely to form a cluster when their nearest boundary distance was within 1.08 µm (critical limit).

The main procedure to identify clusters in the image (at 200× magnification) consisted of the following steps. Firstly, all the particles themselves were identified within the image according to their intensity, hue and saturation optical parameters. The result was a binary image of the particles and the matrix (Figure 3.11(a)). One cycle of dilation was performed on all the particles, which means adding one pixel (1.08 µm)

around the contour of each particle. Those particles for which the influence range was within the critical limit value as mentioned above were overlapped with each other (Figure3.11(b)).The areas closed by the bridging of particles were filled to represent the formation of clusters as a whole mass. Secondly, six cycles of erode, which was a process opposite to dilation, were applied, followed by elimination of the non-cluster noises. Subsequently, to recover the original contour of particles after one cycle of dilation and six cycles erode of operations, five cycles of dilation were further executed. By this step, the clusters have been identified to some extent as shown by the thresholding area (Figure3.11(c)). To ultimately satisfy the condition for quantitative measurement, the particles touching the pre-identified clusters were reselected, followed by 5 cycles of closing operation and filling the internal holes. As well 3 cycles of convex hull operation were applied to selectively dilate the concave portions of the contour to make them smoother, usually in the transitional area of neighboring particles. This operation was most effective with small concavities. Applying the convex hull operation to a feature with few, large concavities, might significantly distort the feature since it would begin dilating in all directions once the concavities were eliminated. Hence caution should be taken. Consequently, a well indentified cluster was shown in Figure3.11(d), with the contour circled by the outermost particles' boundaries. Besides, due to the clusters were the agglomerates of B4C particles likely joined together by reaction-induced particles, in my definition, a cluster required at least three B4C particles. Any feature containing fewer than the number of B4C particles was removed from the set of clusters.

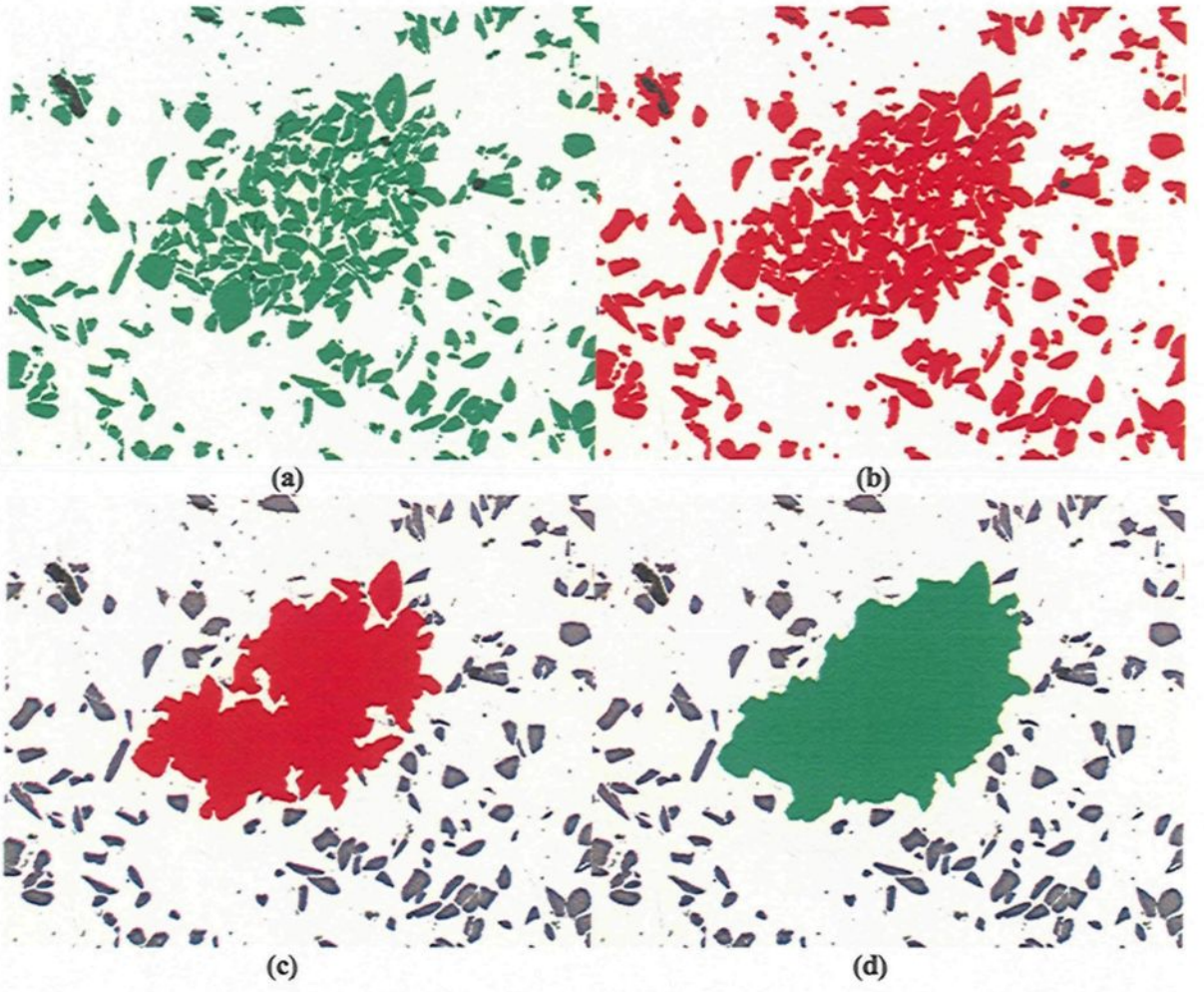

Figure 3.11: Steps of a particle cluster identification: (a) thresholding image; (b) dilated image; (c) pre-identified image; (d) identified image.

Particle network

Particle network induced by oxide films was identified simply according to the flow behavior of these particles that they were enclosed by the oxide films as a whole mass and occupied a much greater space during fluid flow. Through image analysis techniques, the particles in the optical image (at 200× magnification) , Figure3.12(a), which were enclosed by the circle of oxide film, were lassoed in along the thin oxide film to form a closed area, namely the effective area of the particle network as shown in Figure3.12(b). In addition, small discontinuous slices or line-shaped oxide films were neglected due to

the much less tendency to form particle networks in such cases. The routine for identification of particle cluster and network is listed in Appendix D and E. Finally, the volume fraction of particle clusters, as well as particle networks were quantitatively measured, for correlating with the fluidity evolution of the corresponding these Al-B_4C composite scrap samples.

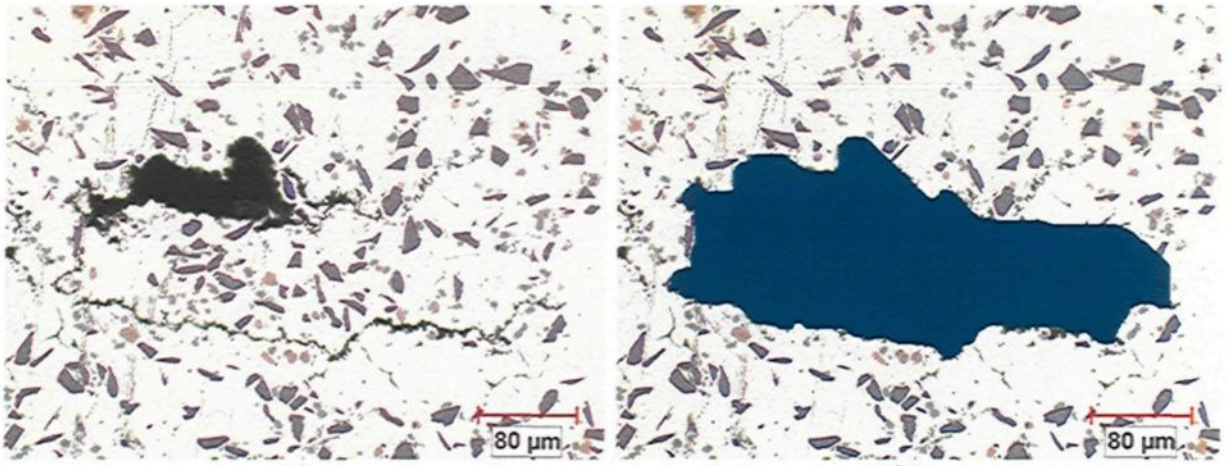

Figure 3.12: Steps of a particle network identification: (a) original image; (b) identified image.

3.2.2.4 Particle effective volume fraction

In Al-B_4C composites, B_4C and reaction-induced particles were not uniformly distributed in the Al matrix, as some of them formed particle segregates or agglomerates. Thus, a simple volume fraction measurement of particles could not truly reflect the flow resistance of solid particle segregation and agglomeration. To overcome this, a concept of the effective volume fraction of particle complexes was introduced. When several solid particles in the Al matrix were close enough, they likely moved as a whole mass during the fluid flow and occupied a much greater space than the sum of individual solid particles. For the particle segregation and agglomeration in the microstructure, three different cases were classified in the effective volume model: small particle aggregates,

dense particle clusters and particle networks induced by oxide films or reaction products. Therefore, to further investigate the contribution of particle segregations to the flow resistance, the effective volume fraction of the total solid particles (B_4C, Al_3BC, TiB_2, and AlB_2) at the flow end of fluidity samples of cast, extruded and rolled materials obtained after prolonged of holding times (30-510 min) were measured. These fluidity samples were transversely sectioned at the flow end and examined at 500× magnification over the entire 6 mm diameter round area using the image analyzer.

The solid particles in the micrographs of the composite were treated by image analysis techniques as illustrated in Figure3.13. The particle clusters and oxide film induced particle networks were characterized by the corresponding model introduced in the previous sections. Moreover, the identification method for small particle aggregates was the same as that for the particle clusters, i.e., when nearest boundaries distance of neighboring particles was within 1.08 μm, they were defined as a whole mass. This could be a complement to the particle clusters, which included the small agglomerates produced by several reaction products and B_4C particles (less than 3). From Figure3.13, it is also shown that extremely dispersed particles were not affected by the models and still keep their contour after the modeling. Finally, the effective volume fraction of solid particles was quantitatively measured by the image analyzer, consisted of the volume fraction of the three types of particle agglomerates and the volume fraction of the remaining individual particles. The routine for measurement of particle effective volume fraction is listed in Appendix F.

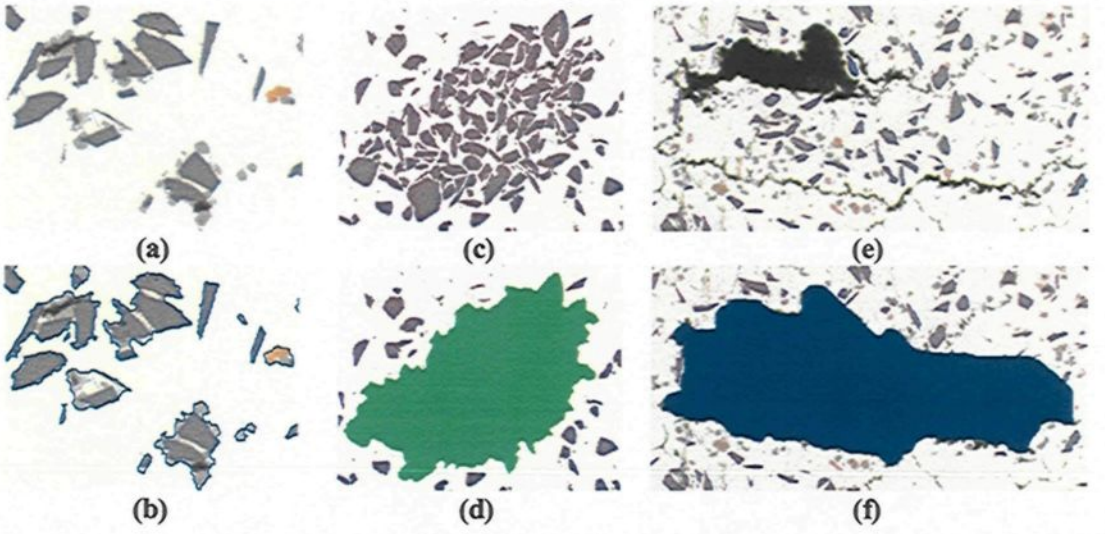

Figure 3.13: The effective volume models and the effective volume fraction measurements in the image analysis: a) original micrograph and (b) model image for small particle aggregates; c) and d) for a dense particle cluster; e) and f) for a particle network induced by oxide films or reaction products.

3.3 ELECTRON MICROSCOPY

A scanning electron microscope (SEM) was employed to study the spatial microstructure of oxide films and particle clusters and the influence of extrusion and rolling processes on microstructure of the reaction-induced particles, especially the TiB_2 layer.

CHAPTER 4

RESULTS AND DISCUSSION

CHAPTER 4

RESULTS AND DISCUSSION

4.1 CAST AND EXTRUDED RECYCLED MATERIALS (AA6063-10 VOL.% B_4C)

4.1.1 Fluidity evolution

The fluidity of Al-10 vol.% B_4C composite scrap in the form of cast billets and extruded plates was evaluated. Figure 4.1 shows the fluidity evolution of both materials for a long holding period (510 min). The fluidity of these materials declines with the increase in holding time. However, the fluidity decline rate of the two materials is different. At the start of the holding period, the fluidity of the extruded plates is slightly higher than that of the cast billets. With prolonged holding time, the fluidity of the extruded plates decreases very slowly. In comparison, the fluidity of the cast billets decreases much more quickly over the same holding time range. Moreover, the fluidity deterioration rate of the cast billets is not constant. In the first stage, the flow length of the cast billets decreases rapidly from roughly 55 to 40 cm for holding time up to 150 min, which represents approximately 90% of the total decrease in fluidity. After this period, the fluidity decline rate slows down remarkably. The continuous decrease of fluidity indicates that the rheological properties of the composite melt had changed during the holding period.

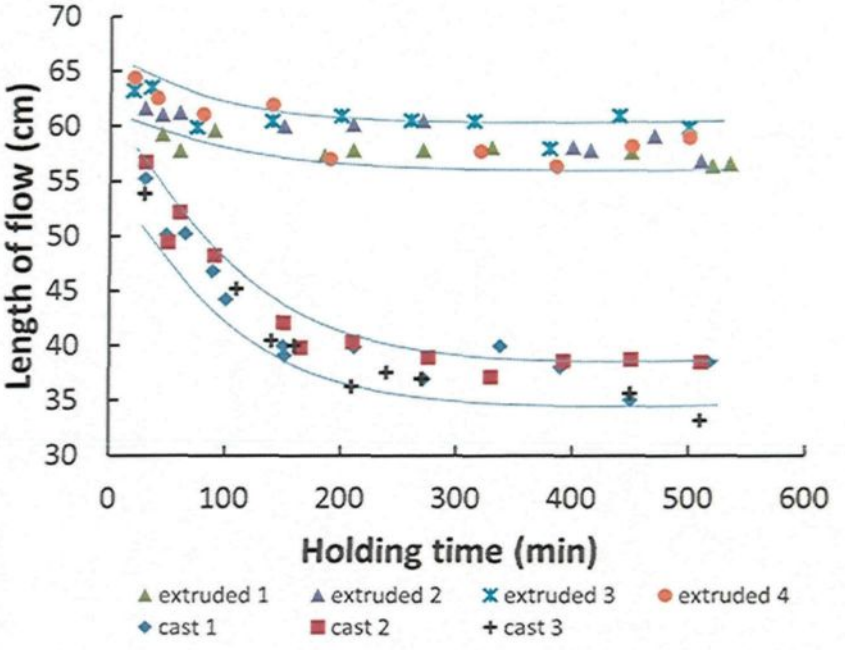

Figure 4.1: Fluidity evolution of cast and extrusion Al-10 vol.% B_4C MMCs.

4.1.2 Original scrap materials

4.1.2.1 Microstructure of B_4C and reaction-induced particles

In order to understand the flow behavior of the composites, the microstructure of the original scrap materials derived from the cast billets and extruded plates were examined. Other than B_4C particles, the reaction-induced particles, mostly Al_3BC and TiB_2, are observed in both materials (Figure 4.2). A few AlB_2 particles are occasionally found in the matrix of these materials. In the cast billets, these reaction-induced particles are mostly attached and close to the B_4C particles to form a layer around the B_4C particle surfaces, while many of these particles in the extruded plates are separated from the B_4C particle surface due to the severe hot deformation, which occurred during the extrusion process.

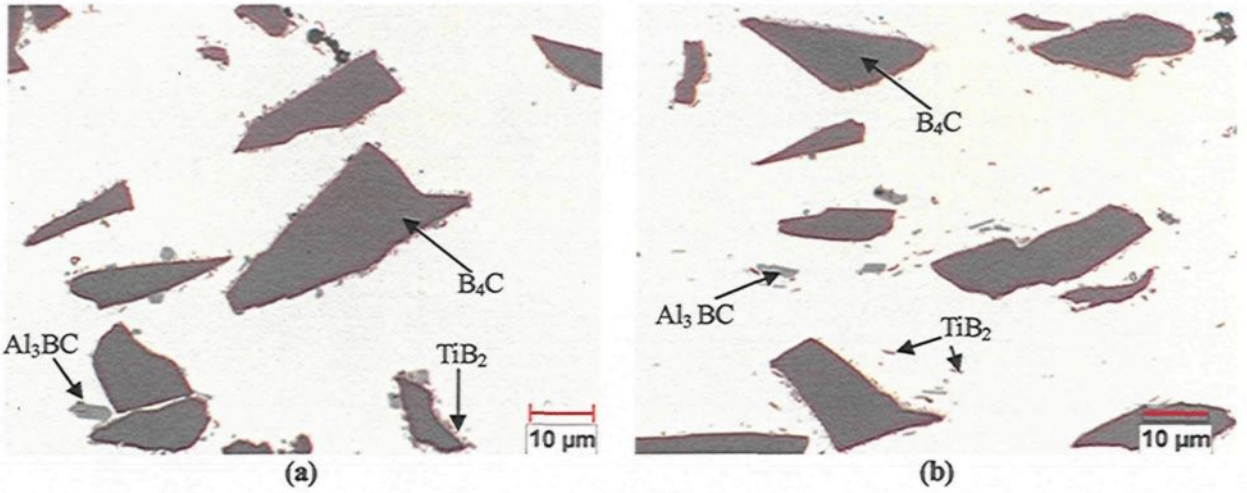

Figure 4.2: Micrographs of Al-10 vol.% B_4C composite scrap: (a) cast billets; (b) extruded plates.

4.1.2.2 Microstructure of particle agglomerates

Particle clusters, a dense solid particle complex, could be observed in both the cast billets and the extruded plates (Figure 4.3). However, comparing the cluster observed in the two scrap materials, many particle clusters in the extruded plates are broken down along the extrusion direction and appear much less dense than those observed in the cast billets. The particles in the original clusters are more or less separated from each other. Due to the deformation related to the extrusion process, it is observed that the amount and size of the clusters in the extruded plates are considerably less and smaller than those found in the cast billets.

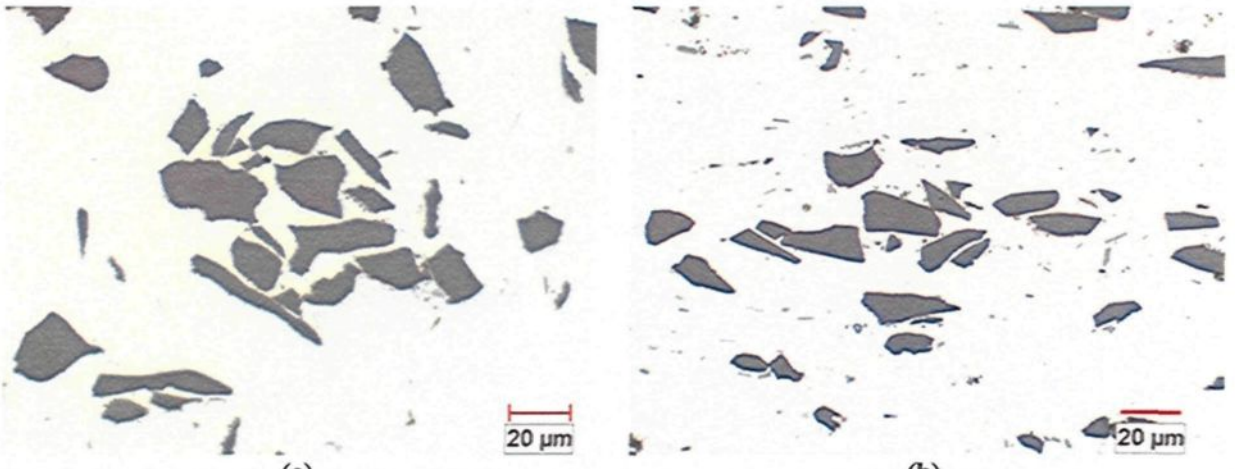

Figure 4.3: Particle clusters: (a) in cast billets; (b) in extruded plates.

Oxide films are one type of defects in Al-based metal matrix composites. These films can also be observed in both types of scrap material (Figure 4.4). However, in the cast billets, some B_4C particles and reaction-induced particles are enclosed by oxide films and can easily form particle networks which will act as a whole mass moving in the liquid during the remelting. On the other hand, in the extruded plates the oxide films are squeezed and broken down along the extrusion direction. Under heavy deformation of the extrusion process, these oxide films become discontinuous and tiny slices which will hardly have a tendency to form particle networks in the remelting process.

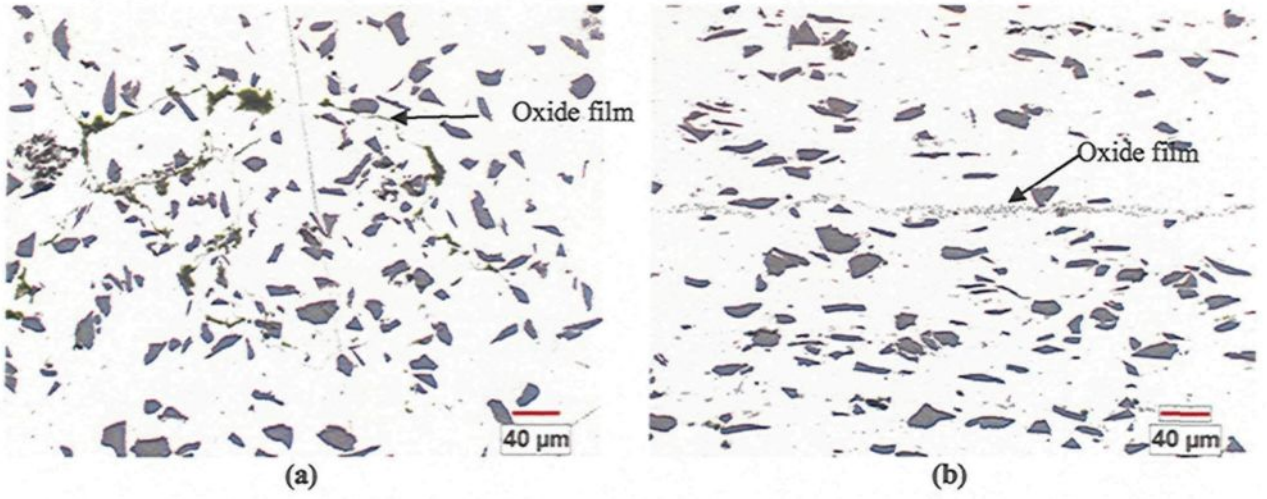

Figure 4.4: Oxide films: (a) in cast billets; (b) in extruded plates.

4.1.3 Crucible samples

4.1.3.1 Microstructure of B_4C and reaction-induced particles

Figure 4.5 gives an example of the microstructural evolution of the crucible samples for 510 minutes holding time. In both materials, the amount and size of Al_3BC and AlB_2 are larger than those observed in the original scrap materials. However, it is interesting to notice that, in the cast billet samples, most of the reaction-induced particles are still attached and close to the B_4C particles after remelting and holding, indicating a strong tendency to form solid particle aggregates. On the other hand, in the extruded plate samples, many of those particles are separated from the B_4C particles and more or less uniformly distributed in the matrix. As previously mentioned, many small reaction-induced particles are separated from the B_4C particles in the original extruded plates. These pre-existing particles might provide favored sites for further precipitation and growth of Al_3BC and AlB_2 during remelting and holding periods. Consequently, after remelting, the extruded materials will exhibit a more uniform distribution of all the solid particles in the matrix.

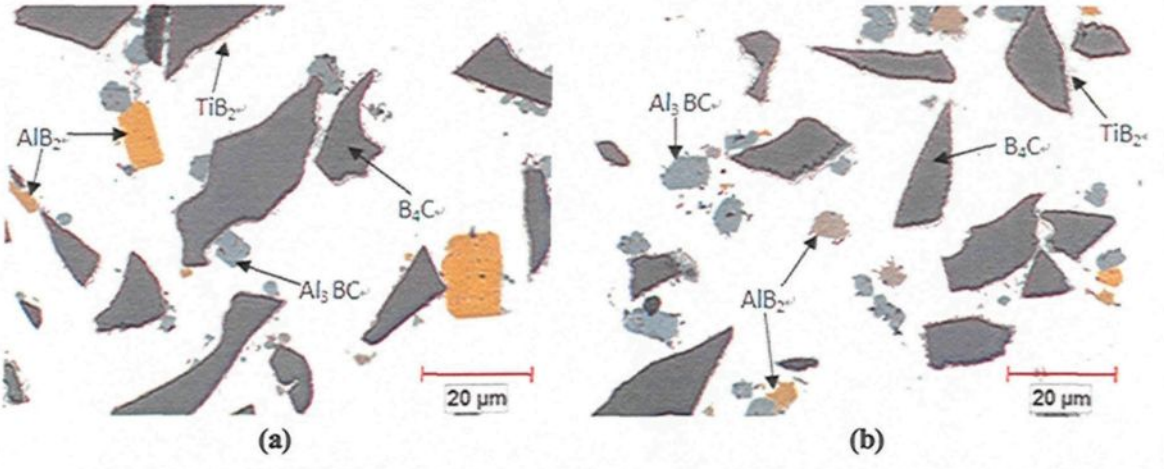

Figure 4.5: Micrographs of the crucible samples with 510 minutes holding time: (a) cast billets; (b) extruded plates.

4.1.3.2 Microstructure of particle agglomerates

Figure 4.6 shows the particle clusters of cast and extruded materials after 510 min of holding. It is found that the B_4C particles in the clusters are bonded densely by the reaction-induced particles. Particle clusters observed in the cast billets were formed during the initial DC casting and remelting. Although the extrusion process can considerably improve the uniformity of particle distribution, a small proportion of particle clusters may still exist or be formed during very long period holding.

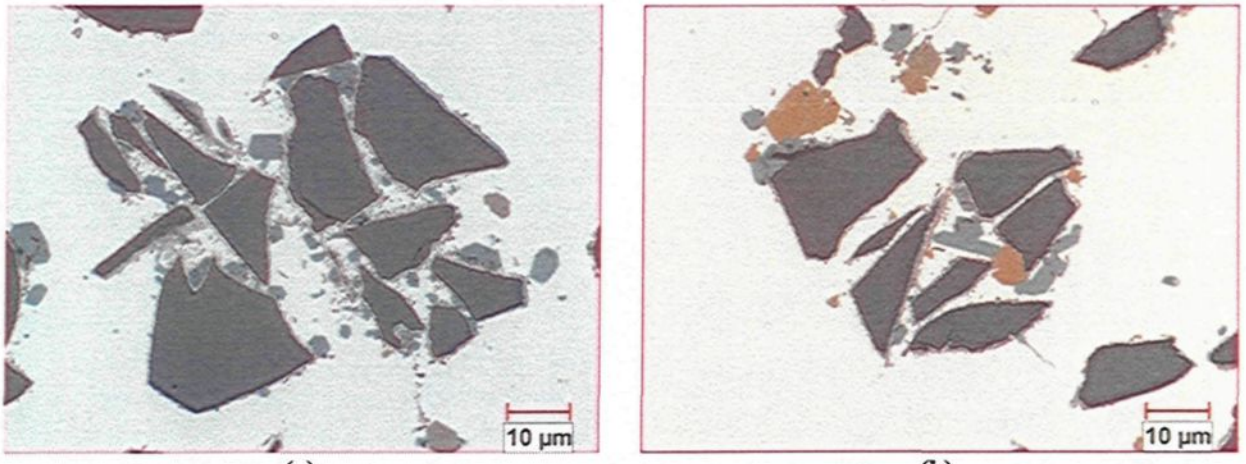

(a) (b)

Figure 4.6: Particle clusters of 510 min holding crucible samples of: (a) cast billet; (b) extruded plate.

In addition, oxide films have been observed in the two materials as shown in Figure 4.7. It is found that the B_4C and reaction-induced particles are trapped by or attached to the oxide films forming particle networks, as demonstrated by the SEI images as shown in Figure 4.8. In these images, the oxide films connect the particles in a circle or extend between particles. In particular, the majority of particles attached to the oxide film are Al_3BC or AlB_2 as shown in Figure 4.7(c), in which the oxide films appear to act as favored sites for further precipitation and growth of reaction-induced particles.

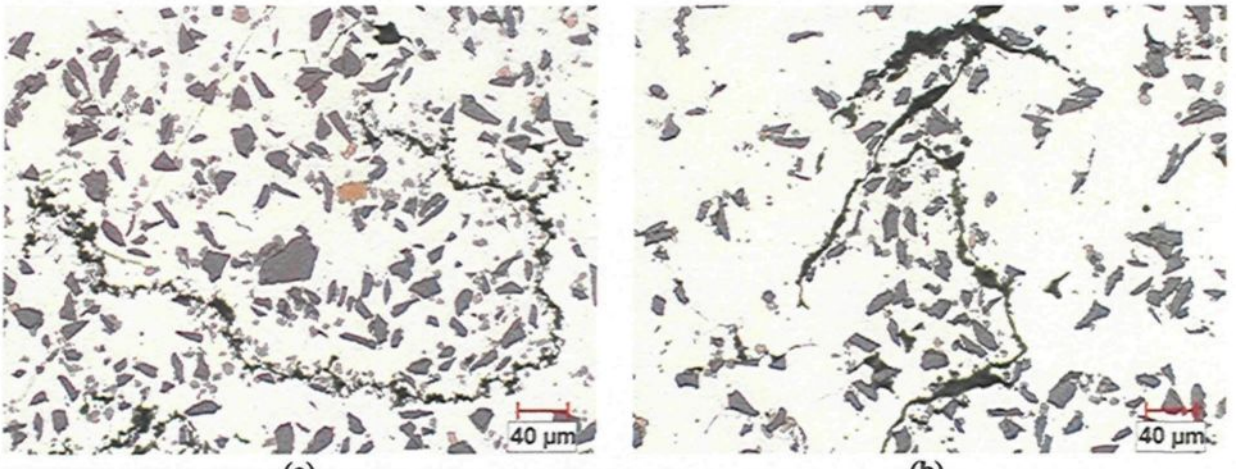

(a) (b)

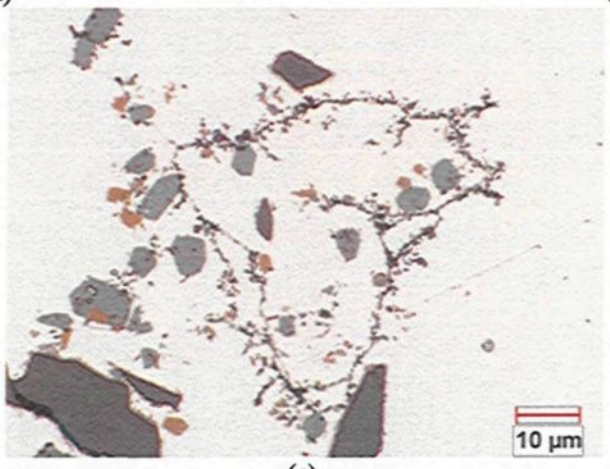

(c)

Figure 4.7: Oxide film induced segregation of 510 min holding etched crucible samples of: (a) extruded plate; (b) (c) cast billet.

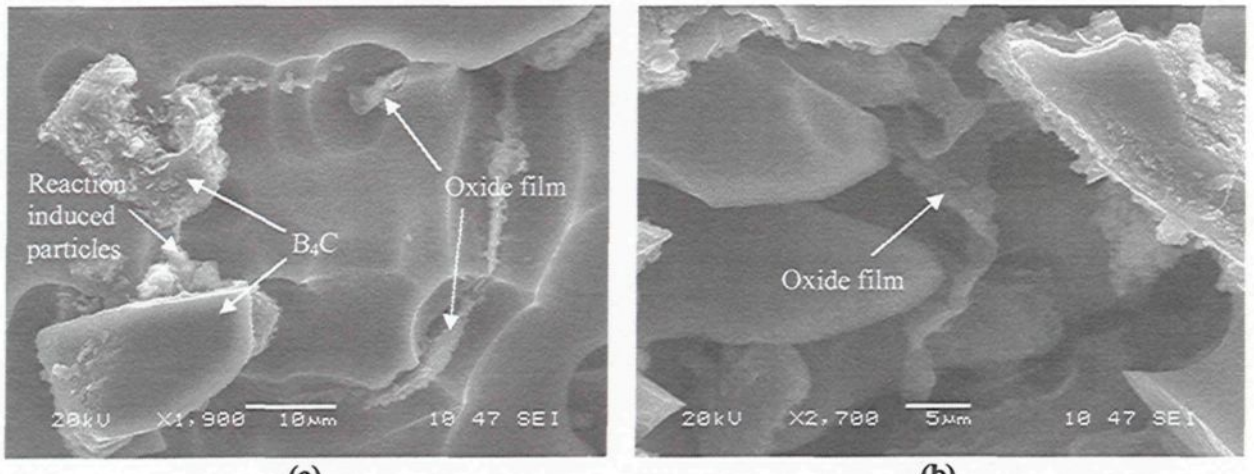

(a) (b)

Figure 4.8: Secondary electron images (SEI) of etched crucible samples obtained after 510min holding time: (a) circular oxide film; (b) extended oxide film.

However, as mentioned previously, some of the oxide films in extruded plates are broken into tiny slices or folded after the extrusion process, such films are thus hardly expected to form particle networks during remelting, as shown in Figure 4.9.

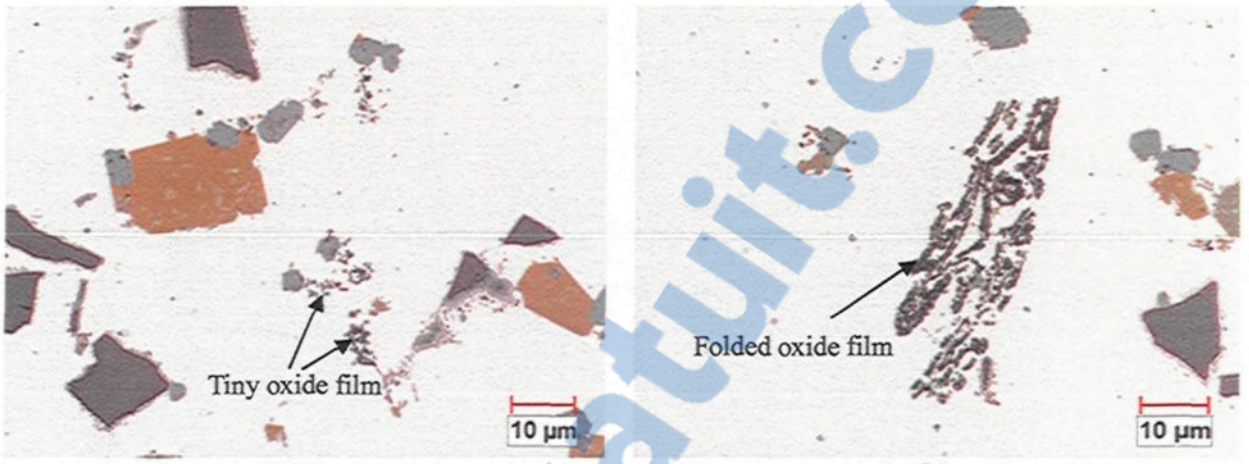

Figure 4.9: Oxide films in the crucible sample of extruded plate scrap with 510 min holding time: (a) tiny oxide films; (b) folded oxide films.

4.1.3.3 Quantitative analysis of B_4C and reaction-induced particles

Particle Volume fraction

During the remelting and holding times, interfacial reactions continue in both cast and extruded materials. Table 4.1 shows the volume fraction of B_4C particles and reaction products obtained as a function of holding time in the crucible samples, which represents the particle behavior of the melt at the entrance of the fluidity samples.

Table 4.1:Volume fraction of B_4C particles and reaction-induced particles with holding time

Composite	Holding time (min)	Volume fraction (%)				
		Total particles	B_4C	Al_3BC	AlB_2	TiB_2
Cast billet	30	15.31	11.48	1.00	0.07	1.66
	90	15.39	11.13	1.22	0.15	1.64
	150	16.43	11.22	1.55	0.46	1.78
	510	18.09	10.58	2.32	1.26	1.83
Extruded plate	30	16.26	11.82	1.43	0.22	1.60
	90	16.51	11.16	1.69	0.54	1.70
	150	17.44	11.66	1.81	0.97	1.63
	510	18.96	10.63	2.76	1.64	1.84

Firstly, it should be mentioned that TiB_2 is formed before remelting. From Table 4.1, it is reasonable to assume that Ti is no longer available in the matrix after remelting, since the amount of TiB_2 remains almost constant in the cast and extruded composites during holding.

It is evident that the total volume fraction of particles increases slowly with the increase in holding time. This increase is contributed by the increasing amount of the reaction-induced particles, namely Al_3BC and AlB_2, as the fraction of B_4C decreases gradually with holding time due to the decomposition process. Nevertheless, there is no remarkable difference in the total particle amounts in both cast and extruded materials with respect to the holding time, taking into consideration of the deviation of the image analysis measurements induced from the quality of sample preparation and equipment errors.

Particle distribution

Firstly, to assess the volume fraction of reaction-induced particles attached to the

B4C particles in cast and extruded materials, the ratios of Al_3BC and AlB_2 particles (attached to B_4C particles) to the B_4C particles with holding time were quantitatively analyzed as respectively illustrated in Figures 4.10 and 4.11.

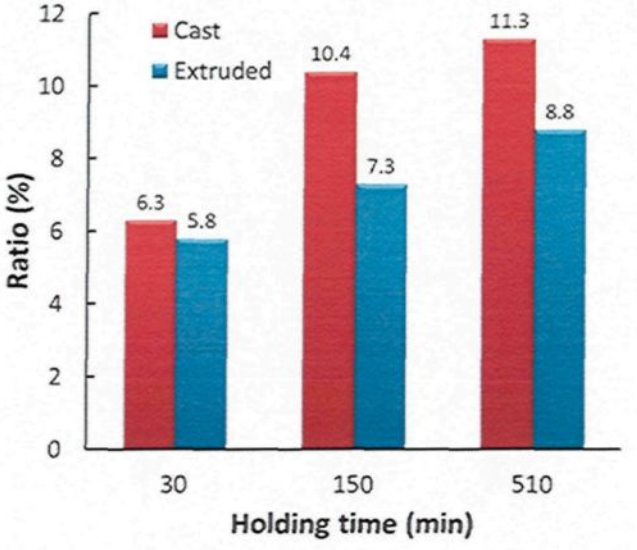

Figure 4.10: The ratios of Al_3BC particles (attached to B_4C particles) in cast and extruded composites with holding time.

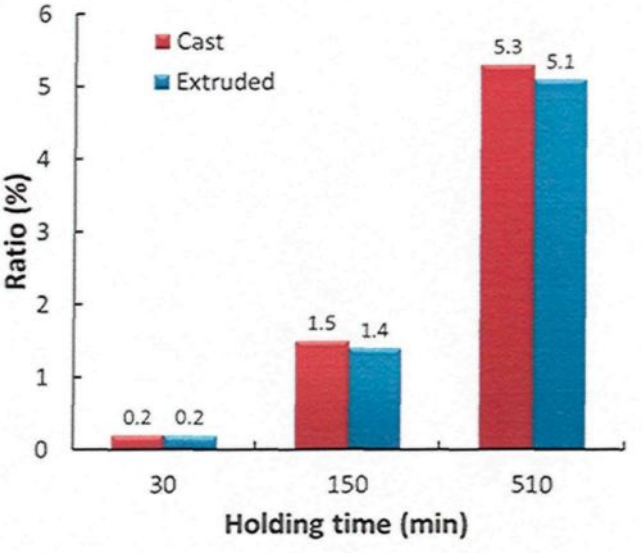

Figure 4.11: The ratios of AlB_2 particles (attached to B_4C particles) in cast and extruded composites with holding time.

It is evident that in both materials, the ratios of Al_3BC and AlB_2 particles attached to B_4C particles increase dramatically with the increase in holding time. On passing from a holding time of 30 to 510 minutes, the Al_3BC particles attached to B_4C particles in cast billet samples display a much higher ratio than the extruded plate samples. Meanwhile, the ratios of AlB_2 attached to B_4C in the cast billet samples are slightly higher than those in the extruded plate. B_4C particles are likely to form particle agglomerates by the interconnection of reaction-induced particles. Hence, the higher ratios of cast billets indicate a stronger tendency to particle agglomeration during holding.

In Figure 4.12, the evolution of particle distribution homogeneity in cast and extruded samples with holding time is separately characterized by a homogeneity parameter P. The larger the value of P, the less homogeneous will be the particle distribution (random distribution P=1). In both materials, with the increase of holding time, the reaction-induced particles, Al_3BC and AlB_2 are distributed more inhomogeneously. Meanwhile, the distribution of B_4C particles becomes nonuniform after remelting. However, it is interesting to notice that, in the cast billet samples, the homogeneity of solid particle distribution is remarkably worse than that in the extruded plate samples after remelting and holding, indicating that there is a strong tendency in the cast billets to form solid particle aggregates, based on the fact that more reaction-induced particles appear attached as well as close to the B_4C particles.

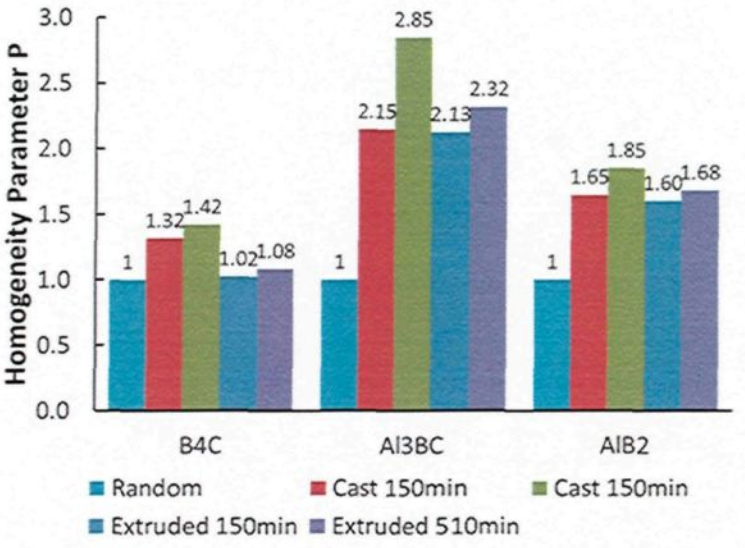

Figure 4.12: Evolution of particle distribution homogeneity in cast and extruded samples with holding time.

4.1.4 Fluidity samples

4.1.4.1 Quantitative analysis of particle agglomerates

The volume fraction induced by particle clusters and particle networks at the flow end of the fluidity samples is displayed in Figure 4.13. Results show that these two types of particle agglomerates increase with the increase in holding time, and play an important role on the flow resistance of the molten metal during the fluidity testing, due to their large contribution to the effective volume of particles. Moreover, it could clearly be seen that the volume fractions of both the particle clusters and the oxide film-induced particle networks in the cast billet samples are higher than those in the extruded plates, which indicates that the cast materials have a greater tendency to particle agglomeration than the extruded materials during holding.

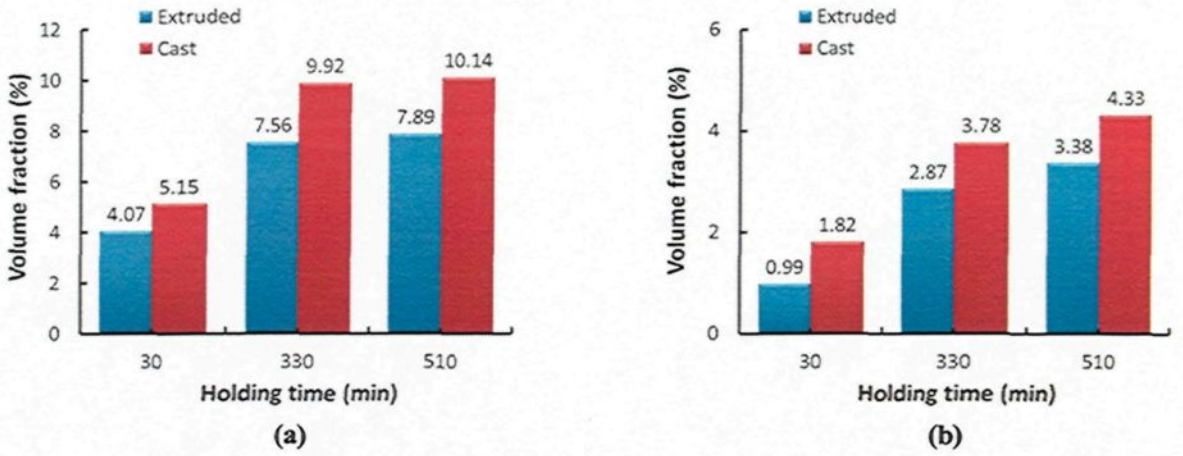

Figure 4.13: (a) Volume fraction of particle clusters; (b) Volume fraction of particle networks induced by oxide films in cast billet and extruded plate samples with holding time.

4.1.4.2 Quantitative analysis of B_4C and reaction-induced particles

Particle effective volume fraction along flow path

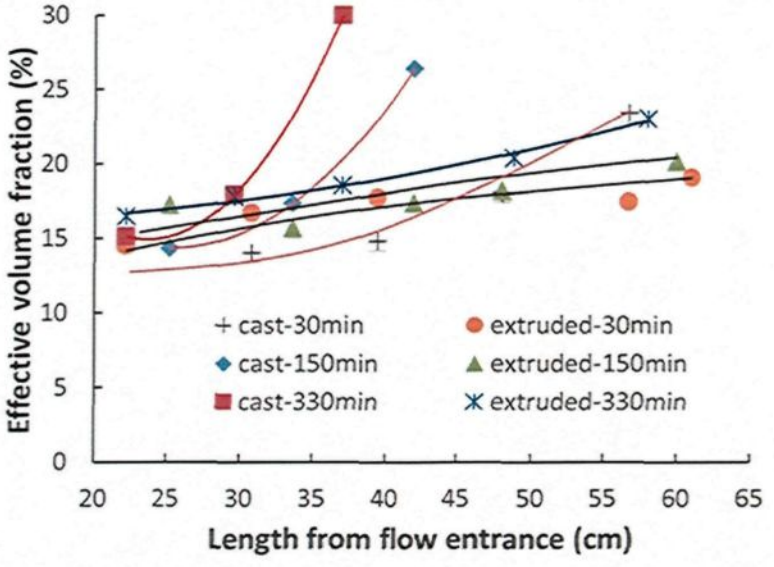

Figure 4.14: Evolution of particle effective volume fraction of the fluidity samples with respect to holding time.

Figure 4.14 shows the effective volume fraction of solid particles along the flow

path in the fluidity samples of both cast and extruded materials for different holding times. In general, the effective volume fraction increases along the flow path. The nearer to the flow end of the fluidity sample is, the higher is the effective volume fraction. This suggests that the particle agglomerates are enriched towards the flow end. Shortly after remelting (30 min holding time), the cast billet sample shows a higher effective volume fraction towards the flow end than the extruded plate sample, which gives an indication that greater particle segregation and agglomeration exist in the cast materials during the initial holding period. With increased holding times (150 and 330 minutes), the cast billet samples display a much higher rate of increase of the effective volume fraction along the flow path than the extruded plate samples. It is evident that the process of particle segregation and agglomeration accelerate with the increase in holding time in the cast materials, leading to a rapid increase in the flow resistance. On the other hand, the effective volume fraction of extruded materials increases only slightly with holding time, which corresponds well with the slight decrease in the fluidity observed with the holding time. This may probably be related to the uniform particle distribution and the absence of the continuous oxide films in the extruded materials. As the amount of the total particles in both materials is almost the same, it is reasonable to believe that particle segregation and agglomeration are the dominant factors influencing the fluidity.

Particle effective volume fraction at flow end

Figure 4.15(a) showed the volume fraction of the total solid particles (B_4C, Al_3BC, TiB_2, and AlB_2) at the flow end of fluidity samples of cast and extruded materials as a function of the holding time. In general, the volume fraction of the solid particles increases with prolonged holding time, leading to a continuous decrease of fluidity.

However, shortly after remelting (30min), the volume fraction of the cast billet sample is 3.23% higher than that of the extruded plate. With the increase of holding time, the cast billet still possesses a higher amount of particles, and shows 4.56% higher than extruded plate at 510 min. Nevertheless, the small varied difference in volume fraction with holding time between the two materials may not be sufficient to explain the fluidity evolution of both materials after a long time holding of 510 min.

To further understand the fluidity behavior and take into consideration of the contribution of particle segregations to the flow resistance, the effective volume fraction of both materials are measured and the values are shown in Figure 4.15(b). It is clearly noted that for both materials, the effective volume fraction increases with holding time, which corresponds well with the decrease observed in the fluidity. Further, at the start of holding (30min), the effective volume fraction of the extruded plate samples is slightly lower than that of the cast billet samples. With increase in holding time, the effective volume fraction of the extruded plate samples increases relatively slowly, whereas that of the cast billet samples increased more quickly in comparison. At 510 min holding time, the effective volume fraction of cast billet sample is as much as 8% higher than that of the extruded plate sample, resulting in a decrease in fluidity of about 18%. Moreover, the increase in the effective volume fraction of the cast billets does not occur at a constant rate. In the first stage, the effective volume fraction of the cast billets increases rapidly from roughly 23 to 28% (for holding times of up to 150 min), which represents approximately 65% of the total increase observed with 510 min of holding time. After this period, the rate of increase of the effective volume fraction slows down gradually. Therefore, the flow length decreases with the increase in holding time due to the increase

of solid particles formed. Consequently, the fluidity of the cast billet samples decreases faster than that of the extruded plate samples due to the faster increase in particle effective volume fraction in these samples.

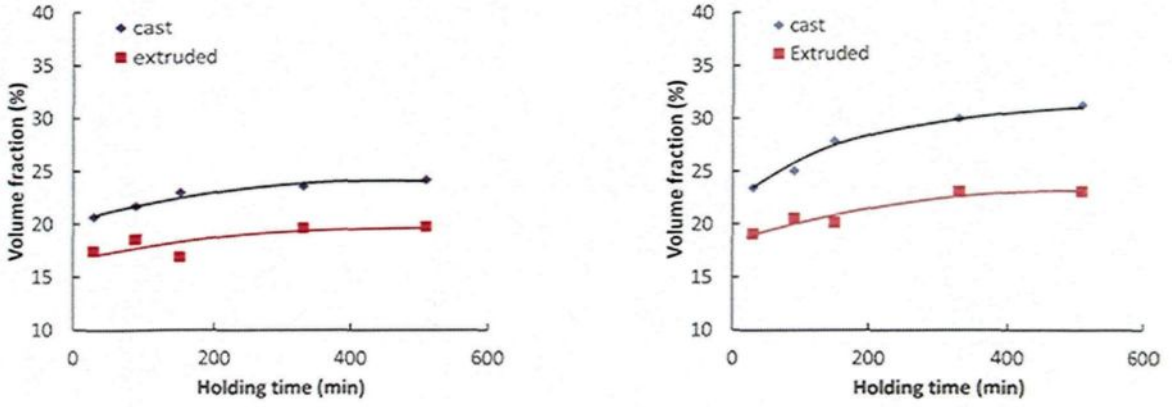

Figure 4.15: (a) Particle volume fraction; (b) particle effective volume fraction at the flow end of fluidity samples with holding time for cast and extruded materials.

4.1.5 Mechanism of flow arrest and explanation of fluidity evolution

In the literature, the mode of solidification of solute-rich long freezing range alloys was introduced by Flemings et al. and Campbell [12,13]. They proposed that fine equiaxed grains nucleate at the tip of the flowing stream and are carried downstream with the flowing metal (Figure2.7). Nucleation continues and the fine grains grow rapidly as flow progresses. When a critical concentration of solid is reached at the leading tip of flowing steam, then the viscosity rises rapidly and flow ceases abruptly [12].

In addition, S.G. Ward et al. [75] measured the relative viscosity as a function of volume concentration for irregularly-shaped powders in aqueous solutions, as shown in Figure 4.16. It may be observed that, for all powders of various sizes, when the particle volume concentration is over 20%, the relative viscosity increases significantly.

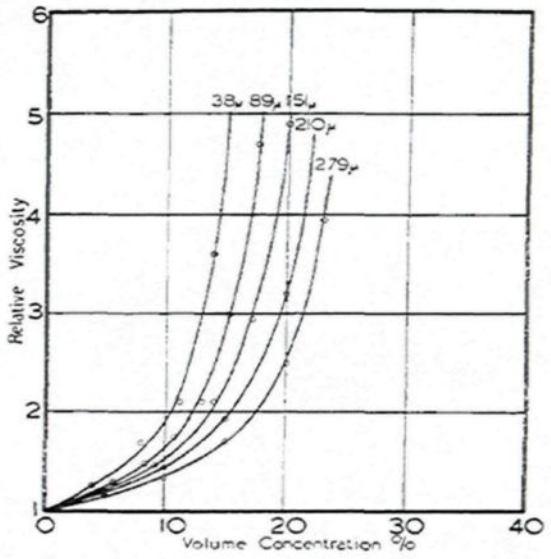

Figure 4.16: Relationship between relative viscosity and volume concentration of powders of various mean statistical diameters in aqueous solutions [75].

In Al-10 vol.% B_4C composite, the particles, as well as particle clusters and oxide film induced aggregations concentrate toward the center of the cross section and are carried downstream with the flowing Al melt, enriched to a very high concentration at the flow end.

Furthermore, the solidification microstructure of longitudinal section near the fluidity sample tip is shown in Figure 4.17, which shows the same solidification mode of composites as the solute-rich alloys (Figure2.7), flow ceasing at tip due to the high concentration of solid phases associated with some porosities.

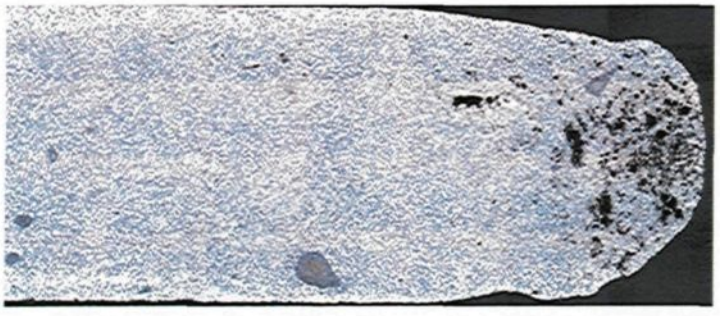

Figure 4.17: Microstructure of longitudinal section near the fluidity sample tip of Al-10 vol.% B_4Ccastbillet obtained after 510 min holding time.

The composite with high volume fraction particles and the solute-rich alloys have the same flow arrest mechanisms, which is due to the concentration of solid phases at the flow tip reaching a critical value, λ. However, as for the composites, the solid phases at the tip consist of two parts, solid equiaxed grains formed during flow, and the solid particles, viz. the parameter λ can be deduced as following,

$$\lambda = \lambda_g + \lambda_p \quad (4.1)$$

where,

λ_g : Concentration of solid grains

λ_p : Concentration of solid particles (effective volume fraction)

All the fluidity tests of cast and extruded composite materials were carried out under the same experimental conditions. Therefore, the major factors affecting the fluidity [12], including the heat content, heat transfer, metal velocity, and the mode of solidification were the same. Moreover, the critical value, λ, for both cast and extruded Al-10 vol.%B_4C composites is the same. The flow lengths (fluidity), particle effective volume fractions at flow tips of cast and extruded composites are shown in Table4.2.

Table 4.2: The flow lengths, particle effective volume fractions at flow tips.

Composite		Holding time (min)				
		30	90	150	330	510
Cast billet	flow length L_f (cm)	56.7	48.2	42.1	39.9	38.5
	Particle effective volume fraction λ_p (%)	23.41	25.04	27.82	29.98	31.27
Extruded plate	flow length L_f (cm)	61.6	59.6	60.0	58	56.8
	particle effective volume fraction λ_p (%)	19.07	20.52	20.14	23.05	23.09

It is found that either cast or extruded composites, the particle effective volume fraction observed at the tips of fluidity samples decreases with the increase of fluidity. This is because with the increase of flow length in the channel, the solid grains carried downstream to the flow tip would be more, viz, λ_g is higher when the flow stops; flow ceases when the concentration of solid phases achieves the critical solid concentration value, λ. Thus the concentration of solid particles, λ_p, is lower when λ_g is higher. In other words, an increase in the particle effective volume fraction indicates a decrease in fluidity.

As for cast ingot samples, the fluidity varies from 56.7 to 38.5 cm with the holding time ranging from 30 to 510min, and the particle effective volume fraction varies from 23.41% to 31.27%. The flow lengths differ by 18.2 cm, corresponding to the concentration difference of 7.86%.

Considering the extruded plate samples, the fluidity varies from 61.6 to 56.8 cm with the holding time ranging from 30 to 510 min, and the particle effective volume fraction varies from 19.07% to 24.09%. The flow lengths differ by 4.8 cm, corresponding to the concentration difference of 5.02%.

Comparing the fluidity of cast and extruded composite melts at 30 min and 510 min holding times, respectively, the flow lengths are seen to differ by 4.9 and 18.3 cm corresponding to concentration differences of 4.34% and 8.18%. The larger difference in particle concentrations together with the corresponding flow lengths confirms that the fluidity of the extruded plate materials is higher than that of cast billets during melt holding.

In addition, the particle concentrations of cast ingot at 30min and extruded plate at 510min show little difference, 23.41% vs. 23.09%, corresponding to approximately the same flow lengths, 56.7cm and 56.8cm, respectively, which implies that materials with the same concentration of particles have similar fluidity.

During the fluidity testing, it was observed that the small particle aggregates, clusters and networks had a tendency to migrate to the center of the section and toward the flow end of the fluidity samples. Due to the high tendency of particle agglomeration in the cast materials, there were much more particles enriching at the flow ends of the fluidity samples corresponding to the cast billet scrap than in the extruded scrap samples. When the effective volume fraction of the particles plus the solidified aluminum reached a critical level at the flow end, the viscosity of the melt rose rapidly and the flow stopped abruptly. Therefore, the flow length of the cast scrap sample was shorter than that of the extruded scrap sample. When using the remelting process for reuse of the valuable composite materials, it can be expected that the recyclability of scrap obtained from extruded plates, in terms of fluidity and melt quality, will be better than that of cast billets due to a more uniform particle distribution and the presence of less particle agglomerates in the former.

4.2 CAST AND ROLLED RECYCLED MATERIALS (AA1100-16 VOL.% B_4C)

4.2.1 Fluidity evolution

The fluidity of Al-16 vol.% B_4C composite scrap in the form of cast ingots and rolled sheets was evaluated. Figure 4.18 shows the fluidity evolution of both materials for a holding period of 150 min. The fluidity of these materials declines sharply with the increase in holding time. However, at the beginning of the holding time, the fluidity of the rolled sheets is found to be slightly higher than that of the cast ingots. With the increase of holding time, the fluidity of both the rolled sheets and cast ingots decreases significantly. The flow lengths of the two materials are almost the same after 90 min holding. The fluidity continues decreasing until the fluidity is too poor for carrying out a test (150 min). For prolonged holding times of 90 min, the fluidity deterioration rate of rolled sheets is more or less the same as the cast ingots, showing a similar decreasing tendency of fluidity.

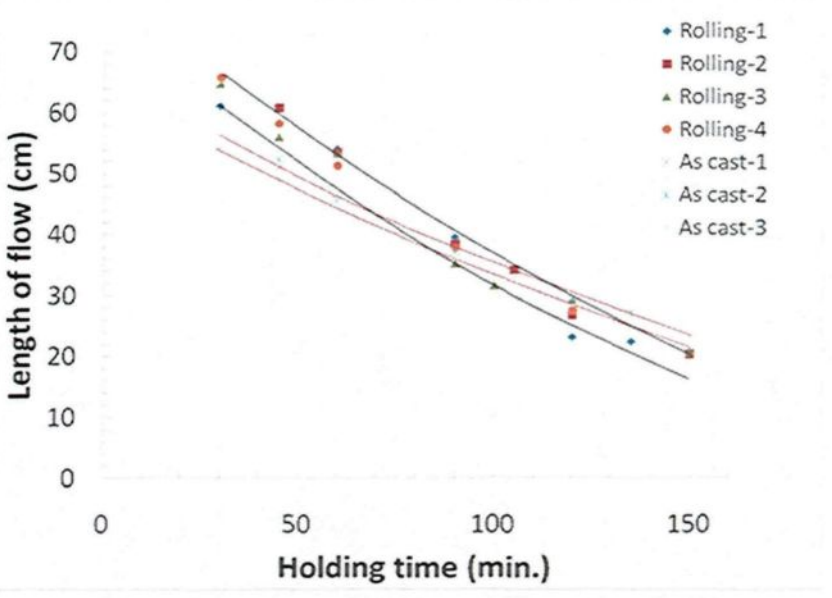

Figure 4.18: Fluidity evolution of cast and rolled Al-16 vol.% B_4C MMCs as a function of holding time.

4.2.2 Original scrap materials

4.2.2.1 Microstructure of B_4C and reaction-induced particles

Figure 4.19 shows the microstructures of the original scrap materials of the cast ingots and rolled sheets. Other than B_4C particles, the reaction-induced particles, mostly Al_3BC and TiB_2, are observed in both materials. In the cast ingots, these reaction-induced particles are mostly attached and close to the B_4C particles. And it is interesting to note that the TiB_2 particles are in the form of coarse plates or needles around the B_4C particles due to the 1.5% Ti addition to the composite melt. On the other hand, many of these particles in the rolled sheets are separated from the B_4C surface due to severe rolled deformation, and it is rare to see the coarse TiB_2 particles attached to B_4C, so that the rolled materials exhibit a more uniform distribution of all solid particles in the matrix.

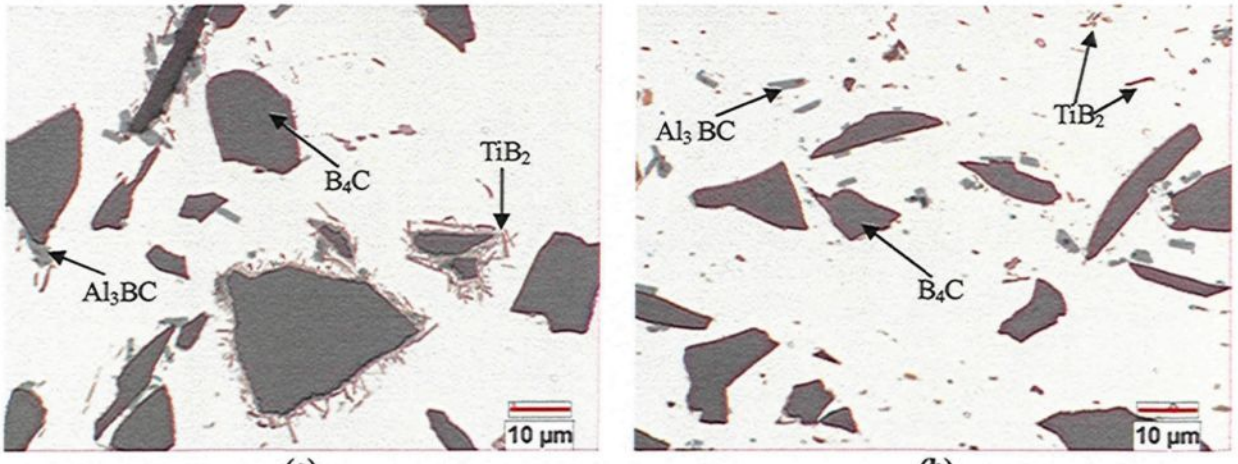

(a) (b)

Figure 4.19: Micrographs of Al-16 vol.% B_4C composite scrap: (a) cast ingots; (b) rolled sheets.

4.2.2.2 Microstructure of particle agglomerates

Figure 4.20 shows that in cast ingots the particle clusters are formed by reaction-induced particles, whereas many particle clusters in the rolled sheets appear to be broken down along the rolling direction, so that they appear much less dense than those observed

in the cast ingots. The amount and size of the clusters in the rolled sheets are less and smaller than those found in the cast ingots.

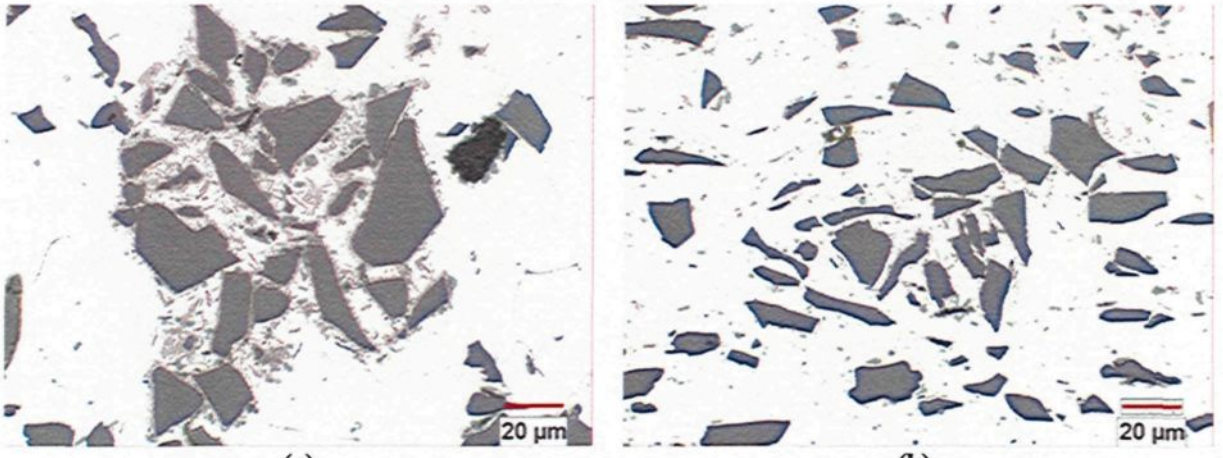

(a) (b)

Figure 4.20: Particle clusters: (a) in cast ingots; (b) in rolled sheets.

Oxide films can also be observed in cast and rolled materials (Figure 4.21). In the cast ingots, B_4C particles and reaction-induced particles are often found to be enclosed by oxide films and could easily form particle networks, increasing flow resistance. On the other hand, in the rolled sheets, the oxide films are squeezed and broken down along the rolling direction. Under heavy deformation of the rolling process, these oxide films become discontinuous tiny slices, which eliminate the tendency to form particle networks during the remelting process.

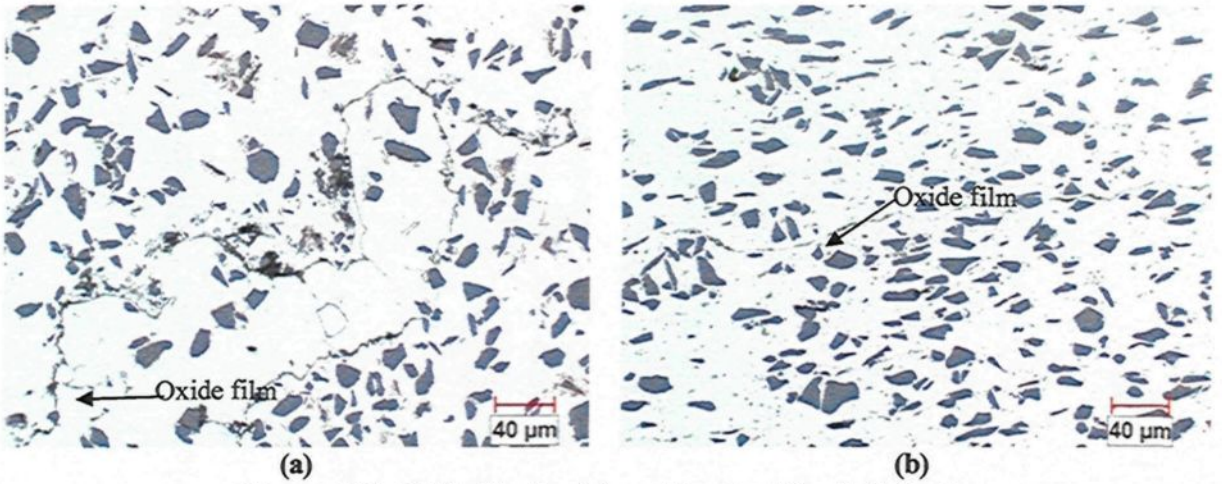

(a) (b)

Figure 4.21: Oxide film in: (a) cast ingots; (b) rolled sheets.

4.2.3 Crucible samples

4.2.3.1 Microstructure of B_4C and reaction-induced particles

The morphological evolution of the crucible samples with 150 minutes holding time is shown in Figure 4.22. In both materials, the amount and size of Al_3BC and AlB_2 become larger than those observed in the original scrap materials. In addition, it is found that, in the cast ingot samples, most of the reaction-induced particles are still attached and close to the B_4C particles after remelting and holding. However, in the rolled sheet samples, some of those particles are separated from the B_4C particles due to the fact that the pre-existing particles are broken down during the rolling process, and these broken particles may provide favored sites for further precipitation and growth of Al_3BC and AlB_2 during remelting and holding. Moreover, after this long holding time, it is interesting to note that a great quantity of freshly formed Al_3BC and AlB_2 are attached to B_4C particles in the rolled sheets (Figure4.22(b)), which may result in a much more inhomogeneous particle distribution in the long term holding.

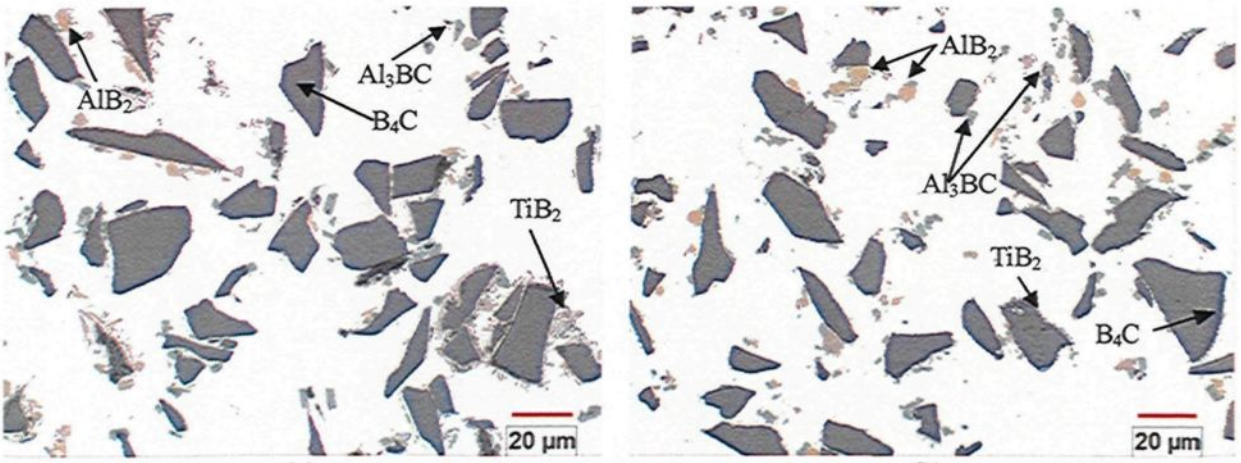

Figure 4.22: Micrographs of the fluidity samples after 150 minutes holding time: (a) cast ingots; (b) rolled sheets.

To further understand the impact of rolling deformation on the microstructure and the microstructural evolution with holding time, original scrap materials of cast ingots and rolled sheets as well as their crucible samples with 60 min holding were examined by SEM as shown in Figures 4.23 and 4.24.

Figure 4.23(a) illustrates that in the original cast ingots, the B_4C particles are enclosed by a very dense TiB_2 layer. Outside this layer, there are many hexagonal shaped TiB_2particles attached to the B_4C particle surface. However, due to hot rolling deformation (97% reduction ratio), this dense TiB_2 layer is severely damaged and peeled away from the B_4C particle surface, and fewer coarse TiB_2 particles are attached to B_4C particles (Figure4.23(b)), which would lead to a more severe interfacial reaction between B_4C and the Al melt, without the TiB_2 barrier layer.

Figure 4.24 gives an example of microstructural evolution of cast ingots and rolled sheets after 60 min holding. It is apparent that the B_4C particle is well enclosed by the TiB_2 layer during remelting, and a few reaction-induced particles, AlB_2 and Al_3BC, are formed attached to the B_4C particles in the cast ingot sample displayed in Figure 4.24(a). On the other hand, in rolling sheets, due to the severe damage of the TiB_2 layer, a large amount of reaction-induced particles are formed and appear attached to the surface of the B_4C particles, Figure 4.24(b), which would deteriorate the uniformity of the particle distribution uniformity. The presence of these particles also indicates a strong tendency to form particle agglomerates in rolled sheet materials during melt holding.

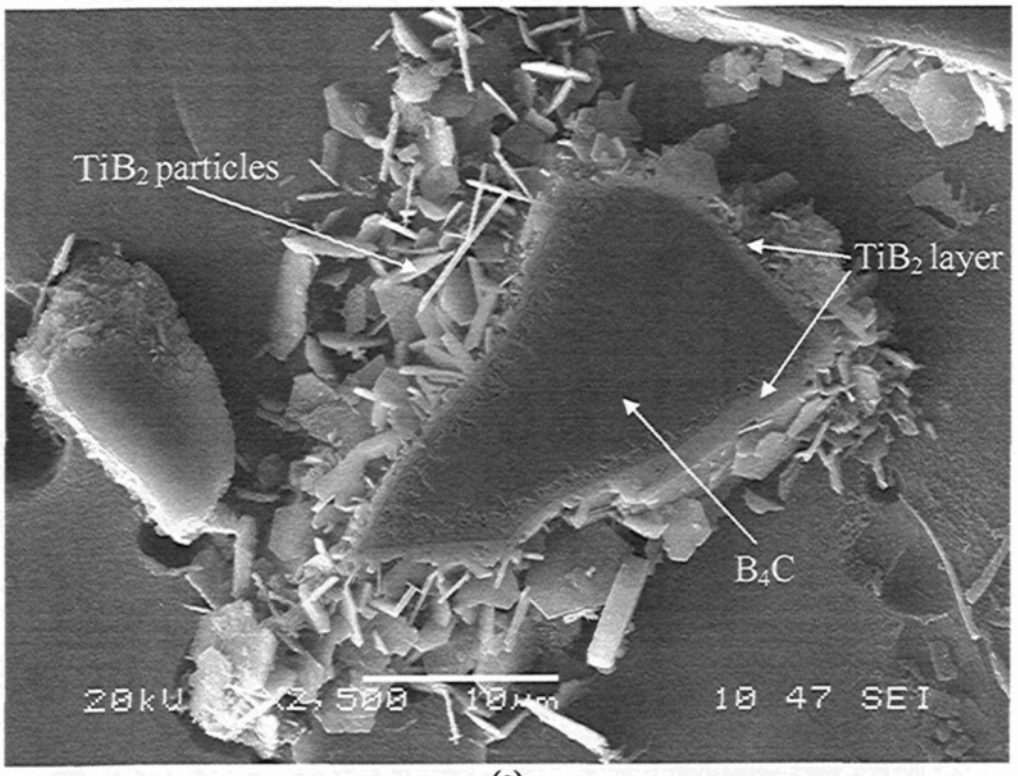

(a)

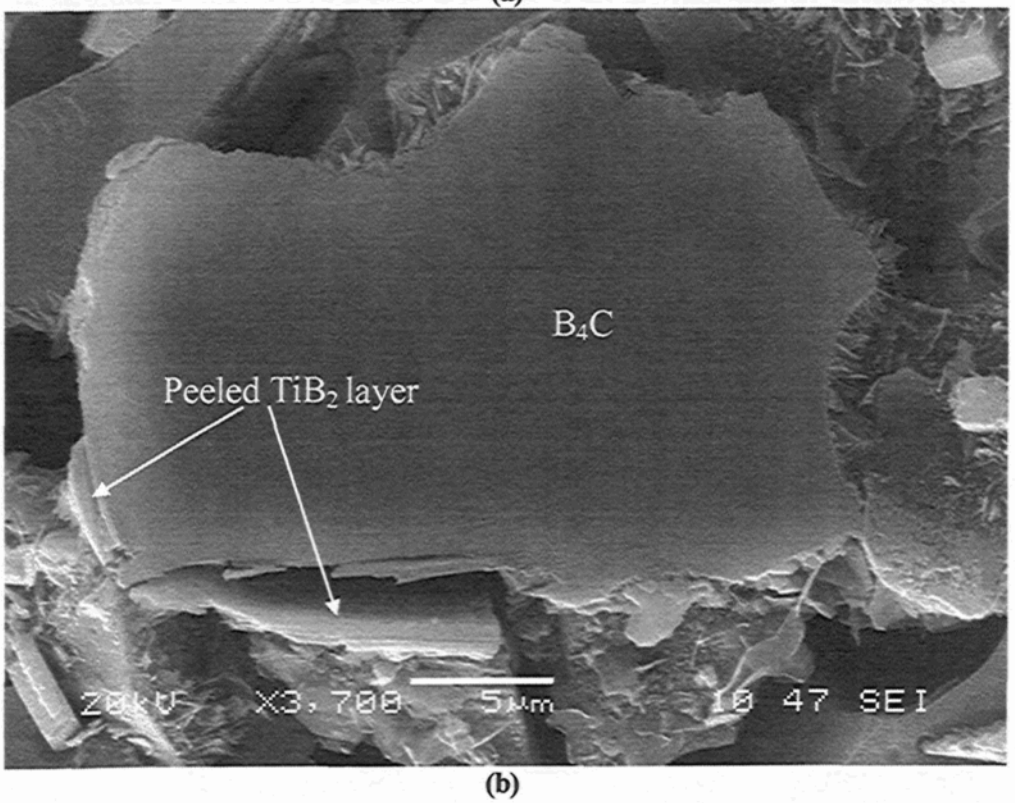

(b)

Figure 4.23: Secondary electron images (SEI) of etched original materials: (a)cast ingots; (b)rolled sheets.

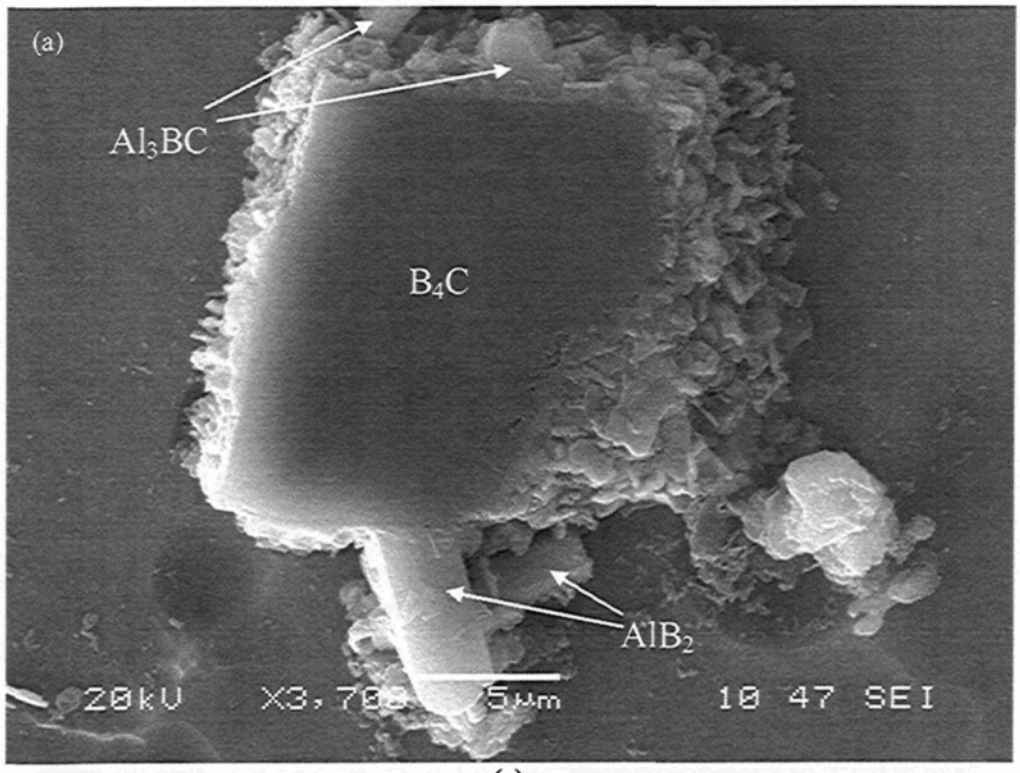

(a)

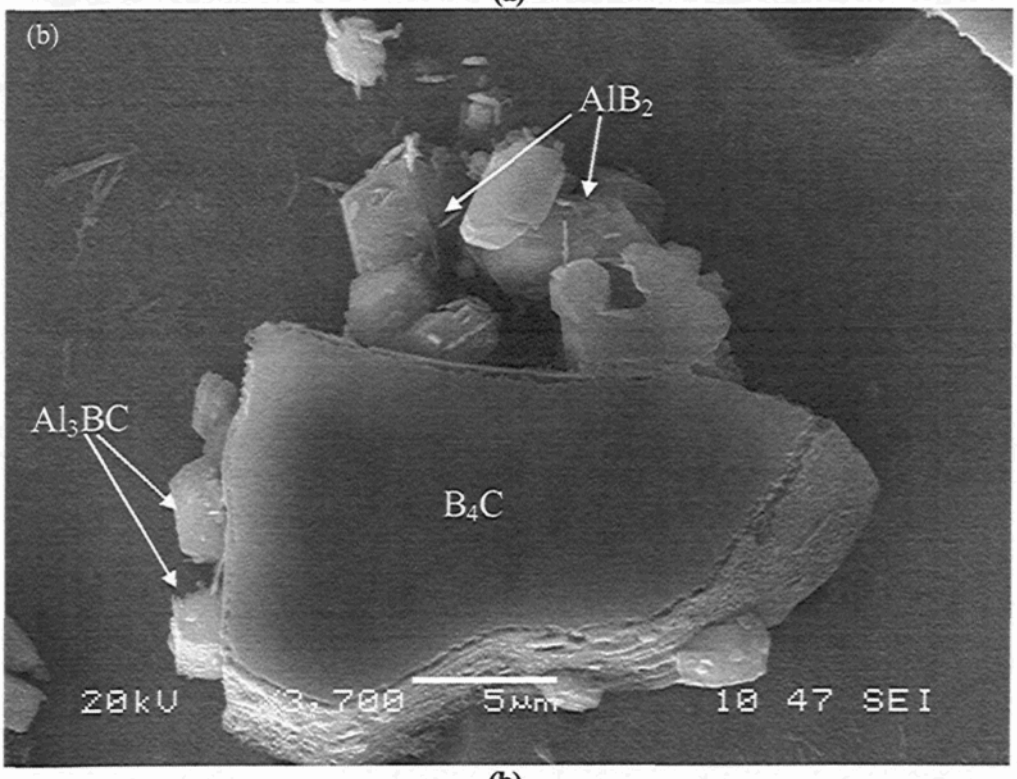

(b)

Figure 4.24: Secondary electron images (SEI) of etched crucible samples obtained after 60 min holding: (a)cast ingots; (b)rolled sheets.

4.2.3.2 Quantitative analysis of B_4C and reaction-induced particles

Particle Volume fraction

Interfacial reactions continued in both cast and rolled materials during the remelting and holding. Table 4.3 shows the volume fraction of B_4C particles and reaction products measured for the crucible samples as a function of holding time.

Table 4.3:Volume fraction of B_4C particles and reaction products with holding time.

Composite	Holding time (min)	Total particles	Volume fraction (%)			
			B_4C	Al_3BC	AlB_2	TiB_2
Cast ingot	30	22.68	15.95	1.69	0.02	1.53
	90	21.96	15.76	1.67	0.17	1.60
	150	23.15	15.48	1.90	0.46	1.62
Rolled sheet	30	22.08	15.67	2.10	0.24	0.95
	90	23.08	15.15	2.47	0.74	1.06
	150	23.98	14.52	2.69	1.17	1.00

From Table 4.3, it is found that as Ti was no longer available in the matrix after remelting, the amount of TiB_2 remained almost constant in the cast and rolled materials during the different holding periods. Furthermore, the volume fraction of TiB_2 in rolled sheets is supposed to be the same as that in cast ingot during the direct rolling process. However, due to critical resolution of optical microscope, partially flaked TiB_2 in the rolled materials is too small to be identified. Therefore, the volume fraction of TiB_2 measured for rolled sheet samples is less than that in the cast ingot samples.

It is also evident that the volume fraction of the total particles increases slowly with the increased in holding time. This increase is contributed to the increasing amount of the reaction-induced particles, namely Al_3BC and AlB_2, since the fraction of B_4C decreased

gradually with holding time. Although there is no large difference in the total particle amounts in both cast and rolled materials during holding, however, shortly after remelting (30 min holding time), the rolled sheet shows a higher volume fraction of Al_3BC and AlB_2 than the cast ingot, With increased holding times (90 and 150 minutes), due to the damage of the TiB_2 barrier layer which increases the probability of interfacial reaction, the rolled sheet possesses a much higher volume fraction of reaction-induced particles than the cast ingot, indicating a strong tendency to form particle segregates, and thereby a rapid increase in the flow resistance.

Particle distribution

Figure 4.25 shows that in both materials, the distribution of Al_3BC and AlB_2 reaction-induced particles becomes more inhomogeneous with remelting and holding time. The distribution of B_4C particles also becomes nonuniform after remelting. It is very interesting to note that at the start of remelting (30 min), the B_4C and reaction-induced particles in the rolled sheet samples show more homogeneous distribution than those in the cast ingot samples. Nevertheless, after a long holding time (150min), the homogeneity of B_4C particle distribution worsens rapidly in rolled sheets. In addition, the distribution homogeneity of reaction-induced particles is worse than the cast ingot samples. The fact that many reaction-induced particles are attached to the B_4C particles, indicate a strong tendency to form particle segregates and thus deteriorate the fluidity. In the cast ingot samples, such particles appear to have a weaker tendency to form particle segregates with long holding times.

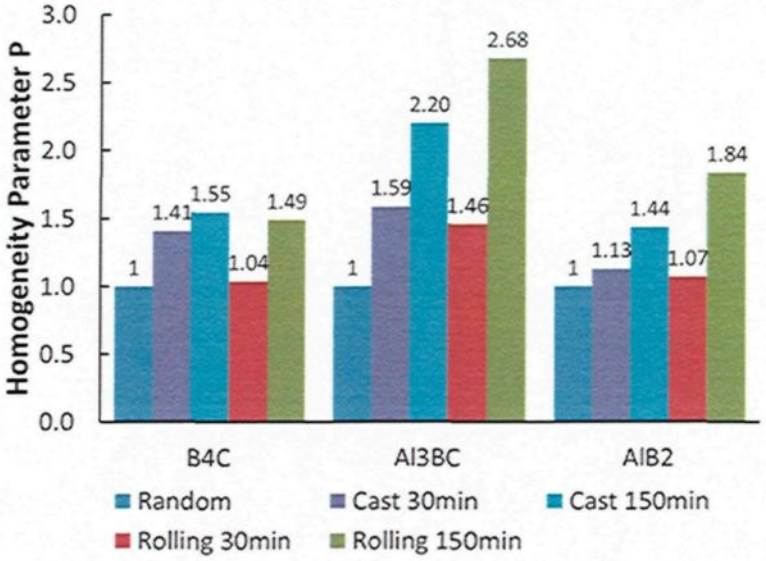

Figure 4.25: Homogeneity evolution of particle distribution in cast and rolled samples with holding time.

4.2.4 Fluidity samples

4.2.4.1 Quantitative analysis of particle agglomerates

Figure 4.26 shows the volume fractions induced by (a) particle clusters and (b) particle networks at the flow end of the fluidity samples, respectively. Results show that these two types of particle agglomerates increase with the increase in holding time. Moreover, the rolled sheet shows a much faster increasing rate of particle clusters, from 5.22% volume fraction difference (30 min) to 0.87% little difference (120 min) compared with that of the cast ingot, which indicates that the rolled materials have a stronger tendency to particle agglomeration than the cast materials during holding, which thus results in a severe deterioration of fluidity during holding periods. Furthermore, the cast ingot indicates a slightly higher fraction of particle networks than the rolled materials.

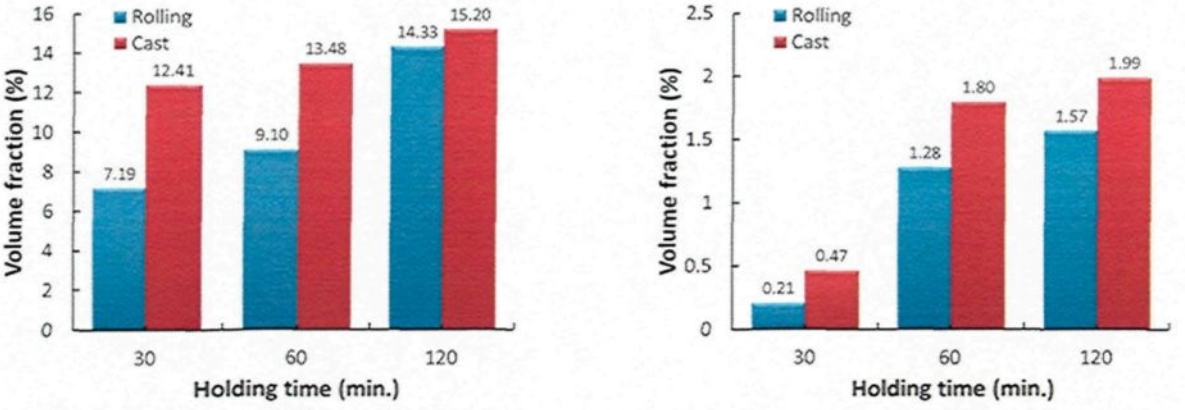

Figure 4.26: (a) Volume fraction of particle clusters; (b) Volume fraction of particle networks induced by oxide films in cast and rolled samples with holding time.

4.2.4.2 Quantitative analysis of B_4C and reaction-induced particles

Particle effective volume fraction along flow

Figure 4.27 shows the effective volume fraction of solid particles along the flow path in both cast and rolled materials for different holding times. As may be observed, the effective volume fraction increases along the flow path. The nearer to the flow end the fluidity sample is, the higher is the effective volume fraction, which suggests that the particle agglomerates are enriched towards the flow end. Shortly after remelting (30 min holding time), the cast ingot sample shows a much higher effective volume fraction towards the flow end than the rolled sheet sample, which gives an indication that a more severe particle segregation and agglomeration exist in the cast materials directly after remelting. With increased holding times (60 min), the cast ingot samples still possess a higher effective volume fraction than the rolled sheet samples along the flow path. However, with prolonged holding time (120min), the two materials show nearly the same increase in effective volume fraction all along the flow path. It is evident that the process of particle segregation and agglomeration accelerate with the increased holding time in

the rolled sheets, leading to a rapid increase of the flow resistance. Moreover, the effective volume fraction of rolled materials increases remarkably with the holding time, especially after 60 min, which corresponded well with a sharp decrease of the fluidity with time. However, the particle agglomerates increase quickly, likely because of the large amount of reaction-induced particles formed and the deterioration in the uniformity of particle distribution. Therefore, the fluidity of the rolled sheet samples decreases sharply due to the rapid increase of flow resistance with holding time.

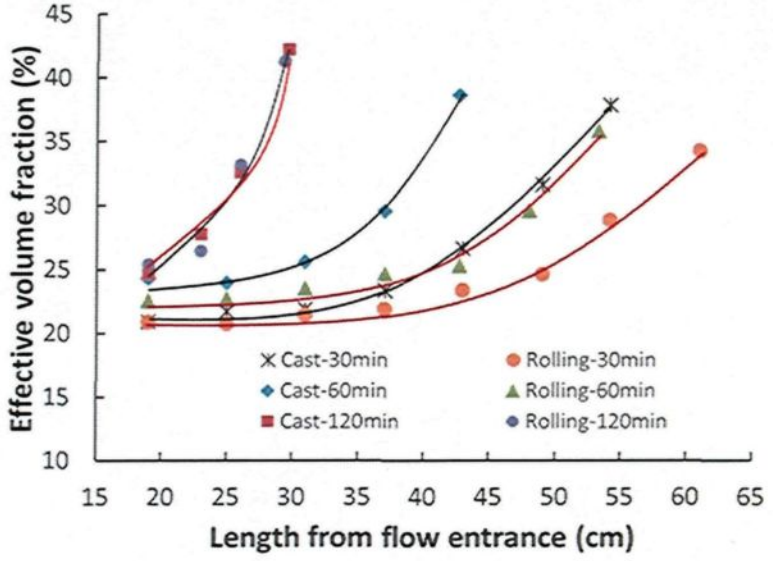

Figure 4.27:Evolution of particle effective volume fraction of the fluidity samples.

Particle effective volume fraction at flow end

As for cast and rolled materials, Figure 4.28(a) indicates the volume fraction of the total solid particles (B_4C, Al_3BC, TiB_2, and AlB_2) at the flow end of fluidity samples as a function of the holding time. In general, the volume fraction of the solid particles increases when prolonging holding time. However, shortly after remelting (30min), the volume fraction of cast ingot is 2.81% higher than that of the rolled sheet. With increase of holding time, the volume fractions of both materials are getting closer and no

remarkable difference after 90 min holding, indicating the relevant tendency to the fluidity evolution.

To further understand the fluidity evolution and consider the effect of particle segregations, the effective volume fraction of both materials is measured in Figure 4.28(b). It is clearly seen that the effective volume fraction increased significantly and shows a linear increase with holding time, which corresponds well with the decreasing trend of fluidity. Further, at beginning of holding (30min), due to the uniformity effect of rolled deformation and lower particle segregation content, the rolled sheet shows a 4.6% lower effective volume fraction than the cast ingot, which results in a better fluidity. When prolonging holding time, the effective volume fraction of rolled sheet increases more rapidly as a result of the severer interfacial reaction and much stronger tendency to form particle segregations. On the other hand, the effective volume fraction of cast ingot increases relatively slowly, which relates well with the slightly decrease of fluidity.

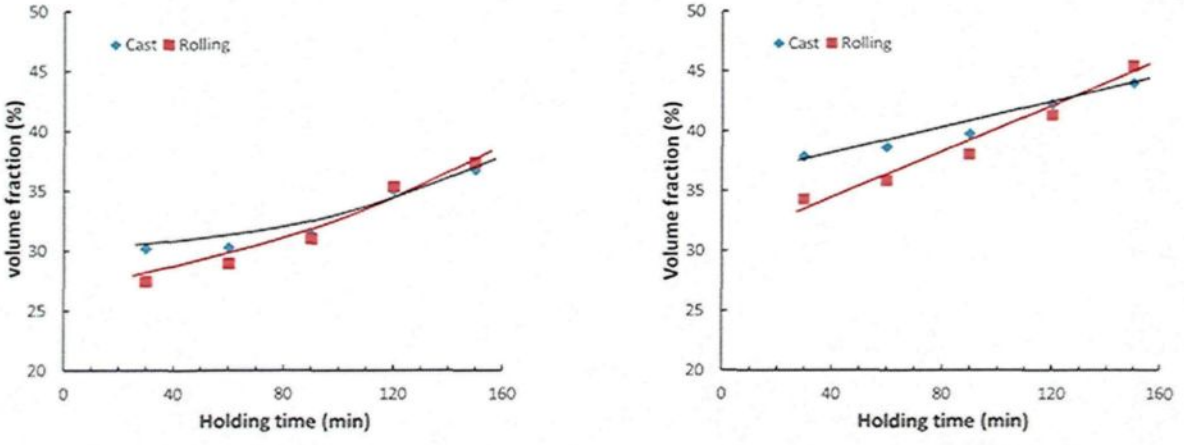

(a) (b)

Figure 4.28: (a) particle volume fraction at the flow end of the fluidity samples; (b) particle effective volume fraction at the flow end of the fluidity samples with holding time.

CHAPTER 5

CONCLUSIONS AND SUGGESTIONS FOR FUTURE WORK

CHAPTER 5

CONCLUSIONS AND SUGGESTIONS FOR FUTURE WORK

5.1 CONCLUSIONS

1. The fluidity of both cast and extruded AA6063-10 vol.%B_4C MMCs decreases with the increase of the holding time. The fluidity decline of the cast billets is much faster than that of the extruded plates during the melt holding period.
2. During remelting and holding, the homogeneity of solid particle distribution in the cast billets is remarkably worse than that of the extruded plates, based on the fact that more reaction-induced particles are attached to or clustered close to the B_4C particles, indicating a strong tendency to form solid particle aggregates.
3. The cast billets exhibit a strong tendency to particle segregation and agglomeration causing a rapid decrease in the fluidity. The extruded plates (extrusion ratio: 22:1) show a more uniform particle distribution and less particle agglomerates and hence maintain a good fluidity.
4. In AA1100-16 vol.% B_4C MMCs, the fluidity of the rolled sheets is slightly higher than that of cast ingots at the start of remelting. With the holding time, the fluidity of both the rolled sheets and cast ingots decreases significantly. As prolonged holding period to 150 min, the fluidity of rolled sheets is more or less the same as the cast ingots.
5. At the beginning of remelting, the rolled sheets show better homogeneity of particle

distribution than the cast ingots because of the uniformity effect of rolling deformation.

6. Due to a severe deformation of hot rolling (97% reduction ratio), the TiB_2 protective layer around B_4C surfaces in rolled sheets is seriously damaged and broken down. With a long term holding, the effective volume fraction of rolled sheets increases more rapidly as a result of severe interfacial reaction and a much stronger tendency for particle agglomerates. Thus, it leads to a quick deterioration of fluidity during holding period.
7. The mechanism of flow arrest is discussed and applied for the explanation of fluidity evolution.
8. The methods for characterization of Al-B_4C composites microstructure are developed based on the image analysis techniques. These methods have been successfully applied to describe and quantitative analyze the particle volume fraction, distribution, agglomeration and particle effective volume fraction.
9. The particle agglomerates in the Al-B_4C MMCs in the form of clusters and networks are commonly encountered in the cast samples. They move as a whole mass during fluid flow and occupy a much greater space than individual solid particles. Therefore, the effective volume fraction of particles is introduced to estimate the influence of particle agglomeration on flow resistance in the Al-B_4C MMCs.

5.2 SUGGESTIONS FOR FUTURE WORK

1. The key to recycling Al-B_4C process scrap is to control the interfacial reaction and avoid the severe formation of particle segregations and agglomerations, which would significantly deteriorate the fluidity. This might be achieved by adding a certain quantity of Ti to reform an interfacial reaction barrier layer during remelting.
2. Characterization of Al-B_4C composites can be further studied to reveal the influence of particle size on the melt flow behavior.

REFERENCES

1. X-G. Chen, Application of Al-B_4C Metal Matrix Compostites in The Nuclear Industry for Neutron Absorber Materials, in: Gupta N, Hunt WH (eds), *Proceedings of solidification processing of metal matrix composites*, TMS 2006, San Antonio, USA, March 2006, pp 343-350.

2. X-G. Chen, Interface Reaction of Boron Carbide in Aluminum Matrix Composites and its Control, *EPD Congress 2005*, edited by M. E. Schlesinger, TMS 2005, pp101-106.

3. Z. Zhang, X-G. Chen and A. Charette, in: N. Gupta, W.H. Hunt (eds), *Proceedings of solidification processing of metal matrix composites*, TMS 2006, San Antonio, USA, March 2006, pp 173.

4. A. R. Kennedy, The Microstructure and Mechanical Properties of Al-Si-B_4C Metal Matrix Composites, *Journal of Materials Science,* Vol 37(No 2), 2002, pp 317-323.

5. M. J. Kozack, S. C. Khatri, J.E. Alison and M.G. Baber, in: S. Suresh et al. (eds.), *Fundamentals of MMCs*, Butterworth-Heinemann, Boston, MA, 1993, pp 297–326.

6. T. S. Srivatsan, I. A. Ibrahim, F.A. Mohamed and E.J. Lavernia, Processing Techniques for Particulate-Reinforced Aluminum Metal Matrix Composites, *Journal of Materials Science*, Vol 26, 1991, pp 5965–5978.

7. D. J. Lloyd (1997) in: P. K. Mallick (eds), *Composites Engineering Handbook*, Marcel Dekker, Inc., pp 631.

8. J. C. Viala, J. Bouix, G. Gonzalez and C. Esinouf, Chemical Reactivity of Aluminium with Boron Carbide, *Journal of Materials Science*, Vol 32, 1997, pp 4559-4573.

9. Z. Zhang, X.-G. Chen and A. Charette, Fluidity and Microstructure of an Al–10% B_4C Composite, *Journal of Materials Science*, Vol 44(No. 2), 2009, pp 492-501.

10. M. K. Surappa and P. K. Rohatgi, Fluidity of Al-Si-Al_2O_3 Composites, *Metallurgical and Materials Transactions B*, Vol 12B, 1981, pp 327-332.

11. F. M. Yarandi, P. K. Rohatgi and S. Ray, Fluidity and Microstructure Formation during Flow of Al- SiC Particle Composites, *Journal of Materials Engineering and Performance*, Vol2(No. 3), 1993, pp 359-364.

12. M. C. Flemings, Fluidity of Metals-Techniques for Producing Ultra-Thin Section Castings, *British Foundryman*, Vol 57, 1964, pp 312-325.

13. J. Campbell, *Castings*, Butterworth Heinemann, 1999, pp 74-75.

14. K. R. Ravi, R. M. Pillai, K. R. Amaranathan, B. C. Pai and M. Chakraborty, Fluidity of Aluminum Alloys and Composites: A Review, *Journal of Alloys and Compounds*, Vol 456, 2008, pp 201–210.

15. P. Rohatgi and R. Asthana, Solidification Science in Cast MMCs: The influence of Merton Flemings, *JOM*, Vol 53 (No.9), 2001, pp 9-13.

16. D. J. Lloyd (1997) In: P. K.Mallick (eds), *Composites Engineering Handbook*, Marcel Dekker, Inc., New York, pp 656-658.

17. B. Hugh, Introduction to Alloy Phase Diagrams, Alloy Phase Diagrams, *ASM Handbook*, The Materials Information Society, Vol 3, 1992, pp 32.

18. D. Aliya, Metallographic Sectioning and Specimen Extraction, Metallography and Microstructures, *ASM Handbook*, ASM International, Vol 9, 2004, pp 229–241.

19. N. Yang, J. Boselli and I. Sinclair, Simulation and Quantitative Assessment of Homogeneous and Inhomogeneous Particle Distributions in Particulate Metal Matrix Composites, *Journal of Microscopy*, Vol 201(No. 2), 2001, pp 189-200.

20. S. Yotte, D. Breysse, J. Riss and S. Ghosh, Microcrack Identification on Particulate

Reinforced Metal Matrix Composite, *Materials Characterization*, Vol. 46, 2001, pp 211-219.

21. P. A. Karnezis, G. Durrant and B. Cantor, Characterization of Reinforcement Distribution in Cast Al-Alloy/SiCp Composites, *Materials Characterization*, Vol. 40, 1998, pp 97-109.

22. R. Asthana, A. Kumar and N. Dahotre, Materials Processing and Manufacturing science, *Elsevier Butterworth-Heinemann*, 2006, pp 406.

23. H. Nayeb-Hashemi and D. Shan, Evaluation of Heat Damage on B_4C Particulate Reinforced Aluminum Alloy Matrix Composite Using Acoustic Emission Techniques, *Materials Science and Engineering A*, 1999, Vol 266 (No.1-2), pp 8-17.

24. R. Asthana, Interfaces in Cast Composites, in *Solidification Processing of Reinforced Metals*, Transtec Publications Ltd: Zurich-Uetikon, 1998, pp 301-350.

25. M. Mabuchi and K. Higashi, Thermal-Stability and Superplastic Characteristics in Si_3N_4 Al-Mg-Si Composites, *Materials Transactions Jim*, 1994, Vol 35(No.6), pp 399-405.

26. X-G. Chen, An advanced Al-B_4C Metal Matrix Composites for Neutron Shielding Materials, Presented at *The 14th International symposium on Packaging and Transportation of Radioactive Materials* (PATRA, 2004), September 2004, Berlin, Germany.

27. Z. Zhang, X-G. Chen, A. Charette, and R. Ghomashchi, Effect of Titanium on Solidification Microstructure of Al-16% B_4C Composites, *Light Metals 2005*, ed. J. P. Martin, 44th Annual Conference of Metallurgist of the CIM, 2005, pp 477-456.

28. A. Kolsgaard and S. Brusethaug, Fluidity of Aluminium Alloy $AlSi_7Mg$-SiC Particulate Composite Melts, *Materials Science and Technology*, Vol 10, 1994, pp 545-551.

29. Z. Zhang, X.-G. Chen and A. Charette, Particle Distribution and Interfacial Reactions

of Al–7%Si–10%B_4C Die Casting Composite, *Journal of Materials Science*, Vol 42(No. 17), 2007, pp 7354-7362.

30. J. C. Viala, in: R. Drew, M. D. Pugh, M.Brochu (eds), *Proceedings of The International Symposium on Metal/Ceramic Interactions*, Montreal, Canada, August 2002, pp 63.

31. D. C. Halverson, A. J. Pyzik, L.A. Aksay and W. E. Snowdenet, Processing of Boron Carbide-Aluminum Composites, *Journal of the American Ceramic Society*, Vol 72(No.5), 1989, pp 775-780.

32. K. M. Shorowordi, T. Laoui and A. S. M. A. Haseeb, Microstructure and Interface Characteristics of B_4C, SiC and Al_2O_3 Reinforced Al Matrix Composites, *Journal of Materials Processing Technology*, Vol 142(No.3), 2003, pp 738-743.

33. D. E. Alman, Properties of Metal-Matrix Composites, in *ASM Handbook: Composites*, ASM International, Materials Park, 2001.

34. C. B. Lin, C. L. Ma, Y. W. Chung, Microstructure of A380-SiC(p), Composites for Die Casting, *Journal of Materials Processing Technology,* Vol 84 (No.1-3), 1998, pp 236-246.

35. C. B. Lin, C. L. Wu, C. H. Chiang, Analysis of Mold Flow and Microstructures of Die Casting in Al Alloy/Sic(P) Composites, *Journal of Materials Science,* Vol 34(No 9), 1999, pp 2229-2240.

36. F. Bedir, Characteristic Properties of Al-Cu-SiCp and Al-Cu-B_4Cp Composites Produced by Hot Pressing Method Under Nitrogen Atmosphere, *Materials and Design*, Vol 28 (No. 4), 2007, pp 1238-1244.

37. J. C. Viala, G. Gonzales and J. Bouix, Composition and Lattice Parameters of a New Aluminium-Rich Boron Carbide, *Journal of Materials Science Letters*, Vol 11(No.10) , 1992, pp 711-714.

38. G. Arslan, F. Kara and S. Turan, Quantitative X-Ray Diffraction Analysis of Reactive

Infiltrated Boron Carbide-Aluminium Composites, *Journal of the European Ceramic Society*, Vol 23 (No.8), 2003, pp 1243-1255.

39. M. Kouzeli, C. San Marchi and A. Mortensen, Effect of Reaction on the Tensile Behavior of Infiltrated Boron Carbide-Aluminum Composites, *Materials Science and Engineering A* , Vol337(No.1-2) , 2002, pp 264-273.

40. W. B. Johnson, A. S. Nagelberg and E. Breval, Kinetics of Formation of a Platelet-Reinforced Ceramic Composite Prepared by the Directed Reaction of Zirconium with Boron Carbide. *Journal of the American Ceramic Society*, Vol 74(No.9), 1991, pp 2093-2101.

41. P. Rogl, H. Bittermann and H. Duschanek, Boron – Carbon – Titanium, in Ternary Alloy Systems Phase Diagrams, *Crystallographic and Thermodynamic Data*, G. Effenberg & S. Ilyenko (Eds). Springer-Verlag, Berlin, Heidelberg, 2006.

42. M. C. Flemings, *Solidification Processing*, McGraw-Hill Book Company, New York, 1974.

43. M. D. Sabatino, *Fluidity of Aluminium Alloys*, PhD Thesis at Norwegian University of Science and Technology, Trondheim, 2005.

44. P. G. Thomas: *Journal of Colloid and Interface Science*, 1965, Vol 34, pp 591.

45. K. R. Ravi, R. M. Pillai, B. C. Pai, and M. Chakraborty, Influence of Interfacial Reaction on the Fluidity of A356 Al-SiCp Composites—A Theoretical Approach, *Metallurgical and Materials Transactions A*, Vol 38 (No.10), 2007, pp 2531-2539.

46. V. A. Ravi, D. J. Frydrychand, A. S. Nagelberg, in: D. M. Stefanescu, S. Sen (Eds.), *Cast MMC*, American Foundrymen's Society, Des Plaines, 1994, pp 306.

47. D.O. Kennedy, 95th Annual Meeting of American Foundrymen's Society, *AFS*, Birmingham, 1991, pp 729.

48. R. E. Carity, *AFS Transmission*, Vol 152, 1990, pp 743.

49. V. A. Ravi, D. J. Frydrych and A. S. Nagelberg, Effect of Particle size, Shape and Loading on Fluidity of SiC-Reinforced Aluminum MMCs, *AFS transactions*, Vol 102, 1994, pp 891-895.

50. Surappa M. K., P. K. Rohatgi, Preparation and Properties of Cast Aluminium-Ceramic Particle Composites, *journal of materials science*, Vol 16, 1981, pp 983-993.

51. F. M. Yarandi, P. K. Rohatgi and S. Ray, Fluidity and Microstructure Formation during Flow of Al- SiC Particle Composites, *Journal of Materials Engineering and Performance,* Vol 2 (No 3), 1993, pp 359-364.

52. J. C. Russ, *The Image Processing Handbook*, 5th Edition, CRC Press, London, 2002, pp 511-513.

53. D. Aliya, Metallographic Sectioning and Specimen Extraction, Metallography and Microstructures, *ASM Handbook*, ASM International, Vol 9, 2004, pp 229–241.

54. A. Wachter and D. Windberg, *Acta Stereol.*, Vol 5, 1986, pp 29-36.

55. I. C. Stone and P. Tsakiropoulos, Characterization of Spatial Distribution of Reinforcement in Powder Metallurgy Route Al/SiCp Metal Matrix Composites 2: Techniques Based on Local Energy Dispersive X-ray Analysis, *Materials Science and Technology*, Vol 11, 1995, pp 222-227.

56. D. Van Hille, S. Bengtsson, and R. Warren, Quantitative Metallographic Study of Fiber Morphology in a Short Fiber Al2O3 Fiber Reinforced Al Alloy Matrix, *Composites Science and Technology*, Vol 35, 1989, pp 195-206.

57. H. Schwarz and H. E. Exner, , The Characterisation of The Arrangement of Feature Centroids in Planes and Volumes, *Journal of Microscopy*, Vol 129, 1983, pp 155-169.

58. W. A. Spitzig, J. F. Kelly, and O. Richmond, Quantitative Characterisation of Second-Phase Populations, *Metallography*, Vol 18, 1985, pp 235-261.

59. M. T. Shehata, and J. D. Boyd, Measurement of Spatial Distribution of Inclusions

and Their Influence on Material Behaviour, R. Rungla (eds), *ASM International*, Ohio, 1988, pp 123-131.

60. J. B. Parse and J. A. Wert, A Geometrical Description of Particle Distributions in Materials, Modeling and Simulation in Materials Science and Engineering, Vol 1, 1993, pp 275-296.

61. J.C. Russ, Adjacency Measurements in Tessellations, *Journal of Computer-Assisted Microscopy*, Vol 1, 1989, pp 217-247.

62. M. Bertram and H. Wendrock, Characterisation of Planar Local Arrangement by means of the Delaunay Neighbourhood, *Journal of Microscopy*, Vol 181, 1996, pp 45-53.

63. J. Boselli, P. D. Pitcher, P. J. Gregson and I. Sinclair, Secondary Phase Distribution Analysis via Finite Body Tessellation, *Journal of Microscopy*, Vol 195, 1999, pp 104-112.

64. G. Burger, E. Koken, D. S. Wilkinson and J. D. Embury, The Influence of Spatial Distributions on Metallurgical Processes, *Advances in Phase Transitions*, J. D. Embury and G. R. Purdy (eds), Pergamon Press, Oxford, 1988, pp 247–266.

65. D. J. Lloyd, in: *Metal matrix composites: processing, microstructure and properties*, Symposium on Materials Science, N. Hansen et al. (eds), Riso National Laboratory, 1991, pp 81-99.

66. I. C. Stone and P. Tsakiropoulos, Characterization of Spatial Distribution of Reinforcement in Powder Metallurgy Route Al/SiCp Metal Matrix Composites 1: Techniques Based on Microstructure, *Materials Science and Technology*, Vol 11, 1995, pp 213-221.

67. R. Pyrz, Quantitative Description of The Microstructure of Composites. Part I: Morphology of Unidirectional Composite Systems, *Compost Science and Technology*, Vol 50 (No 2), 1994, pp 197-208.

68. A. M.Murphy, S. J. Howard and T. W. Clyne, Characterisation of Severity of Particle Clustering and its Effect on Fracture of Particulate MMCs, *Materials Science and Technology*, Vol 14, 1998, pp 959-968.

69. A. Getis and B. Boots, in :*Models of spatial processes, 1st Edn,* Cambridge University Press, Cambridge, 1978.

70. F. George and V. Vander, in: *Evaluating clustering of second-phase particles,* George F. Vander Voort (eds), American Society for Tesing and Materials, Philadelphia, 1990, pp 242-264.

71. M. Li, S. Ghosh, T. N. Rouns, H. Weiland, O. Richmond and W. Hunt, Serial Sectioning Method in the Construction of 3-D Microstructures for Particle-Reinforced MMCs , *Materials Characterization*, Vol 41, 1998, pp 81-95.

72. N. Silva and A. Velhinho, Assessment of particle clustering in MMCs by quantitative image analysis, *Materials Science Forum*, Vol 514-516, 2006, pp 779-783.

73. G. Langelaan, D. Steele and M. Bull, Complementary Techniques: Characterization of The Clustering of Inter-Metallic Particle, *ICAA*, 2008.

74. S. K. Park and K. W. Miller, Random Number Generators: Good Ones Are Hard To Find, Communications of the ACM, Vol 31(No 10), 1988, pp 1192-1201.

75. S. G. Ward, Studies of the viscosity and sedimentation of suspensions Part 2. - The viscosity and sedimentation of suspensions of rough powders, *Journal of Applied Physics*, Vol 1, 1950, pp 325-328.

APPENDICES

APPENDICES

Appendix A: Sample grinding and polishing steps for Al-B_4C MMCs

I. Grinding:

Step	PG 1	FG 2	FG 3
Surface	Diamond disk	Diamond disk	Diamond disk
Abrasive	Diamond	Diamond	Diamond
Grit/Grain size [μm]	74	40	40
Lubricant	Water	Water	Metadi
Speed [rpm]	120 ↓↑	120 ↓↑	120 ↓↑
Force [N]	60	120	60
Time [min]	Until Plane	5	10

II. Polishing:

Step	DP 1	DP 2	DP 3	DP 4	OP
Surface	Silk/Texmet	Texmet	Texmet	Texmet	MD-Chem
Abrasive	Diamond	Diamond	Diamond	Diamond	Colloidal silica
Grit/Grain size[μm]	15	6	3	1	0.05
Lubricant	Blue	Blue	Blue	Red+Blue	Water
Speed[rpm]	150 ↑↑	150 ↑↑	150↑↑	150 ↑↑	150 ↑↑
Force[N]	180	180	160	160	60
Time[min]	5/10, until no broken particles	3	8	10-20	0.5

Note:

PG: Plane Grinding

FG: Fine Grinding

DP: Diamond Polishing

OP: Oxide Polishing

↑↑: Same rotation direction (specimen holder and polishing cloth)

↓↑: Opposite rotation direction

Appendix B: Routine for measurement of particle volume fraction in Al-B_4C MMCs

```
001 ' Volume fraction analysis
002
003 Grab
004 Clear => All
005
006 ' Threshold B4C
007 Color Threshold -> BPL1
    Hue: start = 0°, delta = 360°
    Saturation: 0%..99%
    Intensity: 50..110
008 Object Transfer BPL1 -> None
    Area less than 6µm²
009 Chord Size BPL1 -> None Diameter = 5
010 Closing CIRC x1 => BPL1 Extend
011
012 ' Threshold AlB2
013 Color Threshold -> BPL2
    Hue: start = 1°, delta = 59°
    Saturation: 0%..100%
    Intensity: 121..200
014 Chord Size BPL2 -> None Diameter = 4
015 Closing CIRC x1 => BPL2 Extend
016 Color Threshold -> BPL8
    Hue: start = 300°, delta = 135°
    Saturation: 0%..100%
    Intensity: 105..150
017 Chord Size BPL8 -> None Diameter = 4
018 Closing CIRC x1 => BPL8 Extend
019 (BPL1 DIFF BPL8) -> BPL1
020 (BPL2 OR BPL8) -> BPL2
021
022 Copy BPL1 -> BPL12
023 Dilate CIRC x1 => BPL12
024
025 ' Threshold TiB2
026 Color Threshold -> BPL4
    Hue: start = 250°, delta = 109°
    Saturation: 0%..100%
    Intensity: 120..200
027 (BPL4 DIFF BPL12) -> BPL4
028 Chord Size BPL4 -> None Diameter = 2
029 Closing CIRC x1 => BPL4 Extend
030 (BPL4 DIFF BPL2) -> BPL4
031
032 ' Threshold Al3BC
033 Color Threshold -> BPL3
    Hue: start = 61°, delta = 189°
    Saturation: 0%..100%
    Intensity: 110..200
034 Chord Size BPL3 -> None Diameter = 2
035 Closing CIRC x1 => BPL3 Extend
```

```
036 (BPL3 DIFF BPL2) -> BPL3
037 (BPL4 DIFF BPL3) -> BPL4
038
039 ' Threshold Porosity
040 Color Threshold -> BPL6
   Hue: start = 70°, delta = 360°
   Saturation: 0%..100%
   Intensity: 0..60
041 (BPL6 DIFF BPL1) -> BPL6
042
043 ' Threshold total particles
044 Color Threshold -> BPL7
   Hue: start = 70°, delta = 360°
   Saturation: 0%..100%
   Intensity: 50..200
045 (BPL7 OR BPL1) -> BPL7
046 Chord Size BPL7 -> None Diameter = 3
047
048 Field Measures (BPL1)  -> FLDM1
   Area
   Area Percent
049 Field Measures (BPL2)  -> FLDM2
   Area
   Area Percent
050 Field Measures (BPL3)  -> FLDM3
   Area
   Area Percent
051 Field Measures (BPL4)  -> FLDM4
   Area
   Area Percent
052 Field Measures (BPL6)  -> FLDM6
   Area
   Area Percent
053 Field Measures (BPL7)  -> FLDM7
   Area
   Area Percent
054 Relative Measures -> RELM8
   Area Percent
   BPL1
   BPL2
   BPL3
   BPL4
   BPL5
   BPL6
   BPL7
   Relative to Field
055 Clear => All
056 Live
```

Appendix C: Routine for characterization of particle distribution homogeneity in Al-B_4C MMCs

```
001 ' Particle distribution analysis
002
003 Load Image 'image'
    File: image.tif
    Path: C:\Documents and Settings\DuyguKocaefe\Desktop
004 Clear => All
005 ' Threshold B4C
006 Color Threshold -> BPL1
    Hue: start = 0°, delta = 360°
    Saturation: 0%..99%
    Intensity: 50..110
007 Object Transfer BPL1 -> None
    Area less than 3µm²
008 Chord Size BPL1 -> None Diameter = 5
009 Closing CIRC x1 => BPL1 Extend
010
011 ' Threshold AlB2
012 Color Threshold -> BPL2
    Hue: start = 1°, delta = 59°
    Saturation: 0%..100%
    Intensity: 121..200
013 Chord Size BPL2 -> None Diameter = 4
014 Closing CIRC x1 => BPL2 Extend
015 Color Threshold -> BPL8
    Hue: start = 300°, delta = 135°
    Saturation: 0%..100%
    Intensity: 105..150
016 Chord Size BPL8 -> None Diameter = 4
017 Closing CIRC x1 => BPL8 Extend
018 (BPL1 DIFF BPL8) -> BPL1
019 (BPL2 OR BPL8) -> BPL2
020 Fill => BPL2
021
022 Copy BPL1 -> BPL12
023 Dilate CIRC x1 => BPL12
024
025 ' Threshold TiB2
026 Color Threshold -> BPL4
    Hue: start = 250°, delta = 109°
    Saturation: 0%..100%
    Intensity: 120..200
027 (BPL4 DIFF BPL12) -> BPL4
028 Chord Size BPL4 -> None Diameter = 2
029 Closing CIRC x1 => BPL4 Extend
030 (BPL4 DIFF BPL2) -> BPL4
031
032 ' Threshold Al3BC
033 Color Threshold -> BPL3
    Hue: start = 61°, delta = 189°
    Saturation: 0%..100%
```

```
   Intensity: 110..200
034 Chord Size BPL3 -> None Diameter = 3
035 Closing CIRC x1 => BPL3 Extend
036 (BPL3 DIFF BPL2) -> BPL3
037 (BPL4 DIFF BPL3) -> BPL4
038 Fill => BPL3
039 Chord Size BPL3 -> None Diameter = 3
040
041 Hide => All
042 Pause Edit Kill BPL3
043
044 ' Tesselation B4C
045 Invert BPL1 -> BPL1
046 Trap BPL1 -> None 30x30
047 Invert BPL1 -> BPL1
048 Copy BPL1 -> BPL9
049 Erode OCT x2 => BPL9 Extend
050 Zone CIRC  to End => BPL9
051 Invert BPL9 -> BPL10
052 Clear => BPL10
053 (BPL1 AND BPL9) -> BPL1
054 Centroid => BPL1
055 Copy BPL1 -> BPL10
056 Zone CIRC  to End => BPL1
057 Square Grid 1x1 -> BPL9
   Overall Grid Dimensions
   760 x 572 pixels
   198 x 149 µm
058 Transfer (BPL1 SEL BPL9) -> None
059 Hide => All
060
061 ' Tesselation A1B2
062 Invert BPL2 -> BPL2
063 Trap BPL2 -> None 15x15
064 Invert BPL2 -> BPL2
065 Copy BPL2 -> BPL9
066 Erode CIRC x1 => BPL9 Extend
067 Zone CIRC  to End => BPL9
068 Invert BPL9 -> BPL11
069 Clear => BPL11
070 (BPL2 AND BPL9) -> BPL2
071 Centroid => BPL2
072 Copy BPL2 -> BPL11
073 Zone CIRC  to End => BPL2
074 Square Grid 1x1 -> BPL9
   Overall Grid Dimensions
   760 x 572 pixels
   198 x 149 µm
075 Transfer (BPL2 SEL BPL9) -> None
076 Hide => All
077
078 ' Tesselation A13BC
079 Invert BPL3 -> BPL3
```

080 Trap BPL3 -> None 15x15
081 Invert BPL3 -> BPL3
082 Copy BPL3 -> BPL9
083 Zone CIRC to End => BPL9
084 Invert BPL9 -> BPL12
085 Clear => BPL12
086 (BPL3 AND BPL9) -> BPL3
087 Centroid => BPL3
088 Copy BPL3 -> BPL12
089 Zone CIRC to End => BPL3
090 Square Grid 1x1 -> BPL9
  Overall Grid Dimensions
  760 x 572 pixels
  198 x 149 μm
091 Transfer (BPL3 SEL BPL9) -> None
092 Hide => All
093
094 Object Measures (BPL1) -> OBJM1
  Area
095 Object Measures (BPL2) -> OBJM3
  Area
096 Object Measures (BPL3) -> OBJM4
  Area
097 Object Measures (BPL10) -> OBJM2
  X Centroid
Y Centroid
098 Object Measures (BPL11) -> OBJM5
  X Centroid
  Y Centroid
099 Object Measures (BPL12) -> OBJM6
  X Centroid
  Y Centroid
100 Clear => All
101 Live

Appendix D: Routine for identification of particle cluster in Al-B_4C MMCs

```
001 ' Particle cluster analysis
002
003 Grab
004 Load Image '#' with Bitplanes
   File: #.tif
   Path: E:\Experiment\Mosaic Image\Tip cluster&oxide film analysis\EXT12-300min TIP\ABC
005 Clear => All
006
007 ' Threshold B4C
008 Color Threshold -> BPL4
   Hue: start = 70°, delta = 360°
   Saturation: 0%..100%
   Intensity: 0..40
009 Object Transfer BPL4 -> BPL4
   Area greater than 600µm²
010 Dilate CIRC x4 => BPL4
011 Color Threshold -> BPL1
   Hue: start = 0°, delta = 360°
   Saturation: 0%..99%
   Intensity: 50..110
012 Object Transfer BPL1 -> None
   Area less than 6µm²
013 Chord Size BPL1 -> None Diameter = 3
014 Copy BPL1 -> BPL5
015 Copy BPL1 -> BPL11
016 Hide => BPL4
017
018 ' Identify AlB2, Al3BC
019 Color Threshold -> BPL6
   Hue: start = 1°, delta = 59°
   Saturation: 0%..100%
   Intensity: 121..200
020 Chord Size BPL6 -> None Diameter = 2
021 Closing CIRC x1 => BPL6 Extend
022 Color Threshold -> BPL8
   Hue: start = 300°, delta = 135°
   Saturation: 0%..100%
   Intensity: 105..150
023 Chord Size BPL8 -> None Diameter = 2
024 Closing CIRC x1 => BPL8 Extend
025 (BPL1 DIFF BPL8) -> BPL1
026 (BPL6 OR BPL8) -> BPL6
027 Color Threshold -> BPL8
   Hue: start = 61°, delta = 189°
   Saturation: 0%..100%
   Intensity: 110..200
028 Chord Size BPL8 -> None Diameter = 2
029 Closing CIRC x1 => BPL8 Extend
030 (BPL8 DIFF BPL6) -> BPL8
031 (BPL1 DIFF BPL8) -> BPL1
032 (BPL6 OR BPL8) -> BPL8
```

```
033 Transfer (BPL8 SEL BPL4) -> None
034
035 Dilate CIRC x1 => BPL8
036
037 ' Identify clustering
038 Color Threshold -> BPL3
   Hue: start = 70°, delta = 360°
   Saturation: 0%..100%
   Intensity: 50..200
039 Chord Size BPL3 -> None Diameter = 3
040 Copy BPL3 -> BPL9
041 Copy BPL3 -> BPL7
042 Transfer (BPL3 SEL BPL8) -> BPL3
043 ' recover clusters with larger porosity
044 Transfer (BPL3 SEL BPL4) -> BPL12
045 Copy BPL12 -> BPL10
046 Closing CIRC x1 => BPL10 Extend
047 (BPL10 OR BPL4) -> BPL10
048 Object Transfer BPL10 -> BPL10
   Child Area Percent.BPL4 less than 10%
049 Transfer (BPL12 SEL BPL10) -> BPL12
050 (BPL12 OR BPL3) -> BPL3
051
052 Copy BPL3 -> BPL2
053 Dilate CIRC x1 => BPL2
054 Fill => BPL2
055 Erode CIRC x6 => BPL2 Extend
056 Object Transfer BPL2 -> None
   Area less than 300µm²
057
058 Dilate CIRC x5 => BPL2
059
060 ' Edit particles' clustering
061 Transfer (BPL3 SEL BPL2) -> BPL3
062 Closing CIRC x5 => BPL3 Extend
063 Fill => BPL3
064 Erode CIRC x1 => BPL1 Extend
065 Object Transfer BPL3 -> BPL3
   Child Count.BPL1 greater than 3n
066
067 Copy BPL3 -> BPL11
068 Convex Hull CIRC  x20 => BPL3
069 Invert BPL11 -> BPL11
070 Opening CIRC x20 => BPL11 Extend
071 (BPL3 DIFF BPL11) -> BPL3
072 Convex Hull CIRC  x10 => BPL3
073 Fill => BPL3
074
075 (BPL7 AND BPL3) -> BPL7
076
077
078 Object Measures (BPL3) -> OBJM1
   Area
```

Perimeter
Length
Feret Average
Sphericity
Aspect Ratio
079 Object Measures (BPL7) -> OBJM2
Area
Perimeter
Length
Feret Average
Sphericity
Aspect Ratio
080 Clear => All
081 Live

Appendix E: Routine for identification of particle network in Al-B_4C MMCs

```
001 ' Particle network induced by oxide film analysis
002
003 Grab
004 Load Image '#' with Bitplanes
   S2-90min tip\123456987
   Path: C:\Documents and Settings\DuyguKocaefe\My Documents\Cangji\Mosaic Image\Cluster &
Oxide flim analysis\RCAS2-90min tip\123456987

005 Clear => All
006
007 Pause Edit Lasso BPL12
   Lasso oxide film
008 Color Threshold -> BPL3
   Hue: start = 70°, delta = 360°
   Saturation: 0%..100%
   Intensity: 50..200
009 Chord Size BPL3 -> None Diameter = 3
010 (BPL3 AND BPL12) -> BPL3
011
012 Object Measures (BPL3, 12) -> OBJM1
   Area
   Perimeter
   Length
Feret Average
Sphericity
   Aspect Ratio
013
014 Clear => All
015 Live
```

Appendix F: Routine for measurement of particle effective volume fraction in Al-B_4C MMCs

```
001 ' Total particle effective  volume fraction analysis-Cangji
002
003 Grab
004 Load Image 'ECAS2-120min distribution 5-6' with Bitplanes
   File: ECAS2-120min distribution 5-6.tif
   Path: E:\Experiment\Mosaic Image\distribution analysis\ECAS2-120min distribution
005 Clear => All
006
007 ' 1.Equivalent total particle area, perimeter  measurement
008
009 ' Threshold Porocity
010 Color Threshold -> BPL4
   Hue: start = 70°, delta = 360°
   Saturation: 0%..100%
   Intensity: 0..40
011 Object Transfer BPL4 -> BPL4
   Area greater than 100μm²
012 Dilate CIRC x3 => BPL4
013
014 Color Threshold -> BPL3
   Hue: start = 70°, delta = 360°
   Saturation: 0%..100%
   Intensity: 0..60
015 Object Transfer BPL3 -> None
   Area less than 6000μm²
016 Fill => BPL3
017
018 ' Threshold B4C
019 Color Threshold -> BPL1
   Hue: start = 0°, delta = 360°
   Saturation: 0%..99%
   Intensity: 50..110
020 Object Transfer BPL1 -> None
   Area less than 6μm²
021 Chord Size BPL1 -> None Diameter = 5
022 Closing CIRC x1 => BPL1 Extend
023 Transfer (BPL1 SEL BPL3) -> None
024 Copy BPL1 -> BPL6
025 Erode CIRC x5 => BPL6 Extend
026
027 ' Develop Complex  Model
028 Color Threshold -> BPL2
   Hue: start = 70°, delta = 360°
   Saturation: 0%..100%
   Intensity: 50..200
029 Chord Size BPL2 -> None Diameter = 3
030 Transfer (BPL2 SEL BPL3) -> None
031 Transfer (BPL2 SEL BPL4) -> BPL8
032 Clear => BPL3, BPL4
033 Closing CIRC x2 => BPL2 Extend
```

```
034 Fill => BPL2
035 Thin CIRC  x1 => BPL2
036 Disconnect HEX => BPL2
037 Object Transfer BPL2 -> BPL3
   Area less than 100µm²
038 Object Transfer BPL3 -> None
   Area less than 2µm²
039 Object Transfer BPL2 -> BPL4
   Child Count.BPL6 less than 1n
040 (BPL4 DIFF BPL1) -> BPL5
041 Dilate CIRC x1 => BPL5
042 Closing CIRC x1 => BPL5 Extend
043 Object Transfer BPL4 -> BPL7
   Child Area.BPL5 less than 80µm²
044 Object Transfer BPL4 -> BPL5
   Child Area.BPL6 less than 0µm²
045 (BPL3 OR BPL7) -> BPL3
046 Zone CIRC  x1 => BPL2
047 Zone CIRC  x1 => BPL3
048 Zone CIRC  x1 => BPL4
049 Zone CIRC  x1 => BPL5
050 (BPL3 OR BPL8) -> BPL3
051 Clear => BPL6, BPL8
052
053 ' Reaction product measurement
054 Closing CIRC x20 => BPL5 Extend
055 Fill => BPL5
056
057 ' Single B4C+rea pro measurement
058 Closing CIRC x20 => BPL4 Extend
059 Fill => BPL4
060
061 ' Multi-B4C+rea pro measurement
062 Closing CIRC x13 => BPL2 Extend
063 Fill => BPL2
064
065 Copy BPL2 -> BPL6
066 (BPL6 OR BPL3) -> BPL6
067 (BPL6 OR BPL4) -> BPL6
068 (BPL6 OR BPL5) -> BPL6
069 Copy BPL6 -> BPL12
070 Erode CIRC x2 => BPL12 Extend
071 (BPL6 DIFF BPL12) -> BPL12
072
073 Field Measures (BPL6)  -> FLDM26
   Area
   Perimeter
   Area Percent
074 Relative Measures -> RELM27
   Area Percent
   BPL6
   Relative to BPL1
075 Object Measures (BPL6) -> OBJM28
```

Area
Perimeter
Sphericity
Aspect Ratio
076 Clear => All
077 Live